

博士論文

A Study on Magnetic Field Generation
by Magnetoconvection in a Model Planet

(モデル惑星内のMHD熱対流による
磁場生成に関する研究)

加藤 浩文

平成 3 年

①
↑

Acknowledgements

博士論文

A Study on Magnetic Field Generation
by Magnetoconvection in a Model Planet

(モデル惑星内のMHD熱対流による磁場生成に関する研究)

加藤 浩文

平成3年度

Acknowledgements

The present thesis has been achieved being supervised by Professor H. Oya who guided the author to the study field of geodynamo and has currently provided chances to increase the research activities. The author wishes to express his sincere thanks to Prof. Oya for his continual advice, suggestions and encouragement to achieve the present study. In every chance of the presentations in the seminar and discussions the author has been accepted valuable suggestions and evaluating supports, in this context, the author would like to express his thanks to Professors H. Fukunishi, T. Saito and T. Nakano.

The colleagues in the Prof. Oya's study group have always encouraged and given the author comments and helpful supports to accomplish the present thesis. The author is also grateful to Mr. A. Tanaka and Mr. T. Moriya and other members of Prof. Oya's group.

Eterm++ is provided by Dr. K. Kohketsu and Dr. K. Takano.

Abstract

Geomagnetic field exists for more than 10^9 years and exhibits temporal variations whose characteristic time scale ranges from tens of years to hundreds of thousands of years. The existence and variation of the intrinsic geomagnetic field are due to the dynamo process; the motion of the electrically conducting fluid in the Earth's outer core generates and maintains the geomagnetic field. Due to the effects of rotation and geometrical constraint of the spherical shell, convection in the Earth's core is supposed to be associated with the helical motion and differential rotation which are key ingredients in the geodynamo process.

To investigate the effect of rotation on convection and the magnetic field generation, numerical simulations of magnetoconvection have been carried out for the cases without and with rotation. A large-scale, laminar dynamo model, where the interaction between large-scale velocity and magnetic fields, generates large-scale magnetic field is set up. The equations of motion, electromagnetic induction and heat conduction have simultaneously solved within the Boussinesq approximation for two basically different configurations ; a plane boundary configuration and a spherical shell configuration.

The model with plane boundaries is chosen to study the basic characteristics of the dynamo process to understand the physical processes in the Earth's outer core region. In the plane boundary model, the angular velocity vector is assumed to be anti-parallel to the gravity vector. Approach for the simulation has been made by the two steps; the first is the non-magnetic case and the second is magnetic case.

The distribution of the kinetic helicity density $h = \mathbf{u} \cdot \nabla \times \mathbf{u}$ has been calculated; the results show that when the convective velocity is small in regime of the linear theory, the

distribution of h is anti-symmetric with respect to the horizontal plane set at the center of the simulation box, while the distribution of h changes into the roughly symmetric one in the large velocity case of the nonlinear regime because of the advection effect of the fluid motion. A part of h defined by, $h_z = u_z \omega_z$ is as a good indicator of the rotation effect. The studies are concentrated on the change of the distribution of h_z due to the advection effect.

In the non-rotating case, the magnetic field is intensified in the early stage of evolution, and then decreases almost monotonically, on the other hand, in the rotating case, the magnetic field keeps a certain level during whole stage of the evolution of the computational run though the saturation level of the magnetic energy is much smaller than that of the kinetic energy. Although the increment of the magnetic energy is only a matter of factor compared with the initial value, the rotation effect which facilitates the magnetic field generation is clearly seen even in the plane boundary model. The geometrical relations between \mathbf{u} and \mathbf{B} , between \mathbf{u} and $\boldsymbol{\omega}$ and between \mathbf{B} and \mathbf{J} are also studied quantitatively using the occurrence frequency of $\cos \theta$ where θ is an angle between two vectors of interests.

The simulations for the magnetic field generation have also been made for a model planet with the conducting fluid region of a spherical shell where the ratio of the inner radius to outer one is set at 0.4 and the gravity is assumed to be in direct proportional to the radius. In this case, the conducting fluid in the shell is adjoining an insulator at the outer boundary and adjoining the conducting solid at the inner boundary. The characteristic points of generated convection in the rotating spherical shell are i) appearance of the convective rolls whose axis are approximately parallel to the rotation axis of the shell and whose longitudinal scale is small compared with that of the non-rotating

case, ii) symmetric nature of convection with respect to the equatorial plane, iii) effective generation of the differential rotation iv) westward drift of the convective pattern and v) large magnitude of the kinetic helicity density.

The fluid motion which shows these features is taken to be candidate state for the magnetic field generation. However, the regenerative processes are not necessarily straightforward but largely depend on the magnetic Prandtl number of the fluid. It becomes apparent that the α -effect, which results in the coupling between the poloidal and toroidal magnetic fields is insufficient when the Prandtl number is small. Further developments of the simulation is considered to simulate real planetary dynamo processes.

A Study on Magnetic Field Generation by Magnetoconvection in a Model Planet

Acknowledgments

Abstract

ContentsI

1. Introduction	1
1.1 Geodynamo theory	1
1.2 Present study	9
1.2.1 Plane boundary model	10
1.2.2 Spherical shell model	11
2. Magnetoconvection between plane boundaries	14
2.1 Role of helicity in dynamo theory	14
2.2 Basic equations and boundary conditions	16
2.3 Algorithm for saving equations	20
2.4 Results and discussion	22
2.4.1 Convection caused by a simple perturbation (non-magnetic case)	22
(a) Time evolution of kinetic energy	22
(b) Velocity field	23
(c) Distribution of helicity density for the rotating case	24
(d) Generation of ω_z	25
(e) Distribution of helicity density for the non-rotating case	27
(f) Temperature field	27
2.4.2 Convection with a complicated perturbation	28
(a) Temporal variation of kinetic energy	29
(b) Velocity field	29
(c) Distribution of helicity density	31
(d) Temperature field	32

2.4.3	Magnetic case	32
(a)	Time evolution of kinetic magnetic energies	32
(b)	Velocity and magnetic field	33
(c)	Geometric relation between the velocity and magnetic field vectors	35
(d)	Kinetic and magnetic energy spectra	36
	Figures	38
3.	Magnetoconvection in a spherical shell	78
3.1	Toroidal and Poloidal fields	78
3.2	Basic equations and boundary conditions	81
3.3	Methods of numerical analysis - Algorithm for simulation	87
3.4	Results and discussion	90
3.4.1	Velocity field	90
(a)	Effect of rotation on convection	90
(b)	Distribution of helicity density	93
(c)	Magnetic field	97
	Figures	100
4.	Discussion	120
4.1	Check for the boundary effects in the results	120
4.2	Necessity of small-scale dynamo	122
4.3	Possible direction for future studies	123
	Figures	125
5.	Conclusion	126
	References	i

1 Introduction

1.1 Geodynamic theory

Plate tectonics is the theory that describes the large-scale motion of the Earth's lithosphere. It is a unifying theory that explains a wide range of geological phenomena, including the formation of mountains, the occurrence of earthquakes, and the distribution of volcanoes. The theory is based on the concept of rigid plates that move relative to each other. The forces driving plate motion are primarily mantle convection and slab pull. Plate boundaries are classified into three types: divergent, convergent, and transform. Divergent boundaries are where plates move apart, convergent boundaries are where plates move together, and transform boundaries are where plates slide past each other horizontally.

1. Introduction

The study of plate tectonics is a rapidly evolving field. Recent advances in geophysical techniques, such as GPS and satellite geodesy, have provided new insights into plate motion and the forces driving it. These techniques have shown that plate motion is not always as simple as previously thought. For example, some plates move in a non-linear fashion, and some plates have internal deformation. The study of plate tectonics is also important for understanding the Earth's history and the evolution of the planet. Plate tectonics has played a major role in the formation of the Earth's crust and the distribution of life. The theory of plate tectonics is a fundamental part of modern geology and is essential for understanding the Earth's dynamic system.

1 Introduction

1.1 Geodynamo theory

Paleomagnetic data indicate that the geomagnetic field exists for more than 10^9 years, while the magnetic diffusive time of the Earth's core could be estimated at several 10^4 years. Therefore, the geomagnetic field is not the 'fossil' one obtained at the time of the formation of the Earth. In addition, the temperature of the Earth's core is supposed to be higher than the Curie point, showing that the geomagnetic field is not a permanent one. Some mechanism for maintenance of the geomagnetic field is necessary. Now, it is widely believed that the geomagnetic field is generated and maintained by the motion of the electrically conducting fluid in the Earth's outer core. This is the geodynamo mechanism.

In the past record it is also shown that the geomagnetic field exhibited the temporal variation, i.e. secular variation, whose characteristic time scales ranged from tens of years (e.g. the sixty year variation) to hundreds of thousands of years (e.g. period of polarity reversals). Among many features of the secular variation, two phenomena are most prominent evidences, polarity reversals and westward drift of the non-dipole component.

The polarity reversals of the axial dipole of the geomagnetic field have occurred irregularly (Cox, 1969), and the distribution of the time span between the reversals is supposed to be roughly Poisson distribution, in contrast with the reversals of the solar magnetic field which take place rather regularly with the period 22 years. In the latest epoch for the geomagnetic polarity, called 'Brunhes' epoch, the polarity has been normal for 0.69 million years, although there were some reverse terms of short duration called 'event' and 'excursion'. A number of models were presented to explain the mechanism of the reversals (Inglis, 1981).

The westward drift of the non-dipole field is clearly shown by separating the non-dipole field into the standing and drifting parts (Yukutake and Tachinaka, 1968,1969). Yukutake and Tachinaka (1969) showed that the spatial distribution of the drifting part is simpler than that of the standing one, and that the typical drift velocity is between 0.2 and 0.3 degree per year depending on the spherical harmonic mode. It was also indicated that there is no interference between the standing and drifting fields, suggesting that two fields are generated by different mechanisms. The westward drift is supposed to reflect the magnetohydrodynamic waves or drift of the convective pattern in the Earth's outer core (Inglis, 1981).

Recently, a secular variation with short time scale, the sixty year variation has been investigated in detail by performing Sompi spectral analysis and by constructing a model (Yokoyama, 1989, 1991). It was shown that the sixty year variation is most likely caused by the interaction between the fluid motion near the core-mantle boundary and the magnetic field. It was also indicated that the sixty year variation exists in most of the Gauss coefficients, and that the amplitude of each mode for the sixty year variation temporally changes almost in phase or anti-phase. The relation of the sixty year variation to the length of day was also discussed in the paper.

Although the temporal and spatial variation of the geomagnetic field is rather complicated, the major part of the geomagnetic field has been the dipole component with axis roughly parallel to the rotation axis.

The goal of studies on the geodynamo theory is to elucidate the interaction between the fluid motion and the magnetic field in the Earth's outer core, and to explain the properties of geomagnetic field, such as the predominance of the dipole component, the westward drift, the time span between the polarity reversals, the behavior of Gauss coefficients

during the reversal process, and to predict the states which could not be observed, such as the intensity of the toroidal magnetic field in the Earth's core, the kinematic viscosity of the Earth's outer core.

The dynamo theory has been extensively studied by many researchers since Elsasser (1946a,b,1947) provided a theoretical treatment of a regenerative process. A number of exquisite models have been constructed with considerable success. From a large number of the works in the history of the studies on geodynamo we will select only core subject here.

Bullard and Gellman (1954) formulated the kinematic dynamo problem by the spherical harmonic expansion of the toroidal and poloidal scalar functions for the magnetic and velocity fields. This model was concerned with the large-scale flow, and the velocity field with low degree in the spherical harmonics was chosen, i.e. T_1 and S_2^{2c} motion. They numerically solved the eigenvalue problem for the induction equation in the steady state, and obtained the eigenvalue, showing that the steady dynamo was feasible. In the Bullard-Gellman (B-G) model, however, the spherical harmonics for the magnetic field higher than degree four were neglected because of the ability of the computer in those days. In fact, it was shown that the truncation in the spherical harmonic expansion possessed serious effect on the eigenvalue problem (Gibson and Roberts, 1969). Lilley (1970) extended the B-G model by adding the S_2^{2s} motion with higher truncation level in the spherical harmonics and larger number of the grid points in the radial direction. In the Bullard-Gellman-Lilley (B-G-L) model, the eigenvalue, which seemed to converge as the truncation level becomes higher, was obtained, showing the model worked as a dynamo. However, Gubbins (1973) investigated the B-G-L model with more refined calculation, and showed that the eigenvalue diverged with a higher level of truncation.

Parker (1955) studied the dynamo process, so-called $\alpha\omega$ - dynamo. In the model, the toroidal magnetic field is generated from the poloidal field by the differential rotation of convection in a rotating shell, i.e. ω -effect. Generation of the poloidal field from the toroidal field (α -effect) was the main issue of the Parker's paper. A large number of small-scale upward flows, which possess helical motion due to the Coriolis force, were considered. These rising eddies, called ' cyclones ' twist the toroidal magnetic field, and statistically generate the poloidal field.

Braginsky (1965a,b, 1975, 1978) invented nearly axisymmetric dynamo which could avoid the Cowling's anti-dynamo theorem (Cowling, 1934). In this model, the large-scale flow including the non-axisymmetric part is treated with high magnetic Reynolds number. The interaction between the non-axisymmetric velocity and magnetic fields creates an α -effect, and the differential rotation causes the ω -effect. Thus, an $\alpha\omega$ -dynamo process becomes possible.

Though Parker's dynamo (Parker, 1955) contains an idea of a statistical dynamo, Steenbeck, Krause and Rädler (1966) investigated mean-field electrodynamics first ; this becomes an epoch-making work on turbulent dynamo. The velocity and magnetic fields are separated into the mean and fluctuating parts. The interaction between the fluctuating velocity and magnetic fields can create the electric current parallel to the mean magnetic field ; that is, an α -effect occurs.

Busse (1975) has proposed a model based on the study of thermal convection in a rapidly rotating system (Busse, 1970). In this model the intensity of the toroidal magnetic field is comparable with that of the poloidal field. Busse's model therefore contrasts with the strong field model, such as the models of Bullard and Gellman (1954) and Braginsky (1965a,b).

In the first stage, the geodynamo problem was investigated kinematically, i.e. using the prescribed velocity field, because of mathematical simplicity. It is, however, essential to adopt the velocity field which satisfies Navier-Stokes equation ; and the magnetic energy in the Earth's outer core is supposed to be larger than the kinetic energy even for the weak field model. In the strong field model the toroidal magnetic field is some hundreds times larger than the poloidal field (Roberts, 1987). Hence, the effect of the magnetic field on the velocity field is essential in the geodynamo, and convection should be treated magnetohydrodynamically.

In the dynamo process, rotation of the system is a significant key. Due to the Coriolis force, convection in the rotation system generates the helical motion which is a key ingredient to facilitate the magnetic field generation. The helical motion is characterized by a quantity, the kinetic helicity defined by $\int \mathbf{u} \cdot \nabla \times \mathbf{u} dV = \int \mathbf{u} \cdot \boldsymbol{\omega} dV$, which is deeply related to the α -effect. In general, helicity, $\int \mathbf{A} \cdot \nabla \times \mathbf{A} dV$ for a vector field \mathbf{A} expresses the extent of twist of the vector field. The effect of the kinetic helicity on the magnetic field generation has been extensively studied in the small-scale, turbulent dynamo problem (Moffatt, 1978; Moffatt and Proctor, 1982; Krause and Radler, 1980). The kinetic helicity of the large-scale, laminar flow is also important for the magnetic field generation (Roberts and Gubbins, 1987). Properties of the kinetic helicity and its role in dynamo process are described in Section 2.1. In addition to rotation, the geometrical property of the convection zone, i.e. a spherical shell provides important effects on the dynamo process of the planet and star. In general, convection in a rotating spherical shell generates the differential rotation which is another key ingredient of the dynamo process. The gradual change of the angle formed by the gravity and angular velocity vectors in a rotating shell has influence on convection and the generated magnetic field. Therefore, in

order to understand the geodynamo mechanism it is necessary to investigate magnetoconvection in a rotating shell. As will be shown in the following sections, however, the basic equation of magnetoconvection is extremely difficult to the analytic approach even for the simple model, that is, non-linear, simultaneous, partial differential equation. Therefore, the numerical approach is needed in the geodynamo problem as well as in the planetary, stellar and galactic dynamo problems.

In the geodynamo problem, there are several candidates of energy sources to drive convection, and three major sources are the thermal buoyancy due to the heat sources in the core, the buoyancy produced by compositional difference of the material distribution in the core and the precession of the Earth, corresponding to thermal, compositional and rotationally powered dynamos, respectively (Roberts and Gubbins, 1987). By considering the energy budget of the Earth, it is pointed out for the Earth's outer core that compositional dynamo is the most plausible one. Thermal dynamo has been most commonly investigated, and is supposed to be relevant to the dynamos of Jupiter, Saturn (Stevenson, 1983) and the Sun. Although we adopt a thermal dynamo as a model of the geodynamo in the present paper, this does not mean that we are considering a compositional dynamo as a minor one. The reasons for choosing thermal convection are rather its simplicity and the fact that the property of the velocity field of thermal convection might be similar to that of compositional one (Roberts and Gubbins, 1987).

The numerical simulations of thermal convection and magnetoconvection in a rotating spherical shell have been so far performed by many researchers. Particularly, Gilman and Glatzmaier has extensively investigated magnetoconvection in a rotating shell motivated by the solar and stellar dynamo processes.

Gilman and Miller (1981) performed a numerical simulation of magnetoconvection

to study the solar dynamo. They simultaneously solved the equation of motion, the electromagnetic induction equation and the thermodynamic equation within the Boussinesq approximation. In their calculation, the finite difference method was used for the spatial derivative, and the polar region is not included because of the numerical instability related to the finite difference method. The results have shown that the simulated equatorial acceleration of the differential rotation is consistent with the observed motion and that the velocity of the differential rotation decreased with depth. The distribution of helicity was also indicated. The properties of the solar magnetic field, such as the migration of the sunspots toward the equator and the polarity reversals with period 22 years, were not simulated. Gilman (1983) extended this model mainly by reducing the kinematic viscosity and the thermal diffusivity, and obtained the equatorial acceleration driven by the weak convective motion compared with the motion of Gilman and Miller (1981). Although the migration of the magnetic field and the cyclic solution were obtained, the direction of the migration was poleward opposite to that of the Sun and the cycle period was small compared with that of the Sun. A regime diagram for the various dynamo actions as functions of the electrical conductivity and the effect of rotation was presented.

Glatzmaier (1984) developed a standard scheme for the numerical simulation of the stellar dynamo problem. The mass flux and magnetic fields are separated into the toroidal and poloidal fields. The spatial derivative was calculated by the pseudospectral method using the Chebyshev, Legendre and Fourier series expansion for the radial, latitudinal and longitudinal direction , respectively. Thus, the simulation of global magnetoconvection in stars has been carried out within the anelastic approximation which is more relevant to the stellar dynamo problem than the Boussinesq approximation. Time evolution was per-

formed by an explicit Adams-Bashforce method for the non-linear terms and an implicit Crank-Nicolson method for the diffusion terms. It has been shown that the differential rotation results in the equatorial acceleration as observed on the Sun, and that the angular velocity of the convective motion decreases with depth. The latitudinal propagation of the magnetic field and the magnetic polarity reversals, which are outstanding phenomena of the solar magnetic field, did not appear in the simulation. This model has been studied in more detail in a series of papers (Glatzmaier, 1985a,b). Glatzmaier (1985a) included the subgrid-scale eddy diffusivity in his simulation. The results have indicated that the magnetic field propagates away from the equator in contrast with the case of the solar magnetic field. A profile of the kinetic helicity has been presented. On the average, the profile of the kinetic helicity is negative in the northern hemisphere and positive in the southern hemisphere. Glatzmaier (1985b) further treated a dynamo process at the base of the convective zone. It has been indicated that though the magnetic field shows the propagation toward the equator, in this case, as observed on the Sun in the initial stage of the simulation, the propagation has been eventually broken.

Experimental simulation of the thermal convection in celestial bodies is quite difficult subject because setting of the radial gravity is required. Busse and Carrigan (1976) tried to achieve the system by utilizing the centrifugal force taking the place of the gravity force with a reversed temperature gradient, considering that the component of the gravity force perpendicular to the rotation axis is more important than the parallel one. Their results have clearly shown the convection rolls as has been predicted by the theory.

Hart, Glatzmaier and Toomre (1986) simulated the radial gravity in the experiment performed on Spacelab 3 on the space shuttle Challenger. In that experiment, the dielectric oil in the electric field experienced the radial force in the micro-gravity state,

and the convective patterns under the various conditions for rotation rate and intensity of the buoyancy force were observed. The effect of variation of the temperature at the boundary was also investigated. It has been shown that in the high rotation cases the non-axisymmetric flow, called 'Banana cells', is dominant at low latitude in agreement with the Taylor-Proudman theorem. Although there are some inappropriate points to compare the experimental results with convection in the Earth's core, such as the r^{-5} dependence of the radial force, the hemispheric shape of the convective region and the large ratio of the inner radius to the outer one, the qualitatively similar properties could be expected. The experimental results were compared with the results of the numerical simulation carried out in parallel, and good agreements were obtained.

Though previous numerical simulations described here contain many fruitful results and provide the important guidance to the geodynamo problem, most of works are mainly concerned with the solar dynamo process. The decisive simulation of geodynamo has not been performed so far.

1.2 Present study

In the present paper, we perform three-dimensional, time-dependent numerical simulation of magnetoconvection to study the geodynamo process for a large-scale dynamo where large-scale, laminar flow generates large-scale magnetic field. In this work, we consider the situation of thermal dynamo in which the thermal buoyancy drives convection. Navier-Stokes equation, the electromagnetic induction equation and the equation of heat conduction are solved simultaneously within the Boussinesq approximation which is considered as a good approximation in the Earth's outer core in contrast with the solar

convective zone.

The present study consists of two parts. First part is devoted for a basic study concerning with magnetoconvection between plane boundaries. Second part is the study of magnetoconvection in a spherical shell which is more relevant to apply for understanding the geodynamo problem.

1.2.1 Plane boundary model

The numerical simulation of magnetoconvection between plane boundaries is carried out to clarify the effect of rotation under simple condition. In this model, the angular velocity vector of the system is anti-parallel to the gravity vector. Therefore, the situation of the simulation box can be taken as a local region picked up from the area near the Earth's north pole. To simulate the system, the periodic boundary condition is imposed in the horizontal direction, while the rigid and perfectly conducting boundaries are used at the vertical end of the simulation box. Spatial derivatives are calculated by the pseudospectral method using Fourier series expansion in the horizontal direction and by second-order finite difference method in the vertical direction. Time integration is carried out by the improved Euler method which consists of the second-order, predictor-corrector method.

In this magnetoconvection in the space with plane boundaries, two different categories of cases, i.e. i) non-magnetic and ii) magnetized cases are simulated.

In the non-magnetic case, the velocity field of convection is studied with the emphasis on the distribution of the kinetic helicity density. The effect of the advection term in Navier-Stokes equation on the distribution of the helicity density is investigated. The distribution is anti-symmetric with respect to the mid-plane ($z = 0$ where z -axis is set in

parallel to the gravity field) when the velocity of convection is small, i.e. the advection term is not effective. This result is consistent with that of the linear theory (Veronis, 1959 ; Chandrasekhar, 1961). As the velocity becomes larger, the distribution of the helicity density changes into approximately symmetric one with respect to the mid-plane because of the effect of the advection term. This effect has not been so far discussed very much. We pay attention to a part of the kinetic helicity, $u_z \omega_z$ which is considered as a good indicator of the effect of rotation because the Coriolis force creates ω_z effectively. Several convective patterns with different Taylor numbers are presented.

For the magnetized case, the effect of the rotation on the magnetic field generation process is investigated, the results of the case under rotation are discussed by comparing with the non-rotating case. Although the magnetic energy increases a value only several times larger than the initial value, we can see the effect of rotation for the generation and maintenance of the magnetic field. The relation between the velocity field \mathbf{u} and the magnetic field \mathbf{B} has been also studied in terms of the distribution of $\cos\theta (= \mathbf{u} \cdot \mathbf{B} / (|\mathbf{u}||\mathbf{B}|))$. The relations between \mathbf{u} and $\boldsymbol{\omega} (= \nabla \times \mathbf{u})$ and between \mathbf{B} and $\mathbf{J} (= \nabla \times \mathbf{B})$ are also investigated.

The plane boundary model provides the basic mechanism of the generation of the helical flow. Although the plane boundary model contains the elementary process of the magnetic field generation, more realistic model than the plane boundary model is required to understand the geodynamo process.

1.2.2 Spherical shell model

Magnetoconvection in a spherical shell for two cases, without and with rotation, is studied to apply for the simulation of convection in the Earth's outer core. The ratio of the inner radius of the shell to the outer one is chosen to 0.4. The shell region of the electrically conducting fluid is adjoining at the outer boundary which consists of an insulator, and adjoining at the inner boundary that consists of the conducting solid with the same conductivity with that of the fluid. At the outer and inner boundaries, the rigid boundary condition is adopted for the velocity field. The velocity and magnetic fields are expressed by the toroidal and poloidal field components. The toroidal and poloidal scalar functions for the velocity and magnetic fields, and also the temperature field are expanded in the spherical harmonic series. Spatial derivatives are computed by the pseudospectral method in the latitudinal and longitudinal directions; and second order finite difference method is applied to calculate the radial dependence. Time integration is computed by the improved Euler method as has been employed in the plane boundary model. The present simulation of magnetoconvection has been carried out for various values of the non-dimensional parameters, that is, the bouyancy parameter, the Taylor number, the Prandtl number and the magnetic Prandtl number. Although the purpose of the simulation is to have final simulation of the geodynamo process, some non-dimensional numbers of our simulation such as, the Rayleigh number, the Taylor number and the magnetic Prandtl number are quite different from those of the Earth's outer core. Due to this reason we here use the terminology, ' model planet ' in the whole current of the present thesis. However, we consider that useful suggestions for the geodynamo could be obtained from the results of the present simulation. It is shown that when the effect of rotation is evident, convective rolls whose rotation axis are parallel to the rotation axis of the shell become apparent

and the convective motion shows the tendency of symmetry with respect to the equatorial plane. The helical motion due to the Coriolis force becomes dominant in the polar region; the Coriolis force therefore strongly controls the situation as is the case of the plane boundary model which has been studied as basic cases. The result also shows the westward drift of the convective pattern. The generation process of the magnetic field has also been studied by controlling parameters. non-dimensional numbers. For most of the cases of the present calculations, the obtained magnetic energy decreases with time. For the case of the large Prandtl number, corresponding to the small magnetic diffusivity, however, the magnetic energy starts to increase and show temporal variations. The generated magnetic field indicates rather intermittent nature including the relatively large amplitude in the spherical harmonics with high degree. This property is rather irrelevant to take the resulted magnetic field as the real geomagnetic field. These results suggest that there is another component of some dynamo mechanism which is not included in the present simulation. One possible point is in the α -effect which is taken only insufficiently into the present simulation, because of large-scale nature of the present approach to magnetoconvection. The α -effect connected to the small-scale motion is thought as a effective generation mechanism. The studies on the model which include small scale turbulence could simulate more effective processes to realize the actual geodynamo, but the detail studies in this direction are deferred for future studies.

2. Magnetoconvection between plane boundaries

2.1. Role of helicity in dynamic theory

Helicity, named by Moffatt (1969), indicates the sense of twist of a vector field. For a vector field \mathbf{A} , helicity H is defined as

$$H = \int_V \mathbf{A} \cdot \nabla \times \mathbf{A} \, dV. \quad (2.1)$$

The helicity H is therefore a pseudoscalar. It is equal to zero in the global equilibrium state. When a material junction, such as the vertical shear layer, is introduced, the helicity is

2. Magnetoconvection between plane boundaries

boundaries

Moffatt and Proctor (1982), Krauss and Walker (1985) and, for example, in the simplified case the α -effect is expressed as

$$\alpha = -\frac{1}{3} \frac{H}{\Lambda} \quad (2.2)$$

where Λ is the mean electromotive force and \mathbf{B} the mean magnetic field. The relation between α and helicity could be written as

$$\alpha = -\frac{1}{3} \frac{H}{\Lambda} \left(1 + \frac{R_m}{R_m + 1} \right) \quad (2.3)$$

where $F(k, \omega)$ is the helicity spectrum function which is related to the small-scale structure of the velocity field as

$$\alpha = -\frac{1}{3} \frac{H}{\Lambda} \left(1 + \frac{R_m}{R_m + 1} \right) \quad (2.4)$$

2 Magnetoconvection between plane boundaries

2.1 Role of helicity in dynamo theory

Helicity, named by Moffatt (1969), indicates the extent of twist of a vector field. For a vector field \mathbf{A} , helicity H is defined as

$$H = \int \mathbf{A} \cdot \nabla \times \mathbf{A} dV. \quad (2.1)$$

The helicity H is, therefore, a pseudoscalar and is equal to zero in the mirror-symmetric state. When a preferred direction, such as the rotation axis exists, the mirror-symmetry is broken and helicity possesses a finite value. In the dynamo theory, the kinetic helicity $\int \mathbf{u} \cdot \nabla \times \mathbf{u} dV$ plays an essential role in connection with the α -effect. The kinetic helicity has been extensively studied in the small-scale turbulent dynamo model (Moffatt, 1978 ; Moffatt and Proctor, 1982 ; Krause and Rädler, 1980). For example, in the simplest case the α -effect is expressed as

$$\bar{\epsilon} = \alpha \bar{\mathbf{B}}, \quad (2.2)$$

where $\bar{\epsilon}$ is the mean electromotive force and $\bar{\mathbf{B}}$ the mean magnetic field. The relation between α and helicity could be written as

$$\alpha = -\frac{1}{3}\lambda \iint \frac{k^2 F(k, \omega)}{\omega^2 + \lambda^2 k^4} dk d\omega, \quad (2.3)$$

where $F(k, \omega)$ is the kinetic helicity spectrum function which is related to the small-scale fluctuating velocity field \mathbf{u} by

$$\overline{\mathbf{u} \cdot \nabla \times \mathbf{u}} = \iint F(k, \omega) dk d\omega. \quad (2.4)$$

Thus, the mean kinetic helicity $\overline{\mathbf{u} \cdot \nabla \times \mathbf{u}}$ plays a key role in the turbulent dynamo model. Although the kinetic helicity is deeply related to the α -effect, Gilbert, Frisch and Pouquet (1988) have shown that ' helicity is unnecessary for alpha effect dynamos, but it helps.' In any case, the flow with the kinetic helicity generates the magnetic field effectively. The kinetic helicity is also important in the large-scale laminar dynamo model (Roberts and Gubbins, 1987). Hence, study on the distribution of the kinetic helicity density is necessary to understand the dynamo mechanism.

There are other helicities which also possess significant effect on the magnetic field generation, such as the magnetic helicity $\int \mathbf{A} \cdot \mathbf{B} dV$ ($\mathbf{B} = \nabla \times \mathbf{A}$) or $\int \mathbf{B} \cdot \mathbf{J} dV$ ($\mathbf{J} = \nabla \times \mathbf{B}$) and the cross helicity $\int \mathbf{u} \cdot \mathbf{B} dV$. It is well known that the the magnetic helicity causes the inverse energy cascade in MHD turbulence (Pouquet, Frisch and Leorat, 1976). Although the effects of $\int \mathbf{u} \cdot \mathbf{B} dV$ and $\int \mathbf{B} \cdot \mathbf{J} dV$ have not been discussed very much in the context of dynamo problem, Yoshizawa (1990) has pointed out their importance in the turbulent dynamo and performed turbulence modeling using these helicities. In the ideal MHD fluid, the magnetic and cross helicities are conserved as well as the total energy. Therefore, the magnetic and cross helicities play a key role in the self-organization phenomena together with the total energy (Taylor, 1974; Hasegawa, 1985).

In the present paper we investigate the kinetic helicity density in convection without and with rotation. From now on, we will call the kinetic helicity ' helicity ' for simplicity.

In a rotating body the Coriolis force generates the helical flow which possesses helicity. The helical flow facilitates the magnetic field generation. For example, in the $\alpha\omega$ -dynamo, the helical motion twists the toroidal magnetic field and generates the poloidal magnetic field (Parker, 1955). In this section, the distribution of the helicity density is studied for convection between plane boundaries within the Boussinesq approximation, that is,

Bénard convection. It has been shown by the linear theory that in Bénard convection with rotation the helicity density is positive in the lower half region and negative in the upper half region when the system rotates counterclockwise (Veronis, 1959; Chandrasekhar, 1961). Namely, at the bottom (top) of the upward flow the horizontal flow converges (diverges) with counterclockwise (clockwise) rotation because of the Coriolis force. On the other hand, at the bottom (top) of the downward flow the horizontal flow diverges (converges) with clockwise (counterclockwise) rotation. When the convective velocity is large, the situation becomes complicated owing to the effect of the advection term in Navier-Stokes equation. We investigate the effect of the advection term on the helicity density by the numerical simulation. In order to see the advection effect clearly, convection with a simple initial perturbation of the temperature field is simulated first. We focus our attention on a part of helicity, that is, $u_z \omega_z$ which is considered as a good indicator of the rotation effect because the Coriolis force generates ω_z effectively. Second, the simulation of convection with a complicated perturbation is performed. The change of the distribution of helicity density and convective pattern depending on the Taylor number is presented.

2.2 Basic equations and boundary conditions

A plane boundary model is considered here to study the effect of rotation on convection and the magnetic field generation under simple condition before we treat a more realistic model given in Section 3. The profiles of the gravity and angular velocity vector field distributions of the present model are similar to that in the region near the north pole of the Earth though some boundary conditions, such as the periodic boundary condition

and the condition for the electrically perfect conductor, are oversimplified.

We consider magnetoconvection in a horizontal layer of thickness $2L$, adopting the Boussinesq approximation. The temperature at the top and bottom boundaries are assumed to be uniform, i.e. $T_0 - T_1$ and $T_0 + T_1$, respectively. The basic equations for magnetoconvection within the Boussinesq approximation are the equations of the motion (Navier-Stokes equation), electromagnetic induction and heat conduction, respectively given by,

$$\frac{\partial \mathbf{u}}{\partial t} = \mathbf{u} \times \boldsymbol{\omega} - \frac{1}{\rho_0} \nabla \left(p + \frac{1}{2} \rho_0 |\mathbf{u}|^2 - \frac{1}{2} \rho_0 |\boldsymbol{\Omega} \times \mathbf{u}|^2 \right) - \nu \nabla \times \nabla \times \mathbf{u} + \frac{\rho}{\rho_0} \mathbf{g} + \frac{1}{\rho_0} \mathbf{J} \times \mathbf{B} - 2 \boldsymbol{\Omega} \times \mathbf{u}, \quad (2.5)$$

$$\frac{\partial \mathbf{B}}{\partial t} = \nabla \times (\mathbf{u} \times \mathbf{B}) - \lambda \nabla \times \nabla \times \mathbf{B}, \quad (2.6)$$

$$\frac{\partial T}{\partial t} + (\mathbf{u} \cdot \nabla) T = \kappa \nabla^2 T, \quad (2.7)$$

where

$$\boldsymbol{\omega} = \nabla \times \mathbf{u}, \quad (2.8)$$

$$\mathbf{J} = \frac{1}{\mu_0} \nabla \times \mathbf{B}. \quad (2.9)$$

These basic equations are supplemented by the equation of continuity for an incompressible fluid and the equation of state, that is,

$$\nabla \cdot \mathbf{u} = 0, \quad (2.10)$$

$$\rho = \rho_0 \{1 - \alpha(T - T_0)\}. \quad (2.11)$$

In the above equations, \mathbf{u} is the velocity, $\boldsymbol{\omega}$ vorticity, p pressure, ρ density, \mathbf{B} magnetic field, \mathbf{J} electric current density and T temperature. Other symbols $\nu, \lambda, \kappa, \mu_0, \alpha, \rho_0, T_0, \boldsymbol{\Omega}$

and g refer to kinematic viscosity, magnetic diffusivity, thermal diffusivity, magnetic permeability of vacuum, coefficient of thermal expansion, representative density, representative temperature, angular velocity vector and gravity vector, respectively. In the present model $\mathbf{g} = (0, 0, -g)$ where g is a positive constant, and $\mathbf{\Omega}$ is assumed to be anti-parallel to \mathbf{g} , i.e. $\mathbf{\Omega} = (0, 0, \Omega)$ where Ω is a positive constant, so that the system rotates around the z-axis counterclockwise. We assume that ν, λ and κ are uniform in the system.

Taking the *curl* of Eq. (2.5) to eliminate the pressure term, we obtain the equation for the vorticity, that is,

$$\frac{\partial \boldsymbol{\omega}}{\partial t} = \nabla \times \left(\mathbf{u} \times \boldsymbol{\omega} + \frac{\rho}{\rho_0} \mathbf{g} + \frac{1}{\rho_0} \mathbf{J} \times \mathbf{B} - 2\mathbf{\Omega} \times \mathbf{u} \right) - \nu \nabla \times \nabla \times \boldsymbol{\omega}. \quad (2.12)$$

The equation for the z-component of the vorticity results in

$$\frac{\partial \omega_z}{\partial t} = \left[\nabla \times \left(\mathbf{u} \times \boldsymbol{\omega} + \frac{1}{\rho_0} \mathbf{J} \times \mathbf{B} \right) \right]_z + 2\Omega \frac{\partial u_z}{\partial z} + \nu \nabla^2 \omega_z. \quad (2.13)$$

By operating the *curl* to Eq. (2.12) once again, the equation for $\nabla^2 u_z$ can be written as,

$$\frac{\partial \phi}{\partial t} = - \left[\nabla \times \nabla \times \left(\mathbf{u} \times \boldsymbol{\omega} + \frac{1}{\rho_0} \mathbf{J} \times \mathbf{B} \right) \right]_z - 2\Omega \frac{\partial \omega_z}{\partial z} + \nu \nabla^2 \phi + g\alpha \nabla_{\perp}^2 T, \quad (2.14)$$

where

$$\nabla_{\perp}^2 = \frac{\partial^2}{\partial x^2} + \frac{\partial^2}{\partial y^2}, \quad (2.15)$$

$$\phi = \nabla^2 u_z. \quad (2.16)$$

To obtain the non-dimensional forms of the basic equations, we chose L as the length scale, L^2/κ as time scale, T_1 as temperature scale and $\sqrt{\rho_0 \mu_0 \kappa}/L$ as scale of the magnetic field. The non-dimensional equations corresponding to Eqs. (2.13), (2.14), (2.6) and (2.7) are then given, respectively, as follows,

$$\frac{\partial \omega_z}{\partial t} = [\nabla \times (\mathbf{u} \times \boldsymbol{\omega} + \mathbf{J} \times \mathbf{B})]_z + P_r \sqrt{T_a} \frac{\partial u_z}{\partial z} + P_r \nabla^2 \omega_z, \quad (2.17)$$

$$\frac{\partial \phi}{\partial t} = -[\nabla \times \nabla \times (\mathbf{u} \times \boldsymbol{\omega} + \mathbf{J} \times \mathbf{B})]_z - P_r \sqrt{T_a} \frac{\partial \omega_z}{\partial z} + P_r \nabla^2 \phi + P_r R_a \nabla_{\perp}^2 T, \quad (2.18)$$

$$\frac{\partial \mathbf{B}}{\partial t} = \nabla \times (\mathbf{u} \times \mathbf{B}) - P_r / P_{rM} \nabla \times \nabla \times \mathbf{B}, \quad (2.19)$$

$$\frac{\partial T}{\partial t} + (\mathbf{u} \cdot \nabla) T = \nabla^2 T. \quad (2.20)$$

In the above equations, four non-dimensional numbers appear, i.e. R_a (the Rayleigh number), T_a (the Taylor number), P_r (the Prandtl number) and P_{rM} (the magnetic Prandtl number), defined by

$$R_a = \frac{g \alpha T_1 L^3}{\nu \kappa}, \quad T_a = \frac{4 \Omega^2 L^4}{\nu^2}, \quad P_r = \frac{\nu}{\kappa}, \quad P_{rM} = \frac{\nu}{\lambda}. \quad (2.21)$$

It should be noted that for the non-rotating and non-magnetic case the critical Rayleigh number of Bénard convection with two rigid boundaries is $106.8 (= 1708/2^4)$ because of our definition of L .

The time evolution of Eqs. (2.17) to (2.20) is performed by the numerical methods described in the next subsection. The region of the simulation box is $0 \leq x \leq 2\pi$, $0 \leq y \leq 2\pi$ and $-1 \leq z \leq 1$ (Fig. 2.1). Therefore, two aspect ratios Γ_x and Γ_y are equal to π . We adopt the periodic boundary condition in the horizontal direction. In the vertical direction, the temperature is set at $T = \mp 1$ at $z = \pm 1$, and the rigid boundary condition for the velocity field is imposed at the boundaries. Therefore, the following conditions hold at the boundaries $z = \pm 1$,

$$\mathbf{u} = 0, \quad \frac{\partial \mathbf{u}}{\partial x} = \frac{\partial \mathbf{u}}{\partial y} = 0. \quad (2.22)$$

$$\omega_z = 0. \quad (2.23)$$

From the equation of continuity, it follows

$$\frac{\partial u_z}{\partial z} = 0. \quad (2.24)$$

We treat the model that the electrically conducting fluid is adjoining the perfect conductor at $z = \pm 1$. The electromagnetic boundary conditions are as follows.

$$B_z = 0, \quad E_x = E_y = 0. \quad (2.25)$$

The conditions (2.22), (2.25) and the Ohm's law, which is expressed as

$$\mathbf{J} = \sigma(\mathbf{E} + \mathbf{u} \times \mathbf{B}), \quad (2.26)$$

lead to the condition,

$$J_x = J_y = 0. \quad (2.27)$$

In addition, from the equation of continuity for the electric current, it follows that

$$\frac{\partial J_z}{\partial z} = 0. \quad (2.28)$$

2.3 Algorithm for solving equations

The non-dimensional basic equations with the boundary conditions described in the preceding subsection are numerically solved in the following way. The time integration of $\omega_z, \phi, \mathbf{B}$ and T is performed in the spectral space ; then, the velocity component u_z is obtained for the function ϕ by solving Poisson equation (2.16). The velocity components u_x and u_y are calculated from u_z and ω_z using Eqs. (2.8) and (2.10). The vorticity components ω_x and ω_y are obtained by Eq. (2.8); and \mathbf{J} is calculated from Eq. (2.9). Then, the quantities $\mathbf{u}, \boldsymbol{\omega}, \mathbf{B}, \mathbf{J}$ and T are transformed into the physical space and the nonlinear terms are obtained. These nonlinear terms are transformed to the spectral space. Thus, the time evolution for one-step is completed.

To calculate the spatial derivatives in the horizontal direction, we adopt the pseudospectral method with Fourier series expansion (Orszag, 1971,1972). In the pseudospectral method, the spatial derivative is obtained in the spectral space, while the multiplication for the nonlinear term is carried out in the physical space. The derivatives with respect to x and y are readily and accurately evaluated by the property of the trigonometric function. Fourier transform could be effectively performed by using a Fast Fourier transform scheme. The aliasing error is not removed because the present simulation is only concerned with a large-scale laminar flow. In the vertical direction, the second order finite difference method is adopted. The time integration is carried out by the improved Euler method which is a predictor-corrector method with second order accuracy.

In the following numerical results, the number of mesh points $N_x \times N_y \times N_z$ is chosen to $32 \times 32 \times 33$ and the time interval for the time integration is 0.001. Two Prandtl numbers are fixed to 1 ; and the simulation runs have been made for various Rayleigh and Taylor numbers.

At the initial time of the simulation, the fluid is assumed to be at rest. To cause convection, a perturbation is given to the temperature field which possesses a thermal conduction profile, $T(z) = -z$. In the magnetic case, a weak, horizontally uniform magnetic field exists initially, that is, $\mathbf{B}(t=0) = (0.1, 0.1, 0)$.

As a test of our simulation code, we have numerically investigated the critical Rayleigh number of Bénard convection both for the rigid and free boundaries. For both cases numerical results are in good agreement with the values derived by the linear stability theory (Chandrasekhar, 1961). Simulations with different resolution for space and time have been made to check accuracy of the calculation, for $N_x = N_y = 64$, $N_z = 49$ and

$dt = 0.0005$. In addition, we tested our results by using a different time integration scheme, i.e. second order Adams-Bashforth method. All these treatments provide essentially the same results, showing the validity of the present numerical method.

The simulations have been performed using the NEC SX-2N and Fujitsu VP-200 computers. In the SX-2N computer system, the time integration of 4000 time-steps takes about 46 minutes for the non-magnetic case and about 75 minutes for the magnetic case.

2.4 Results and discussion

2.4.1 Convection caused by a simple perturbation (non-magnetic case)

Computer runs for simulations have been made for various R_a and T_a starting with initial temperature given by

$$T_{dis} = c \sin x \cdot \sin y \cdot (1 - z^2). \quad (2.29)$$

This T_{dis} value is added to the equilibrium temperature profile $T(z) = -z$. The value of constant c in (2.29) is set to be 0.1. Thus, convection with cellar pattern is set up.

(a) Time evolution of kinetic energy

The obtained kinetic energy as a function of time is shown in Fig. 2.2 where the total kinetic energy E_{Ktotal} , with x, y and z -components of the kinetic energy ; E_{Kx}, E_{Ky} and E_{Kz} , respectively, are plotted. The energies E_{Kx} and E_{Ky} show the same value because of the homogeneously applied condition of the perturbation in x and y direction as given by Eq. (2.29). In the first stage the energy increases exponentially, and then the flow experiences nonlinear saturation stage. Finally, the system approaches a steady state. In

general the system does not always settle into a steady state, that is, oscillatory or more complicated temporal behavior take place. In this case, the steady state is realized due to the relatively low Rayleigh number and the simple sinusoidal structure of the initial perturbation. The total energy of the rotating case ($T_a = 100$, $R_a = 400$) is given in Fig. 2.2(b) where E_{Ktotal} is smaller than that of the non-rotating case ($T_a = 0$, $R_a = 400$) as shown in Fig. 2.2(a). This can be understood as the result of the function of rotation to inhibit convection (Chandrasekhar, 1961). The ratio of E_{Kx} (E_{Ky}) to E_{Kz} of the rotating case is larger than that of the non-rotating case as the result of the Coriolis force.

(b) Velocity field

The velocity field \mathbf{u} at $t = 2$, when the system reaches almost steady state, is shown in Fig. 2.3 to 2.5. In Fig. 2.3, projection of \mathbf{u} is indicated on the vertical plane at $y = \pi/2$ where simple convective pattern is shown. On this plane, convective pattern for the rotating case which is similar to that for the non-rotating case is projected. However, on the horizontal plane $z = -3/4$ the effect of rotation on \mathbf{u} is clearly seen as shown in Fig. 2.4. There are two upward flows centered at $(x = \pi/2, y = \pi/2)$ and $(x = 3\pi/2, y = 3\pi/2)$, and two downward flows centered at $(x = \pi/2, y = 3\pi/2)$ and $(x = 3\pi/2, y = \pi/2)$. Since the plane at $z = -3/4$ is near the bottom boundary, the horizontal flow converges to the upward flow and diverges from downward flow. In the non-rotating case (Fig. 2.4(a)) the horizontal flow converges and diverges radially. On the other hand, in the rotating case (Fig. 2.4(b)) the flow converges with counterclockwise rotation and diverges with clockwise rotation. Namely, the Coriolis force creates the positive (negative) ω_z in the region where the horizontal flow converges (diverges), generating the helical flow. In addition, it is found that the absolute value of ω_z for the

convergent flow is larger than that for the divergent flow. In the linear theory ω_z of the convergent and divergent flows possesses a same absolute value with opposite sign. This asymmetry of $|\omega_z|$ for the convergent and divergent flows is due to the advection effect of the flow and is discussed in detail below. Figure 2.5 shows the contour plot of u_z on the horizontal plane at $z = 0$ where thin (thick) lines represent the positive (negative) values of u_z . The simple square cells are seen in the non-rotating case (Fig. 2.5(a)). In the rotating case (Fig. 2.5(b)) this simple pattern is deformed by the Coriolis force.

(c) Distribution of helicity density for the rotating case

Here, we present the contour plots of the helicity density $h(= \mathbf{u} \cdot \boldsymbol{\omega})$ for the rotating case. In Fig. 2.6, indicates h in the vertical plane at $y = \pi/2$ for three different times, $t = 0.1, 0.5$ and 2.0 . The intervals between contour lines in Fig. 2.6 are 0.05 (a), 5 (b) and 40 (c) is indicated. At $t = 0.1$ (Fig. 2.6(a)) when the velocity of convection is still small, the distribution of h is nearly anti-symmetric with respect to the mid-plane ($z = 0$) ; h is positive (negative) in the lower (upper) half layer coinciding with prediction of the linear theory (Veronis, 1959 ; Chandrasekhar, 1961). During further evolution, however, the distribution of h changes into approximately symmetric one (Figs. 2.6(b) and (c)); the process can be attributed to the advection of the flow. At $t = 2$ the system reaches a almost steady state (Fig. 2.2). In order to see the effect of the rotation and advection clearly, we focus our attention on a part of the helicity density, i.e. $h_z(= u_z \omega_z)$ which is a good indicator of the rotation effect in Bénard convection with rotation as described above. The contour map of h_z on the same plane and times as those in Fig. 2.6 is indicated in Fig. 2.7. At $t = 0.1$ (Fig. 2.7(a)) the distribution of h_z is nearly anti-symmetric about the mid-plane, and h_z is positive (negative) in the lower (upper) half region.

This distribution is caused by the evidence that in the upward flow (i.e. $u_z > 0$) $\omega_z > 0$ in $z < 0$ and $\omega_z < 0$ in $z > 0$, while in the downward flow ($u_z < 0$) $\omega_z < 0$ in $z < 0$ and $\omega_z > 0$ in $z > 0$. Though this mechanism of the generation of anti-symmetric h_z is simple, the situation becomes complicated when the velocity increases and the advection term becomes effective. The advection of the flow transports and stretches the vortex. The transport of the vortex by the upward and downward motion is clearly seen in Figs. 2.7(a) and (b). Namely, the vortex with positive (negative) ω_z generated in the bottom (top) region is carried to the upper (lower) part by the upward (downward) flow. This transport effect of the advection changes the distribution of h_z from nearly symmetric one into approximately anti-symmetric one.

(d) Generation of ω_z

In order to study the effect of the advection term on ω_z quantitatively more in detail, we have considered the equation,

$$\frac{\partial \omega_z}{\partial t} = [(\boldsymbol{\omega} \cdot \nabla) \mathbf{u} - (\mathbf{u} \cdot \nabla) \boldsymbol{\omega}]_z + P_r \sqrt{T_a} \frac{\partial u_z}{\partial z} + P_r \nabla^2 \omega_z, \quad (2.30)$$

which is rewritten from Eq. (2.13). To study the generation process of ω_z we trace three terms in Eq. (2.30), that is, $\omega_z \partial u_z / \partial z$ (the term of stretching), $u_z \partial \omega_z / \partial z$ (the term of transporting) and $P_r \sqrt{T_a} \partial u_z / \partial z$ (the term of the Coriolis force). These terms are traced at three spatial points, $L(\pi/2, \pi/2, -1/4)$, $M(\pi/2, \pi/2, 0)$ and $U(\pi/2, \pi/2, +1/4)$. At these points, four other terms of the advection are supposed to be zero. The time evolution of three terms at point L given in Fig. 2.8(a) shows that the linear term of the Coriolis force dominates in the initial period, generating positive ω_z . During the time passage, the nonlinear terms make growth and become larger than the linear term. In this

nonlinear stage, the transporting term $-u_z \partial \omega_z / \partial z$ carries positive ω_z into point L from the lower part where positive ω_z is created effectively. In addition, the stretching term produces positive ω_z . Thus, all these terms contribute to keep positive ω_z at point L, so that h_z is always positive at this point. The evolution at point M (Fig. 2.8(b)) indicates that in the early stage the three terms are smaller than those at point L. In the initial stage when the linear theory is applicable, u_z shows a symmetric profile with respect to the plane $z = 0$ so that the Coriolis term is zero and the nonlinear terms are naturally zero. After the initial stage, the transporting term grows first and breaks the symmetric profile of u_z , followed by the growth of the Coriolis and stretching terms. Among these three terms the transporting term, which contributes to make ω_z positive, dominates over two other terms which contribute negative ω_z . Consequently, h_z at point M becomes positive as a result of the transporting effect. The evolution at point U (Fig. 2.8(c)) shows that the Coriolis term dominates in the initial stage. Although this state is similar to that at point U, there is a difference between h_z patterns in M and U because the Coriolis term generates negative ω_z at point U because of the negative value of $\partial u_z / \partial z$. When the linear theory is legitimate, the absolute value of the Coriolis term at point U is equal to that at point D because points U and D are selected at the same x, y with opposite sign of z . The fact that the absolute values of the Coriolis force at point U is equal to that at point D leads to the same absolute value of ω_z at two points. When the evolution enter into the nonlinear phase, the transporting term which contributes to positive ω_z becomes larger than the sum of the two other terms which make a contribution to the negative ω_z . This temporal change of ω_z on the plane $z = +1/4$ is clearly seen in Fig. 2.9 where the contour plot of ω_z is given for the three times, $t = 0.1$ (a), 0.5 (b) and 2.0 (c). In the region where the upward flow exists, such as point U, ω_z is negative at $t = 0.1$

(Fig. 2.8(a)) and becomes positive as time goes (Figs. 2.8(b) and (c)). Hence, h_z at point U also becomes positive. Thus, the distribution of h_z changes into approximately symmetric one from anti-symmetric one. The contour map of h on the horizontal plane $z = 0$ at $t = 2$ is shown in Fig. 2.10 where the interval between contour lines is 20.

(e) Distribution of helicity density for the non-rotating case

Here, we compare helicity of the rotating case described above with that of the non-rotating case. Figure 2.11 shows the helicity density of the non-rotating case on the three planes $z = 0$, $y = \pi/2$ and $x = \pi/2$ at $t = 2$. The helicity density of the non-rotating case is smaller than that of the rotating case though the kinetic energy of the non-rotating case is larger than that of the rotating case (Fig. 2.2). When the velocity is small and the linear theory holds, the helicity density of the non-rotating case is equal to zero everywhere in the system (Veronis, 1959 ; Chandrasekhar, 1961). When the velocity becomes large, however, the helicity density takes a finite value even for the non-rotating case because of the advection effect. A part of the helicity density, h_z of the non-rotating case is much smaller than that of the rotating case. To express the rotation effect quantitatively, we present the value of $\int |h| dV (= |H|)$, $\int |h_x + h_y| dV (= |H_x + H_y|)$ and $\int |h_z| dV (= |H_z|)$ where H is not indicated $|H|$ because of the symmetric structure of h discussed above. In the non-rotating case $|H_z|$ is much smaller than $|H_x + H_y|$. In Table 2.1 we also present three quantities which are supposed to be good indexes of the rotation effect on flow, that is, $|H|/(u_{rms}\omega_{rms})$, $|H_z|/|H|$ and $|H_z|/(u_{rms}\omega_{rms})$ where u_{rms} is root-mean-square velocity and ω_{rms} is root-mean-square vorticity, which are also shown in Table 2.1.

(f) Temperature field

In Fig. 2.12, the temperature field of the non-rotating and rotating cases are indicated on the two planes at $z = 0.5$ and $y = \pi/2$ at $t = 2$. The isothermal lines are deformed by the convective motion. The horizontally averaged temperature profile is shown in Fig. 2.13 together with the thermal conduction profile. The gradient of the average temperature is large in the vicinity of the boundaries and small in the middle of the system. The Nusselt number, which is a index of the intensity of convection, is given in Table 2.1, showing that the Nusselt number of the rotating case is smaller than that of the non-rotating case because the rotation effect depresses convection.

2.4.2 Convection with a complicated perturbation

So far we have discussed simple cellular convection caused by a sinusoidal perturbation. Though the results are fairly simple, the obtained flows have clearly shown the effect of rotation and advection. Because the sinusoidal temperature perturbation is not an uniquely decided solution, however, we have to study convection with a complicated initial perturbation. In the following calculations the perturbation of the temperature fields contain a number of Fourier modes within a range of $1 \leq k_{\perp} \leq 8$, where $k_{\perp} = \sqrt{k_x^2 + k_y^2}$. All Fourier modes are assumed to take a same amplitude and random phase. In Fig. 2.14 the isothermal lines of the initial temperature field, on the three plane at $z = 0$, $y = \pi/2$ and $x = \pi/2$ are indicated. The initial temperature field consists of the thermal conduction profile and the perturbation. Using this initial condition, we have made four computational runs with different Taylor numbers, i.e. $T_a = 0, 25, 100$ and 400 with the Rayleigh number fixed to 1000 .

(a) Temporal variation of kinetic energy

The temporal variation of the kinetic energy of the four cases is indicated in Fig. 2.15. In these cases the system does not reach the steady state within the period of the simulation but exhibits an oscillatory or more complicated temporal behavior, in contrast with the cases for simple sinusoidal temperature perturbation. The total kinetic energy E_{Ktotal} for $T_a = 0$ exhibits oscillatory behavior after about $t = 1.5$. This oscillation does not take place for higher T_a value. It is shown that the kinetic energy for the case of $T_a = 400$ is smaller than that for $T_a = 0$, indicating that the effect of rotation depresses convection. In the case of $T_a = 0$ (Fig. 2.15(a)), E_{Kx} and E_{Ky} vary approximately in phase and E_{Kz} and E_{Kx} (E_{Ky}) change almost in anti-phase. The value of E_{Ky} approaches zero periodically. When the value of E_{Ky} is much smaller than the values of E_{Kx} and E_{Kz} , 2-dimensional roll whose axis is parallel to the y -axis exists. The axis of the roll changes into a sinusoidal curve with time ; reflecting the relatively large value of E_{Kz} . On the other hand, in the case of $T_a = 400$ (Fig. 2.15(d)) E_{Ky} is comparable to E_{Kx} ; the results show the cellular convection pattern rather than the roll-like convective pattern.

(b) Velocity field

In Fig. 2.16 the horizontal velocity field on the plane ($z = 0$) at $t = 4$ for $T_a = 0, 25, 100$ and 400 is indicated. In the case of $T_a = 0$ (Fig. 2.16(a)) the weak horizontal flow exists on the plane without any remarkable vortex. When the Taylor number increases, apparent vortex patterns of the flow appear as shown in Fig. 2.16(c) and (d). On the average, the vortexes with counterclockwise rotation, i.e. positive ω_z , dominate because of the effect of the Coriolis force and advection as discussed above. In

addition to the generation of the vortex, general horizontal scale of the convective motion is shortened as a result of rotation (Chandrasekhar, 1961). This effect of rotation is more clearly seen in Fig. 2.17 where the contour maps of u_z on the same plane at the same time with the case of Fig. 2.16 are presented. In Fig. 2.17 thin lines represent positive values, i.e. upward flow, and thick lines and thinnest line represent negative values and zero, respectively. In the non-rotating case (Fig. 2.17(a)) roll-like convection takes place; the axis of the roll oscillates sinusoidally. (Fig. 2.15(a)). The distribution of u_z in the upward flow region is nearly the same with that in the downward flow region. The symmetric nature of the upward and downward flows is still observable in the case of $T_a = 25$ (Fig. 2.17(b)), while the symmetry shows the tendency to be lost for the case of strong rotation (Figs 2.17(c) and (d)). In the case of $T_a = 400$ the horizontal scale of the convective motion becomes small and the cellular convective pattern becomes apparent. In the rotating case, the vertical flows are accompanied by the vortices as shown in Fig. 2.16, that is to say, the helical flow which becomes essential origin for the magnetic field generation is realized. (The magnetic field generation by the flows with $T_a = 0$ and $T_a = 100$ will be studied in the next section).

In order to provide the 3-dimensional image of the velocity field for the non-rotating case with $T_a = 0$, the velocity vector field \mathbf{u} at three cross sections, $z = -3/4, y = \pi/4$ and $x = \pi/4$ is given in Fig. 2.18; and the contour plots for u_z on $z = -3/4$, u_y on $y = \pi/4$ and u_x on $x = \pi/4$ are given in Fig. 2.19. In Figs. 2.18 and 19, the straight lines in the graphs indicate the position of the cross sections. The velocity field with $T_a = 400$ is indicated in Figs. 2.20 and 21 in the same way with the cases of Figs. 2.18 and 19. Since horizontal plane $z = -3/4$ is located near the bottom boundary, the horizontal flow, which converges to the upward flow and diverges from the downward flow, is evidently

indicated. In the case of $T_a = 0$ roll-like convection contains one upward region and one downward region (Fig. 2.18(a) and Fig. 2.19(a)). The flow converges and diverges in the direction approximately perpendicular to the axis of the roll, that is, no remarkable vortex exists there. A typical convective pattern is shown in Fig. 2.18(b) where the cross section is almost perpendicular to the axis of the roll. Meanwhile, in the case of $T_a = 400$ the horizontal flow converges with counterclockwise rotation and diverges with clockwise rotation (Fig. 2.18(a)). Thus, the remarkable vortexes appear. These vortexes generated in the bottom region are carried to the upper region by the advection as discussed previously.

(c) Distribution of helicity density

The contour maps of the helicity density h for four cases, $T_a = 0, 25, 100$ and 400 on the horizontal plane $z = 0$ are shown in Fig. 2.22 where the interval between the contour lines is 100. As T_a increases, the absolute value of h becomes large and the horizontal scale of the distribution of h becomes small, reflecting the rotation effect on the convective motion. We present in Fig. 2.23 typical vertical distribution of h on a vertical plane though the distribution of h varies with different cross section. In all cases of $T_a = 0, 25, 100$ and 400 , the approximately symmetric distribution about the plane $z = 0$ is dominant because of the advection effect. The distribution of h_z on the same planes as Figs. 2.22 and 23 is given in Figs. 2.24 and 25, respectively. It is shown from the results given in these figures that the helical flow is effectively generated by the Coriolis force. The symmetric nature of h_z is clearly seen in Fig. 2.25.

Several quantities which characterize the velocity field, such as u_{rms} , ω_{rms} and $|H_z|$, are presented in Table 2.2. In the rotating case $|H_z|/(u_{rms}\omega_{rms})$ is larger than that of the non-rotating case though the kinetic energy is smaller than that in the non-rotating case,

reflecting the helical nature of the velocity field. The quantities at $t = 2$ are also given for the non-rotating case because of the oscillatory behavior of convection described above.

(d) Temperature field

The contour plot of the temperature field on the vertical plane at $y = \pi$ is shown in Fig. 2.26. Although the pattern of the contour map depends on selection of the cross section, we select here a typical case. The temperature field is distorted by convection and the gradient of the temperature becomes large in the vicinity of the boundaries and small near the mid-plane. In Fig. 2.27 the horizontally averaged temperature profile at $t = 4$ is indicated together with the thermal conduction profile $T(z) = -z$. In the case of $T_a = 0$, 25 and 100 the temperature gradient is slightly reversed near the mid-plane $z = 0$ though the gradient varies with time. The Nusselt numbers for four cases at $t=4$ is give in Table. 2.2.

2.4.3 Magnetic case

In this subsection we investigate the magnetic field generation by convection without and with rotation. The initial condition of the temperature field is the same as that of the non-magnetic case with the selection of complicated perturbation. A weak, uniform magnetic field is given as the initial magnetic field, i.e. $\mathbf{B}(t = 0) = (0.1, 0.1, 0)$. The Rayleigh number is set at 1000 as in non-magnetic case. Two cases, that is, non-rotating ($T_a = 0$) and rotating ($T_a = 100$) cases, are considered.

(a) Time evolution of kinetic and magnetic energies

The kinetic and magnetic energies as a function of time are shown in Figs. 2.28 and 29, respectively. Both for $T_a = 0$ and 100, the temporal change of the kinetic energy is almost the same as that in the non-magnetic case (Figs. 2.15 and 16) because the kinetic energy is much larger than the magnetic energy, the system is called kinematic.

In the non-rotating case, the total magnetic energy E_{Mtotal} increases to a value several times larger than the initial value, then decreases to a value comparable to the initial value (Fig. 2.29(a)). The oscillatory behavior of the magnetic energy is attributed to the oscillation of the velocity field (Fig. 2.28(a)). In the rotating case with $T_a = 100$, E_{Mtotal} increases and then saturates at a value smaller than that for $T_a = 0$ (Fig. 2.29(b)). However, E_{Mtotal} for $T_a = 100$ does not decrease in contrast with that for $T_a = 0$. The magnetic field in the case of $T_a = 100$ is supposed to be maintained by a dynamo action. In the present simulation, among the three components of the magnetic energy, E_{Mz} is a good indicator of the generation effect of the fluid motion. At $t = 0$ only horizontal magnetic field exists, i.e. $E_{Mz} = 0$ and the fluid is at rest. With time passage, the velocity increases to a saturation level. The initial growth of the magnetic field is associated with this initial growth of the velocity field. After the initial stage the magnetic energy might be difficult to keep unless there is a generation effect of the magnetic field in the system (Fig. 2.29(a)). Although the growth of the magnetic energy is very small and the system is far from magnetohydrodynamic state, the effect of rotation on the magnetic field generation could be seen in the present simulation (Fig. 2.29(b)). The mechanism of the magnetic field generation is largely related to the helical flow due to the Coriolis force.

(b) Velocity and magnetic fields

In Figs. 2.30 and 31 the velocity field \mathbf{u} at $t = 4$ on the horizontal plane at $z = 0$ is shown for $T_a = 0$ and 100. These patterns are almost the same with those of the non-magnetic case (Figs. 2.16(a) and (c) and Figs. 2.17(a) and (c)) because the system is basically kinematic. In the rotating case apparent vortexes, together with the vertical flow, generate the helical flow. The contour map of h on the plane at $z = 0$ is given in Fig. 2.32 that is given in the way similar to Figs. 2.22(a) and (b). In Fig. 2.33, the contour plot of h_z on the plane at $z = 0$ is indicated. The magnetic field \mathbf{B} in the plane at $z = 0$ at $t = 4$ is shown in Fig. 2.34 both for the non-rotating and rotating cases. In the rotating case, the vortex structure of the magnetic field becomes apparent with J_z even though the vortexes of the field are not so remarkable as those of the velocity field. This vortex structure of \mathbf{B} is, however, not seen in the non-rotating case (Fig. 2.34(a)). The contour map of B_z on the plane at $z = 0$ is given in Fig. 2.35 where the intervals of the contour lines are 0.02 for the non-rotating case (Fig. 2.34(a)) and 0.04 for the rotating case (Fig. 2.35(b)). As described previously, B_z is a good indicator of the magnetic field generation in this calculation. Since we assume that the conducting fluid is adjoining the perfect conductor at top and bottom boundaries, B_z becomes large in the middle region near $z = 0$. In the rotating case, B_z is large compared with that of the non-rotating case. The region with large B_z is localized, and B_z becomes large associated with the helical flow though the helical flow does not always accompany B_z (Figs. 2.30(b) and 31(b)). In Fig. 2.36, \mathbf{B} on the vertical plane $y = 0$ at $t = 4$ is indicated. Because of the boundary condition for \mathbf{B} , i.e. $B_z = 0$ on the plane $z = \pm 1$, magnetic expulsion that is pointed out as a common feature of magnetoconvection (Weiss, 1966 ; Galloway and Weiss 1981), is not outstanding.

(c) Geometric relation between the velocity and magnetic field vectors

The relation between \mathbf{u} and \mathbf{B} vectors can be effectively expressed by a histogram for $\cos \theta$, where θ is an angle between \mathbf{u} and \mathbf{B} vectors at a spatial point; i.e. $\cos \theta (= \mathbf{u} \cdot \mathbf{B} / (|\mathbf{u}| |\mathbf{B}|))$. In the histogram the occurrence frequency is normalized so that the distribution of the occurrence frequency would be uniform when θ is distributed uniformly from 0 to 2π . In Fig. 2.37 the histograms of $\cos \theta$ for all spatial points in the simulation box are given at four different times, i.e. $t = 1, 2, 3$ and 4. In the non-rotating case (Fig. 2.37(a)) the temporal variation of the distribution of $\cos \theta$ is remarkable, that is, the occurrence frequency for given $\cos \theta$ in the vicinity of zero, i.e. $\theta = \pi/2$ becomes large, indicating that \mathbf{u} and \mathbf{B} tend to be perpendicular to each other as time passes. It is well known that similar situation appears when the strong, uniform, horizontal magnetic field exists, that is, due to the effect of the magnetic field on convection, 2-dimensional convective roll, whose axis is parallel to the uniform magnetic field, appears (Chandrasekhar, 1961). Although the magnetic energy is much smaller than the kinetic energy in the present situation, the existence of 2-dimensional roll-like convection makes the magnetic field parallel to the axis of the roll. Meanwhile, in the rotating case (Fig. 2.37(b)) the temporal change of the distribution is small and an approximately uniform distribution of the occurrence frequency for given $\cos \theta$ appears in contrast with the peak at $\theta = \pi/2$ for the non-rotating case. This configuration of \mathbf{u} and \mathbf{B} in the rotating case leads to the magnetic field generation through the induction term $\nabla \times (\mathbf{u} \times \mathbf{B})$. In Fig. 2.38 histogram for only the spatial points, which satisfy the condition $|\mathbf{u}| \geq u_{rms}$, are given in order to remove the noisy level. Thus, the relation between \mathbf{u} and \mathbf{B} , which is associated with the cross helicity $\int \mathbf{u} \cdot \mathbf{B} dV$, has been studied by using these histograms.

The relation between \mathbf{u} and $\boldsymbol{\omega}$ which is related to the kinetic helicity $\int \mathbf{u} \cdot \boldsymbol{\omega} dV$ is also studied by obtaining the histogram for $\cos \theta (= \mathbf{u} \cdot \boldsymbol{\omega} / (|\mathbf{u}| |\boldsymbol{\omega}|))$ as given in Fig. 2.39 where the occurrence frequency for $\cos \theta$ are analyzed for all spatial points. In the non-rotating case central peaks of the occurrence frequency are dominant, reflecting the 2-dimensional roll-like convective pattern. The value of the peak varies with time because of the oscillation of the roll. Central peaks also exists in the rotating case (Fig. 2.39(b)). However, the value of the peak is smaller than that of the non-rotating case and the temporal change is not remarkable. In addition, the distribution of $\cos \theta$ occurrence is broad compared with that of the non-rotating case, indicating the dominantly helical structure of the convective motion in the rotating case, In Fig. 2.40 similar histogram is given for $\cos \theta (= \mathbf{B} \cdot \mathbf{J} / (|\mathbf{B}| |\mathbf{J}|))$ to see the relation between \mathbf{B} and \mathbf{J} which is related to a helicity $\int \mathbf{B} \cdot \mathbf{J} dV$. Both for the non-rotating and rotating case remarkable central peaks exists, the distributions of the occurrence frequency at different time are similar except for $t = 1$. The helical nature of $\int \mathbf{B}$ for the rotating case is not clear compared with that of \mathbf{u} as given in Fig. 2.39. This is considered as the results of the initial and boundary conditions for \mathbf{B} and the moderate value of the magnetic Prandtl number.

(d) Kinetic and magnetic energy spectra

In Fig. 2.41 we show the kinetic and magnetic energy spectrum as a function of the horizontal wavenumber k_{\perp} for $T_a = 100$ at $t = 4$. Two energies decrease exponentially as k_{\perp} increases, reflecting the large-scale nature of the velocity and magnetic field. Both energies show the largest amplitude for the mode $k_{\perp} = 1$. The ratio of the amplitude of the higher mode to that of the lower one is a little larger in the magnetic energy than in

the kinetic energy, indicating that the characteristic scale of the magnetic field is smaller than that of the velocity field.



Figure 3.1: The region of the magnetic simulation. The regular velocity domain is assumed to be well parallel to the gravity vector. The temperature of the top boundary is $T = 1$ and that of the bottom is fixed $T = 0$.

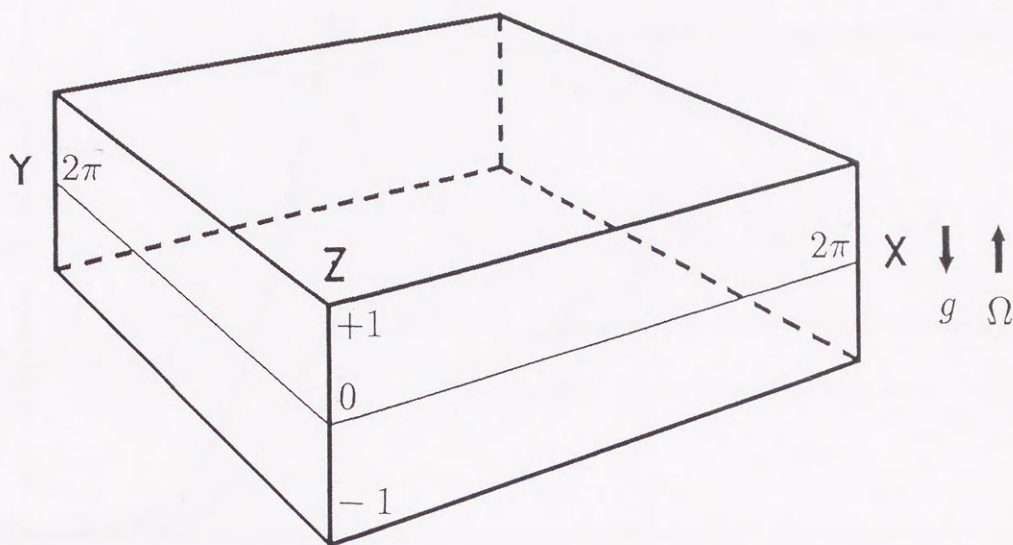


Figure 2.1 The region of the computer simulation. The angular velocity vector is assumed to be anti-parallel to the gravity vector. The temperature of the top boundary ($z=+1$) is -1 and that of the bottom ($z=-1$) is $+1$.

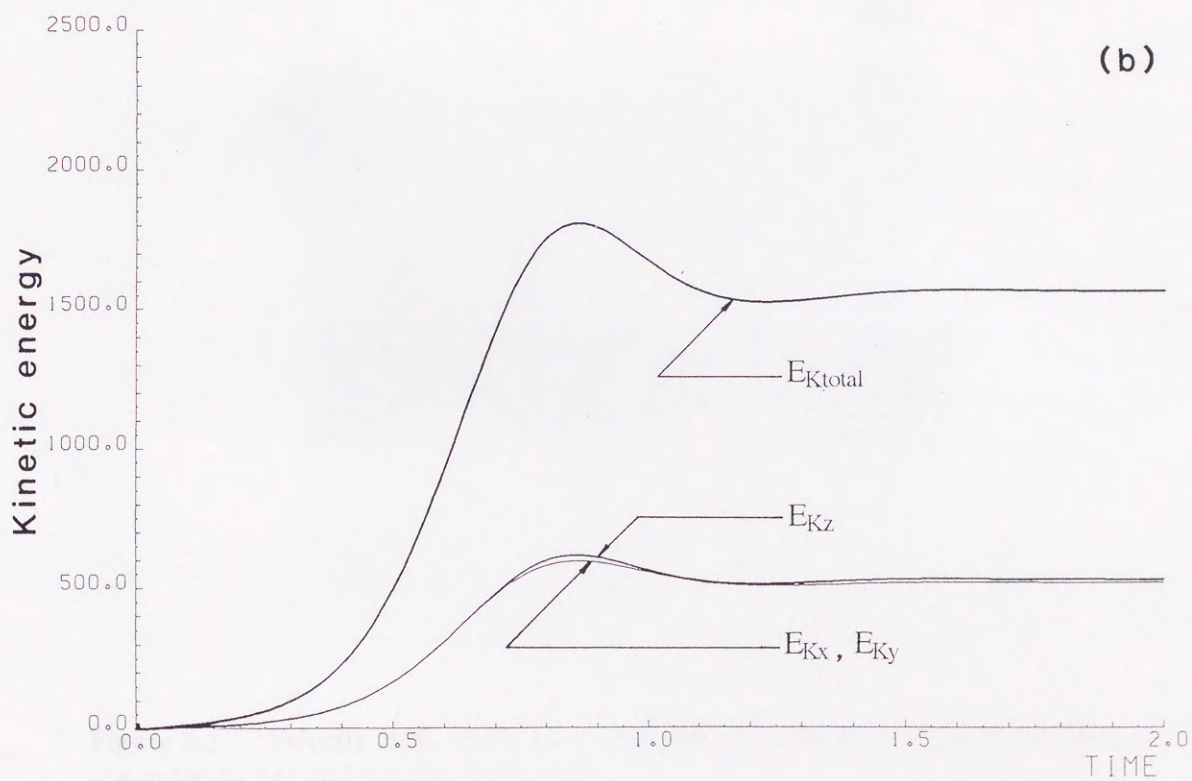
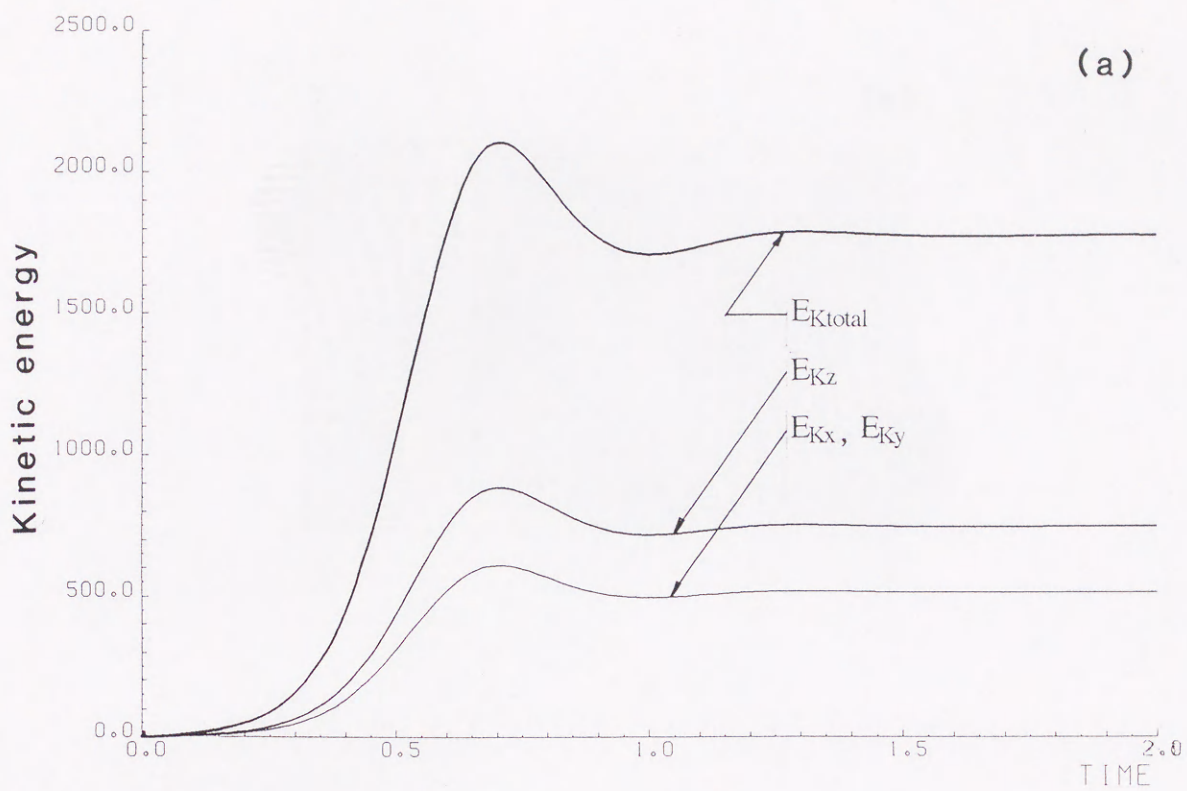


Figure 2.2 Time evolution of the kinetic energy for the non-rotating (a) and rotating (b) cases.

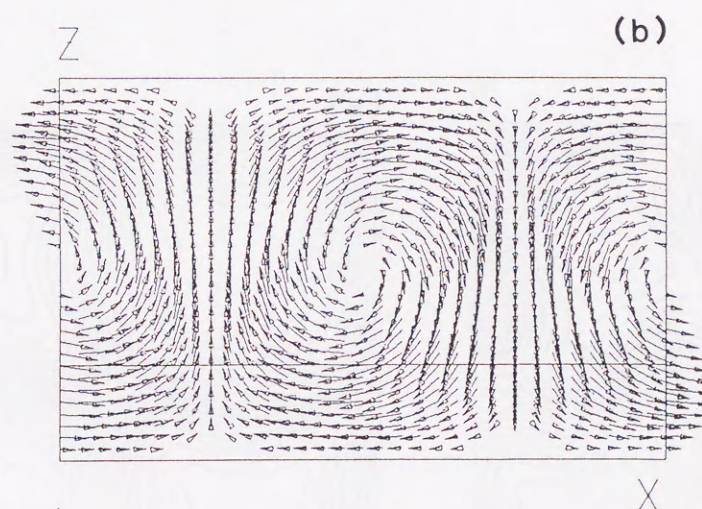
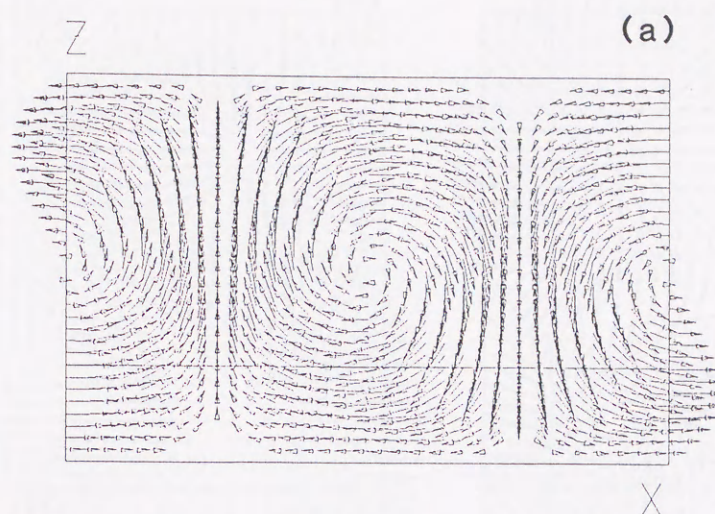


Figure 2.3 Velocity field vector on the vertical plane at $y = \pi/2$ at $t = 2$ for the non-rotating (a) and rotating (b) cases.

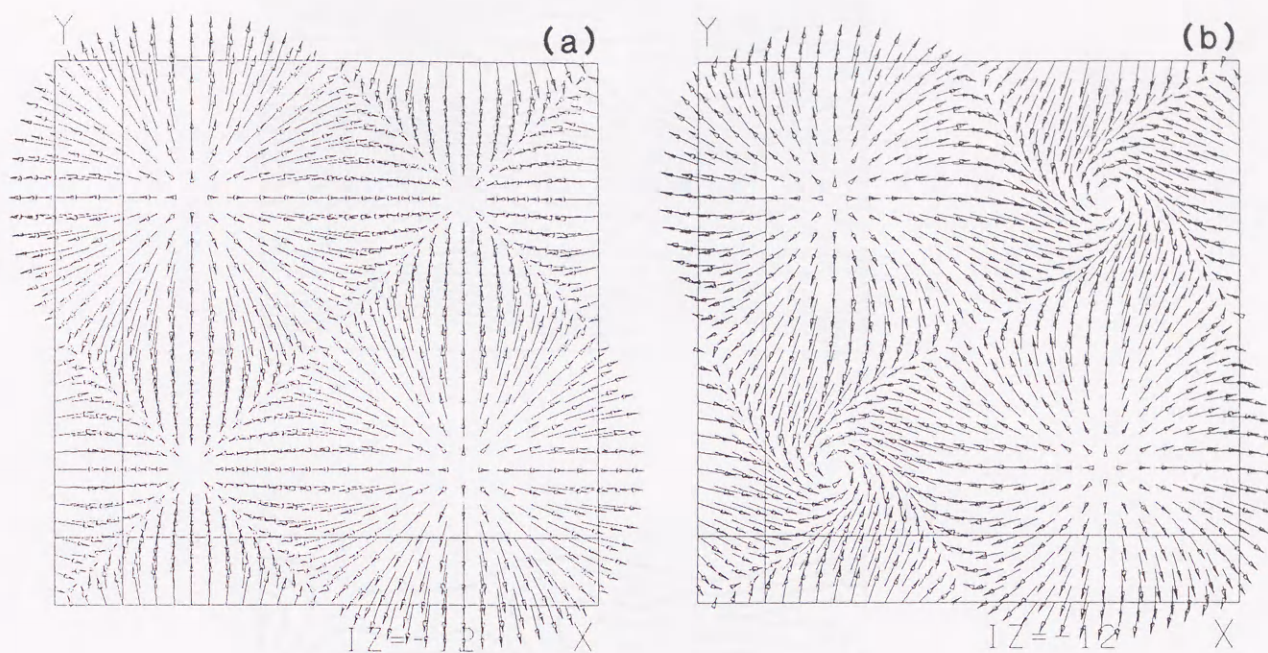


Figure 2.4 Velocity field vector on the horizontal plane at $z = 0$ at $t = 2$ for the non-rotating (a) and rotating (b) cases.

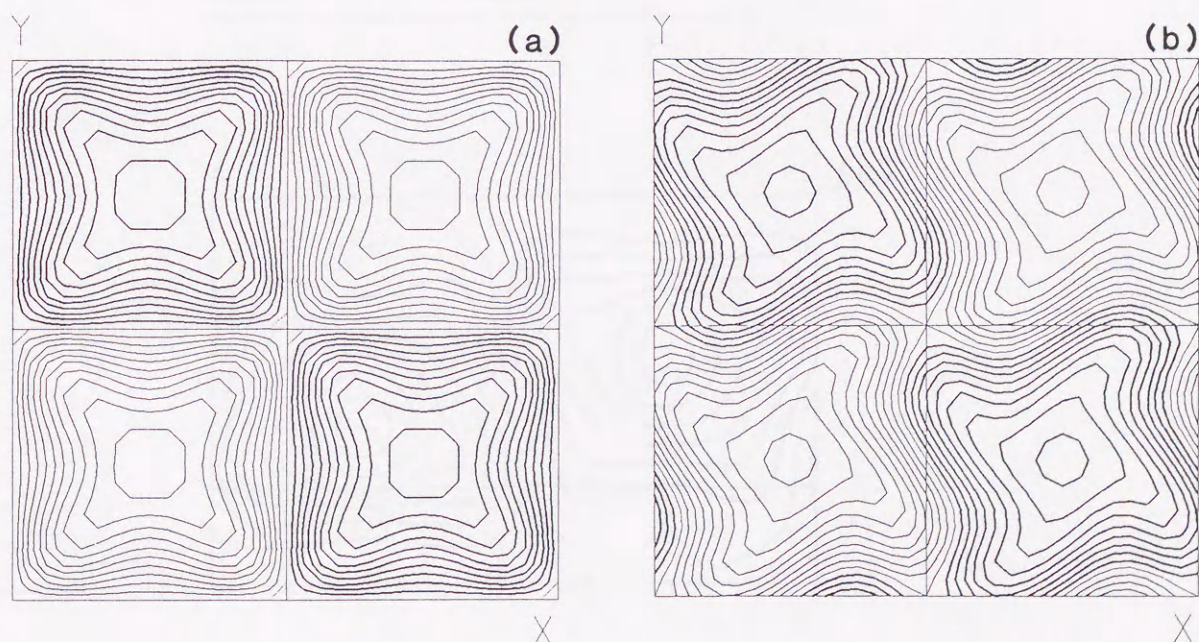


Figure 2.5 Contour plots of u_z on the horizontal plane at $z = 0$ at $t = 2$ for the non-rotating (a) and rotating (b) cases. The interval between the contour lines is 1. Thin lines represent positive values, thick lines positive values and thinnest line zero value.

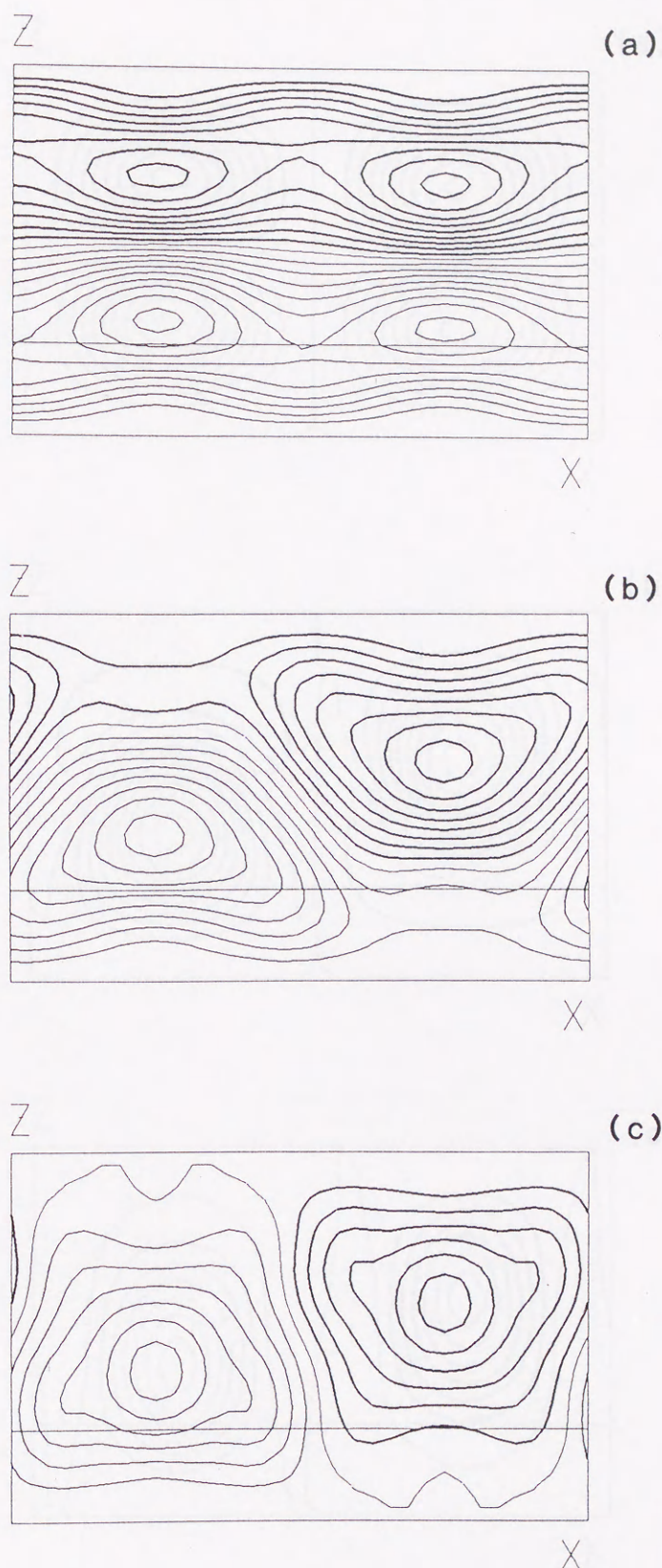


Figure 2.6 Contour plots of h in the vertical plane at $y = \pi/2$ for three different times, $t = 0.1$ (a), 0.5 (b) and 2.0 (c). The intervals between contour lines are 0.05 (a), 5 (b) and 40 (c). Thin lines represent positive values, thick lines positive values and thinnest line zero value.

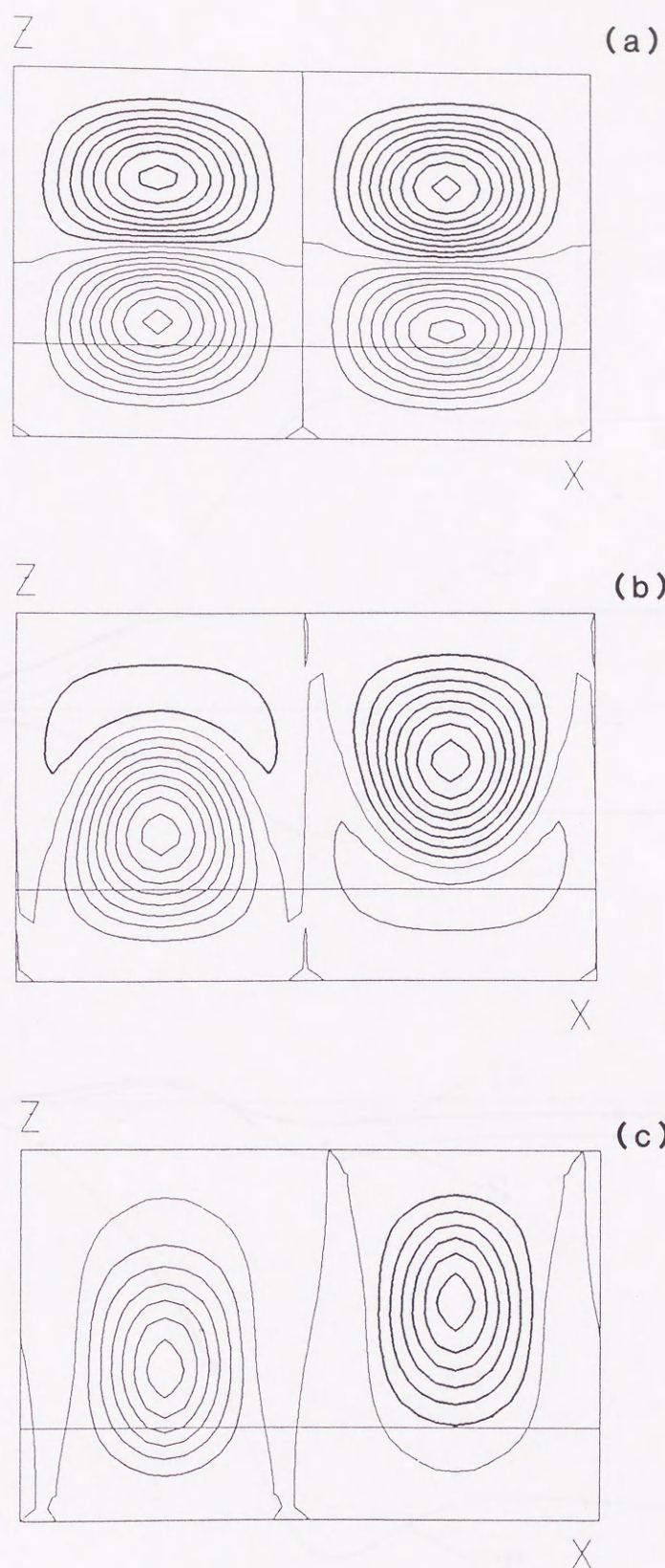


Figure 2.7 Contour plots of h_z . Same conditions as in Fig. 2.6.

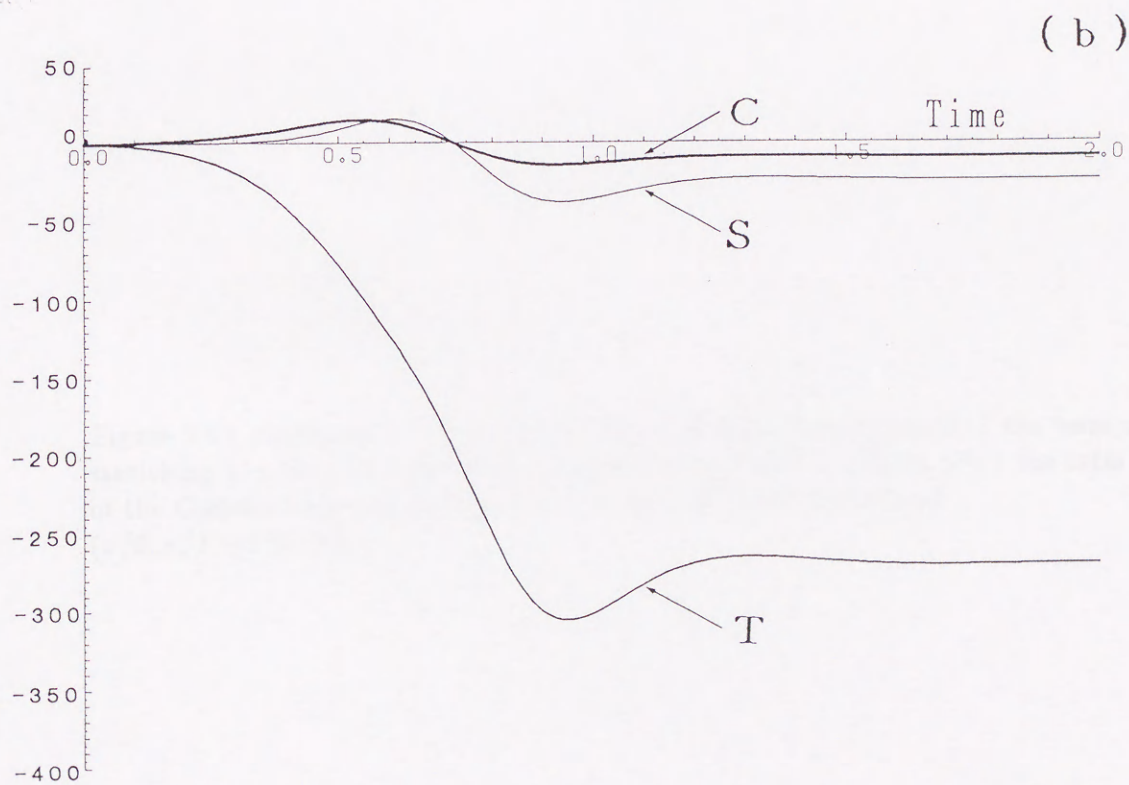
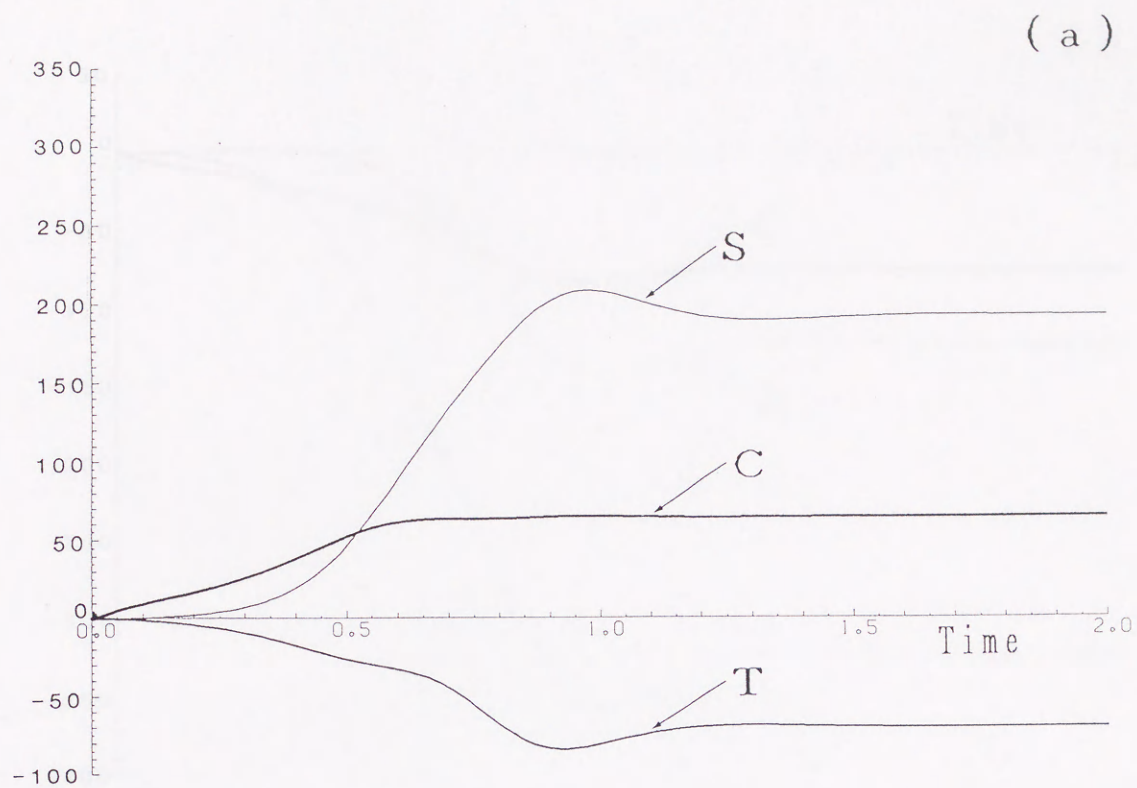


Figure 2.8 For caption see next page.

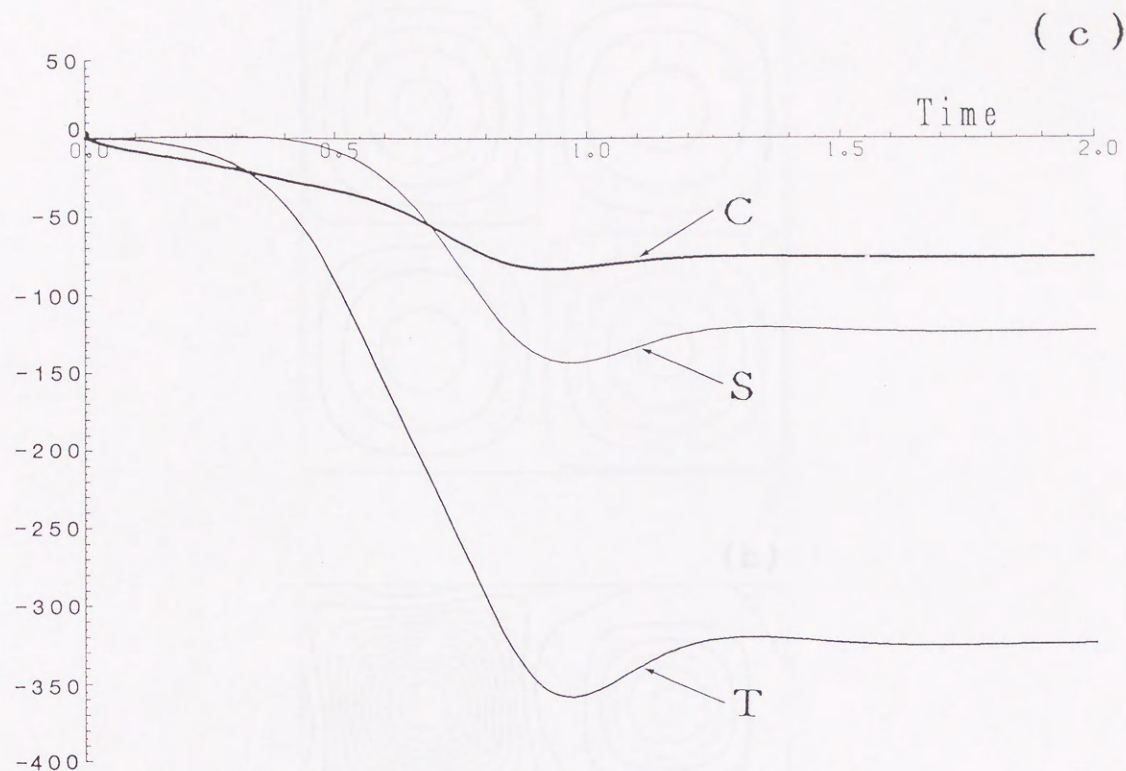


Figure 2.8 (continued) Time evolution of three terms, $\omega_z \partial u_z / \partial z$ (the term of stretching), $u_z \partial \omega_z / \partial z$ (the term of transporting) and $P_r \sqrt{T_a} \partial u_z / \partial z$ (the term of the Coriolis force) at $(\pi/2, \pi/2, -1/4)$ (a), $(\pi/2, \pi/2, 0)$ (b) and $(\pi/2, \pi/2, +1/4)$ (c).

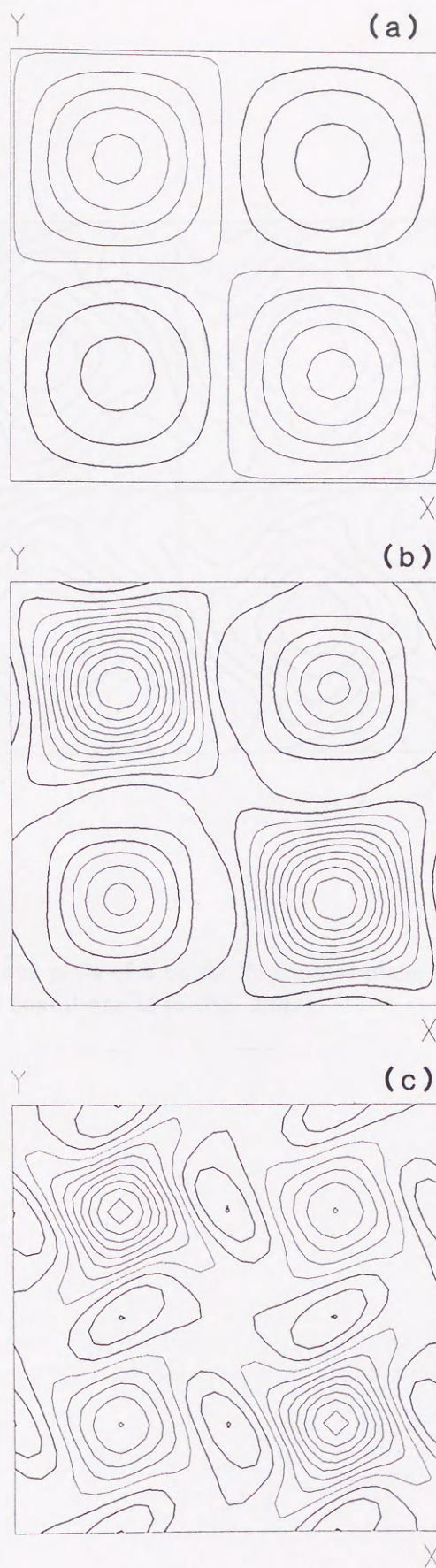


Figure 2.9 Contour plots of ω_z in the horizontal plane at $z = 0.25$ for three different times, $t = 0.1(a)$, $0.5(b)$ and $2.0(c)$. The intervals between contour lines are 0.1 (a), 1 (b) and 4 (c). Thin lines represent positive values, thick lines positive values and thinnest line zero value.

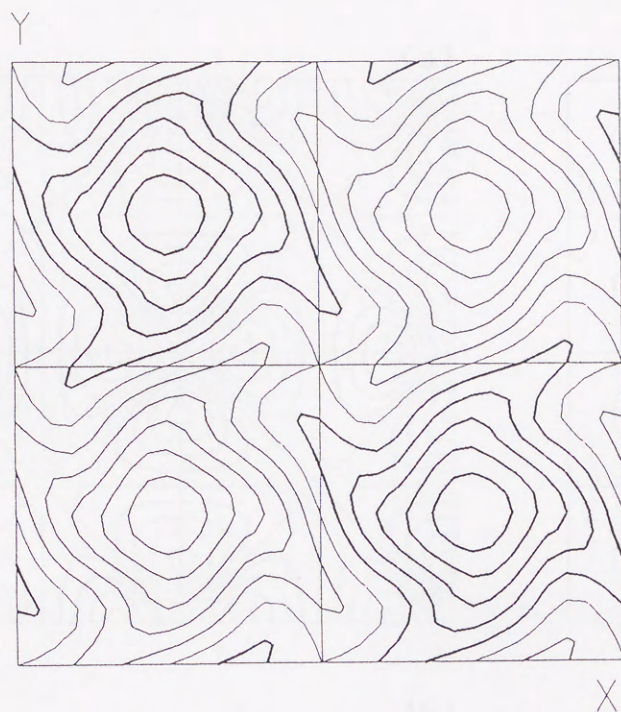


Figure 2.10 Contour plots of h on the horizontal plane at $z = 0$ at $t = 2$ for the rotating case. Same conditions as in Fig. 2.6(c).

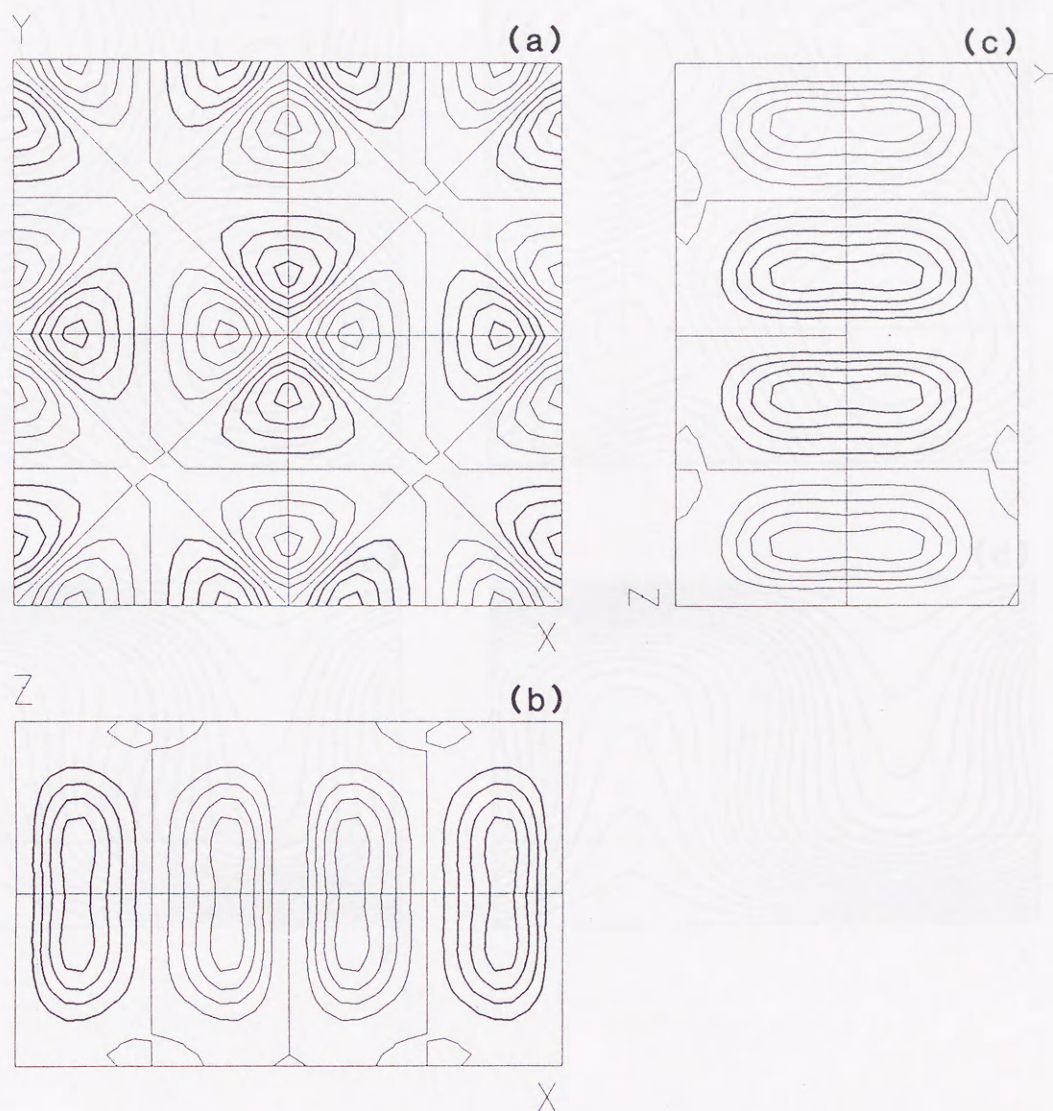


Figure 2.11 Contour plots of h on the planes at $z = 0$, $y = \pi/2$ and $x = \pi/2$ at $t = 2$ for the non-rotating case. The interval between contour lines is 20.

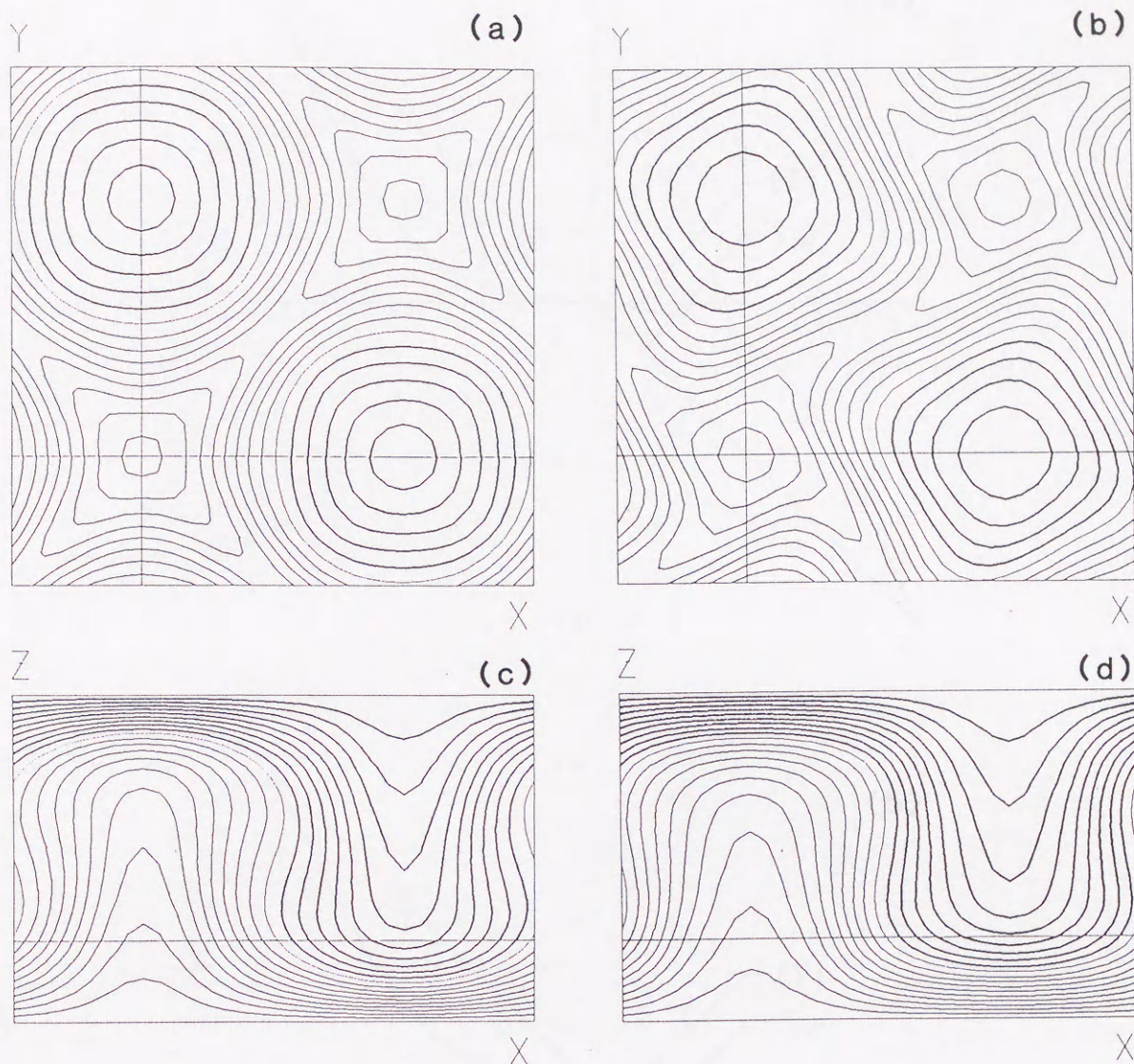


Figure 2.12 Contour maps of the temperature field at $t=2$ on the plane at $z = -3/4$ for the non-rotating (a) and rotating (b) case and on the plane at $y = \pi/2$ for the non-rotating (c) and rotating (d) case.

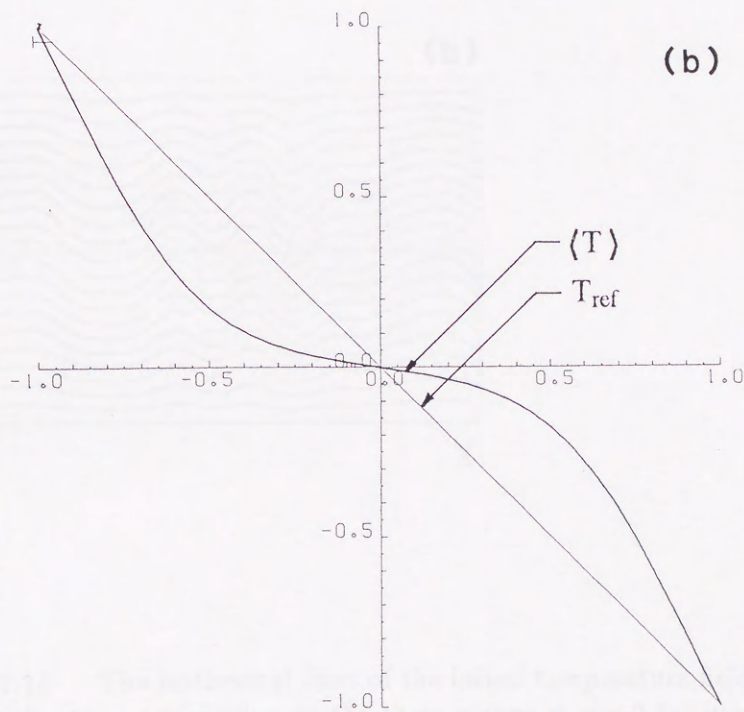
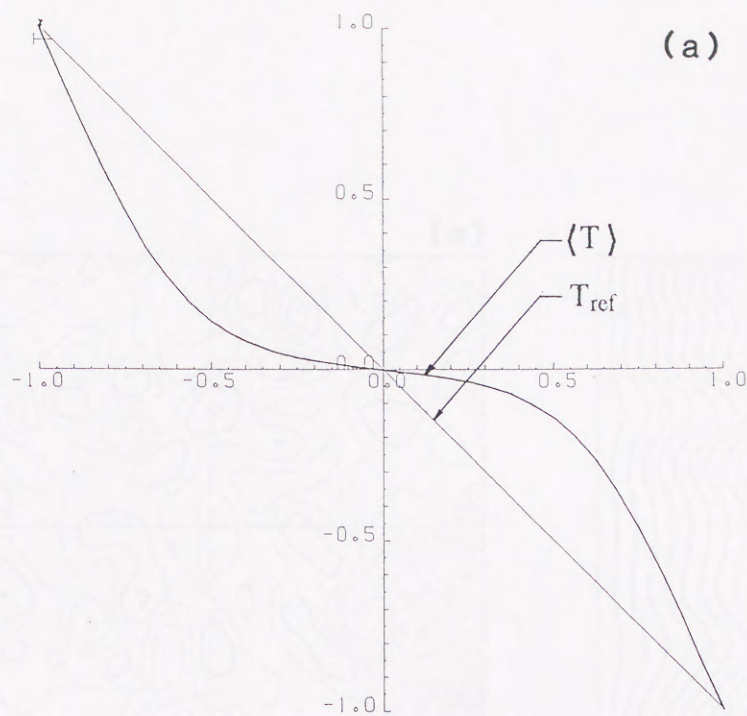


Figure 2.13 Horizontally averaged temperature field $\langle T(z) \rangle$ at $t = 2$ for the non-rotating (a) and rotating case (b) together with the thermal conduction profile $T_{ref} = -z$.

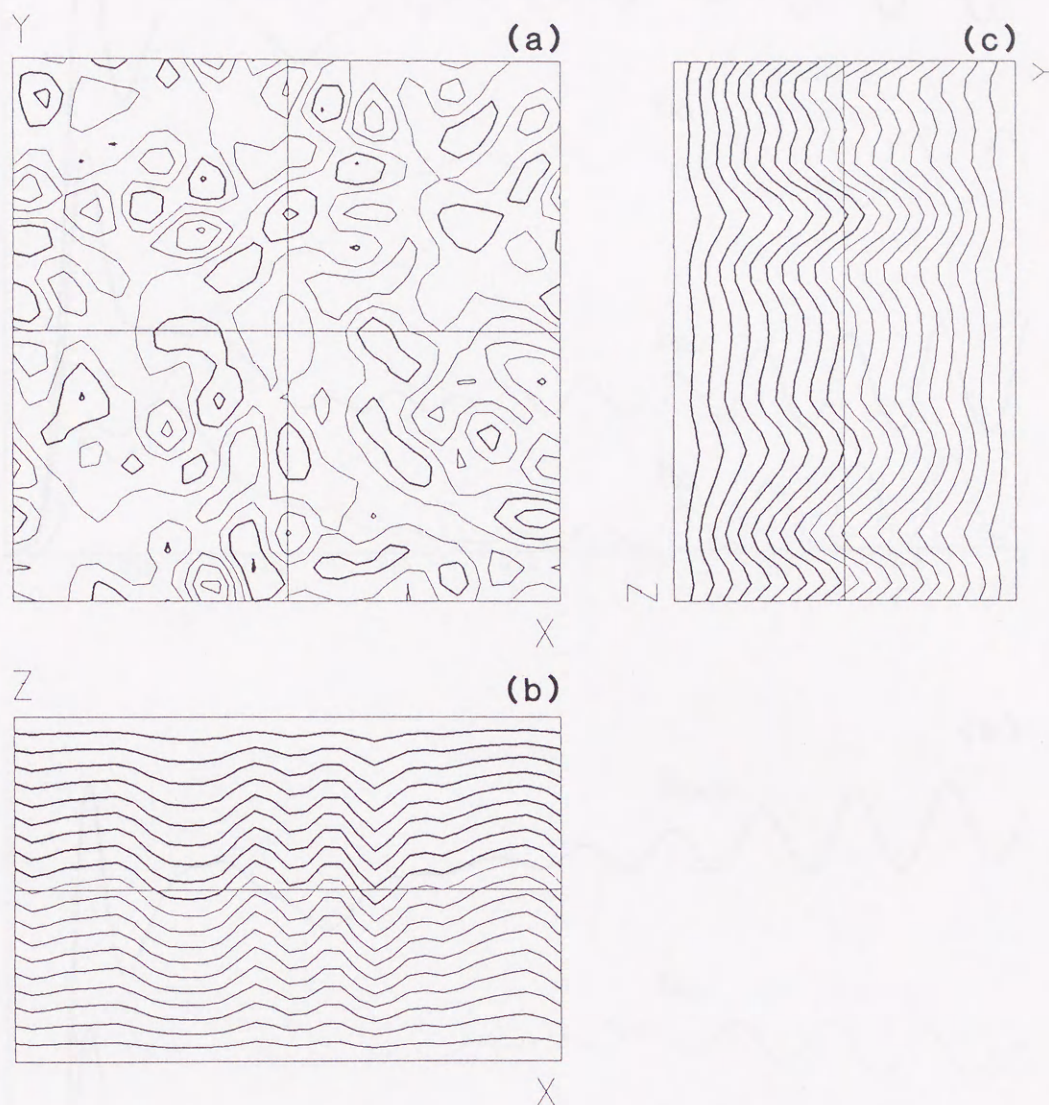


Figure 2.14 The isothermal lines of the initial temperature field for the case of the complicated perturbation on the three planes at $z = 0$ (a), $y = \pi/2$ (b) and $x = \pi/2$ (c). The interval between the isothermal lines is 0.1.

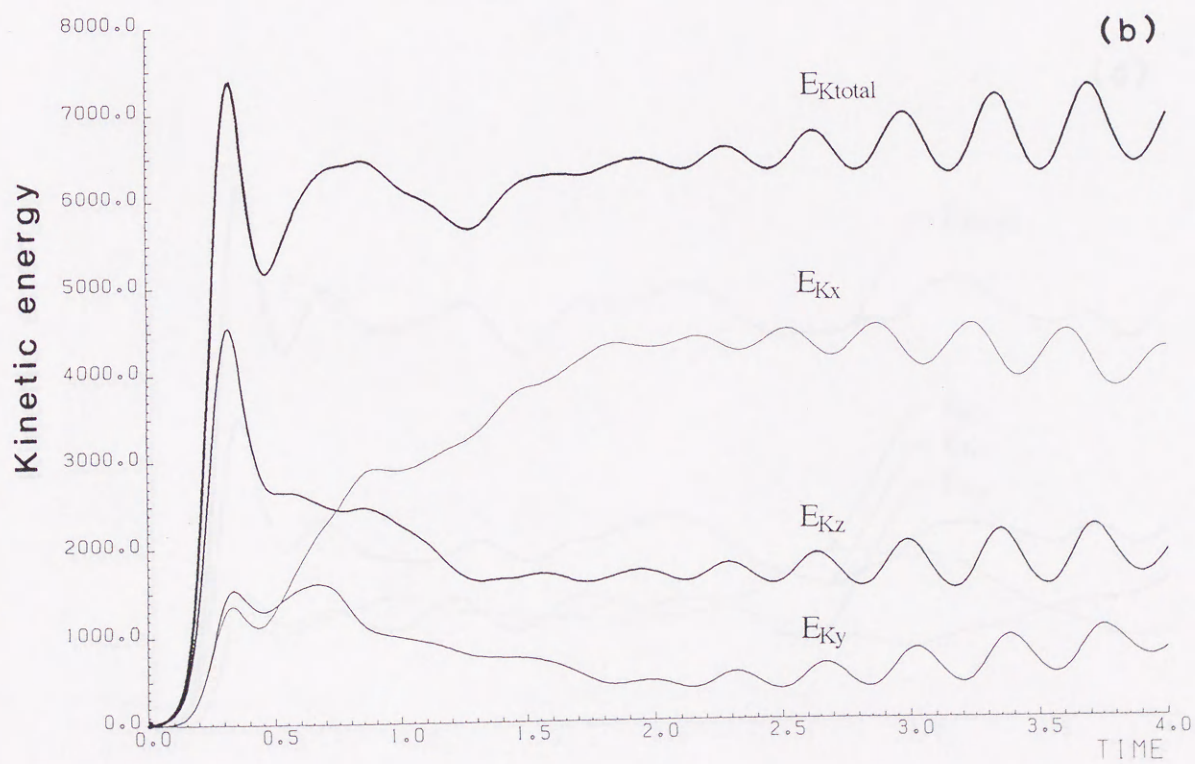
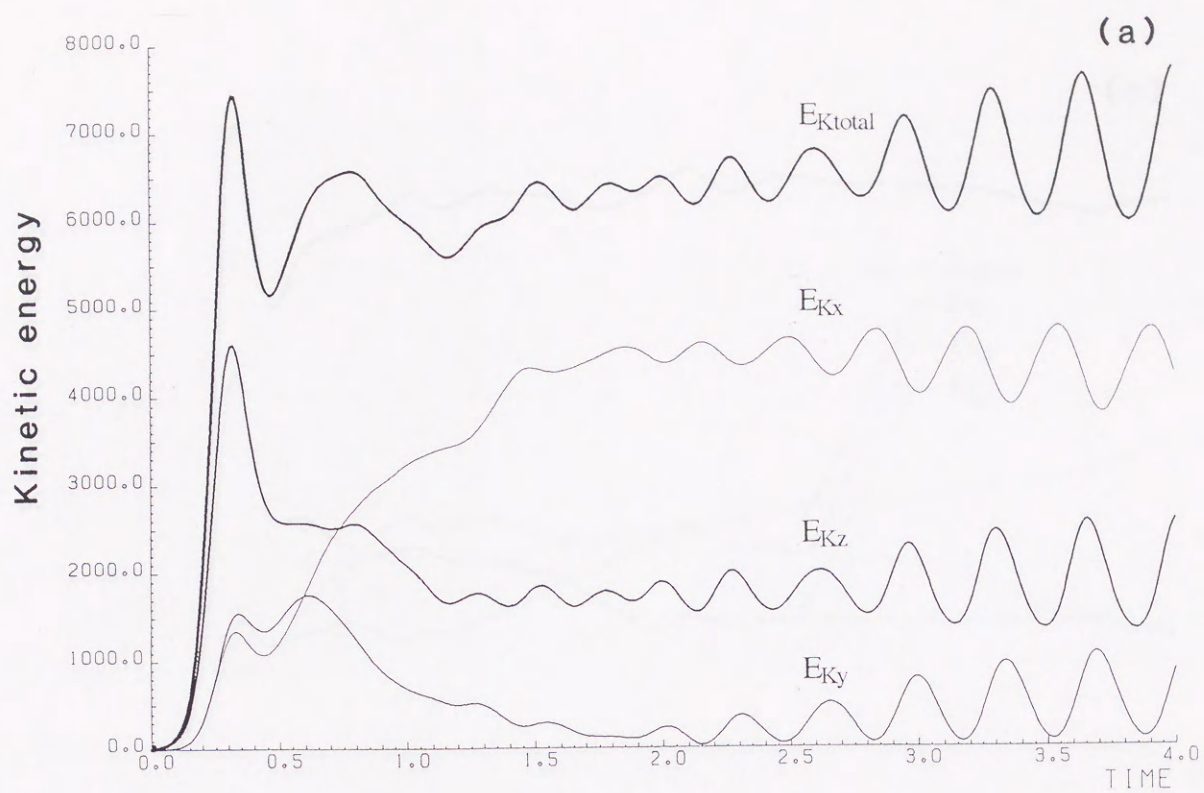


Figure 2.15 For caption see next page.

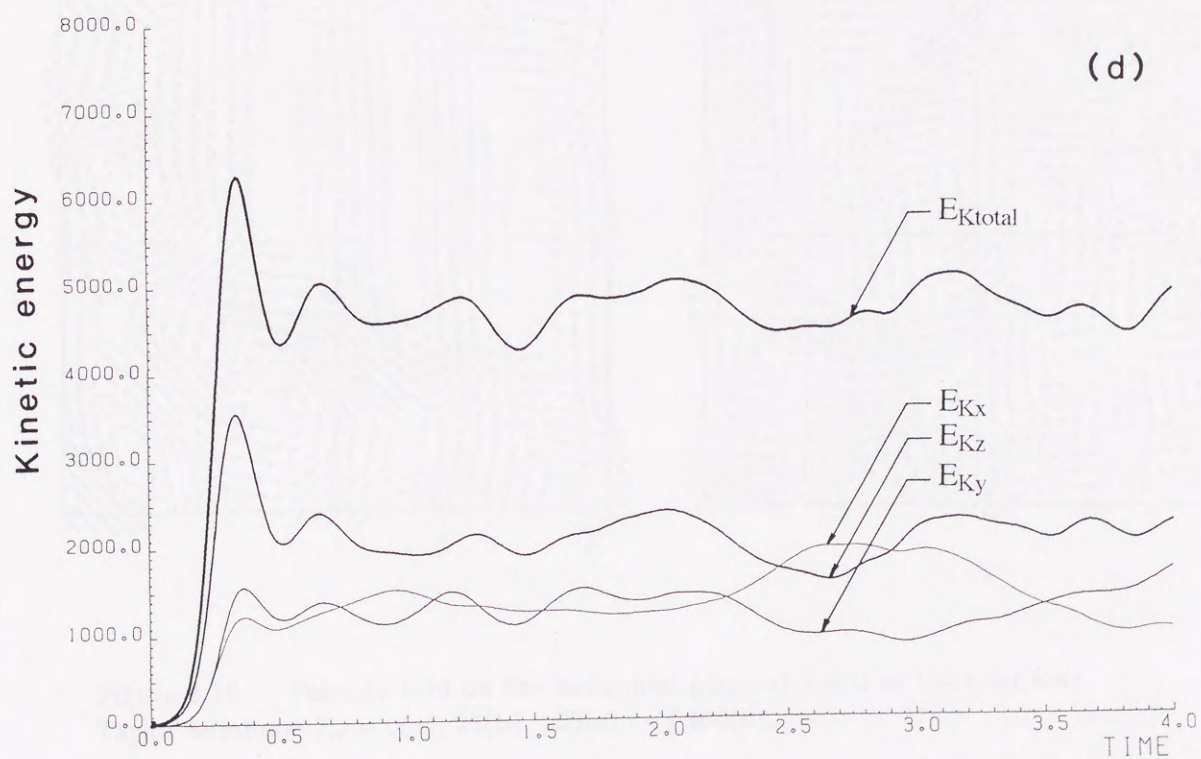
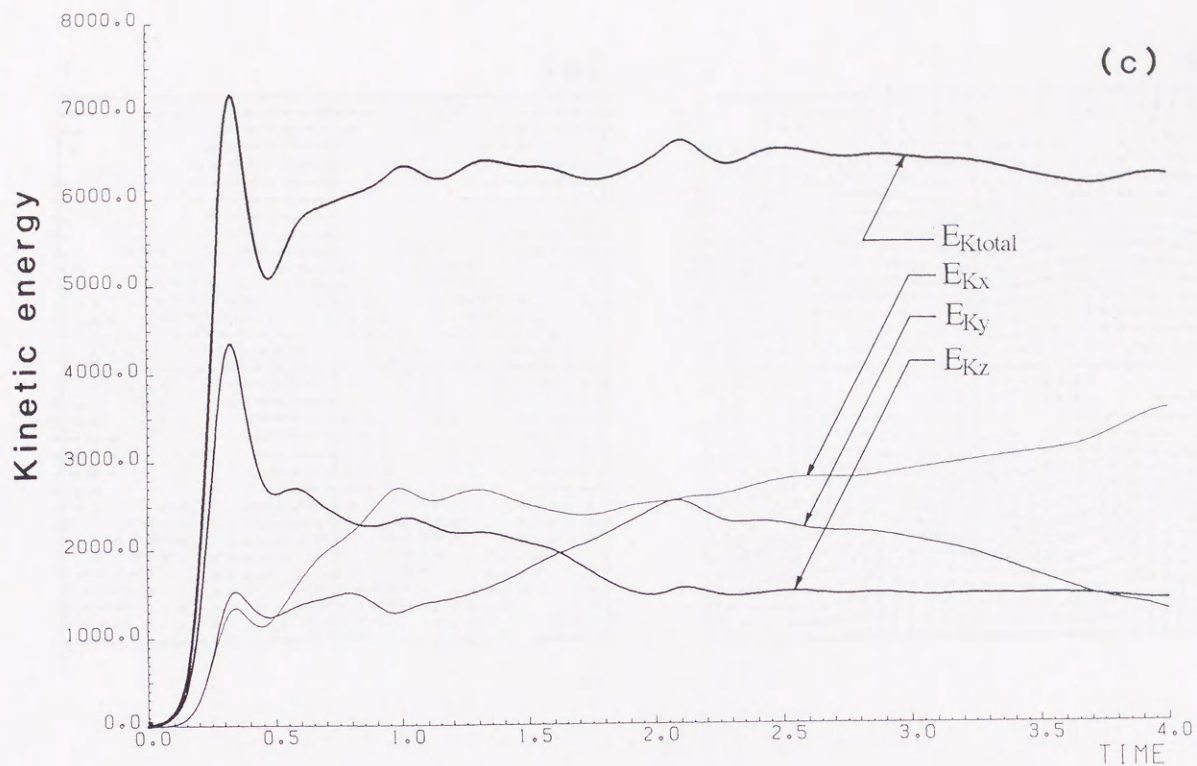


Figure 2.15 (continued) Time evolution of the kinetic energy for four Taylor numbers, $T_a = 0$ (a), 25 (b), 100 (c) and 400 (d).

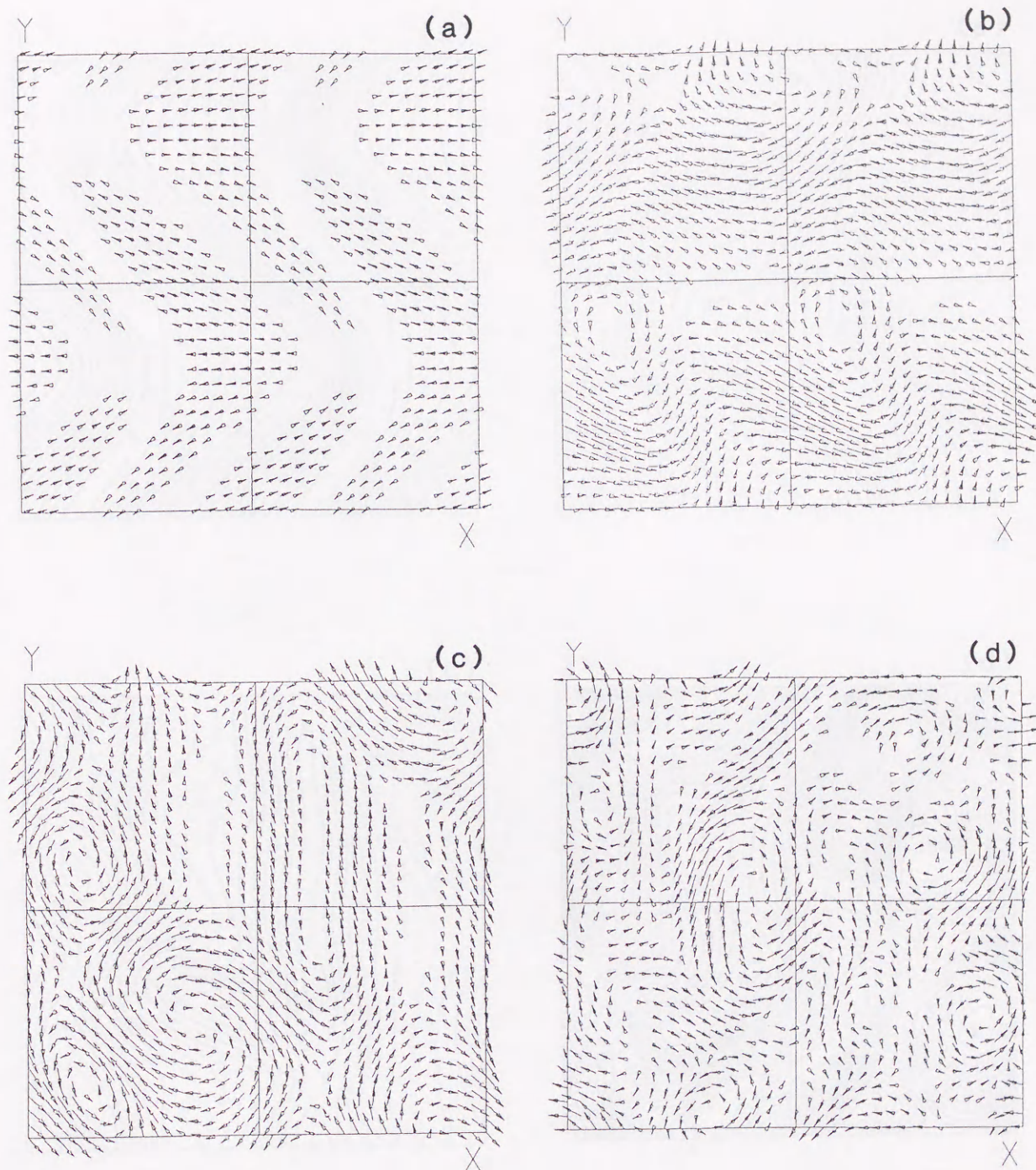


Figure 2.16 Velocity field on the horizontal plane at $z = 0$ at $t = 4$ for four Taylor numbers, $T_a = 0$ (a), 25(b), 100(c) and 400(d).

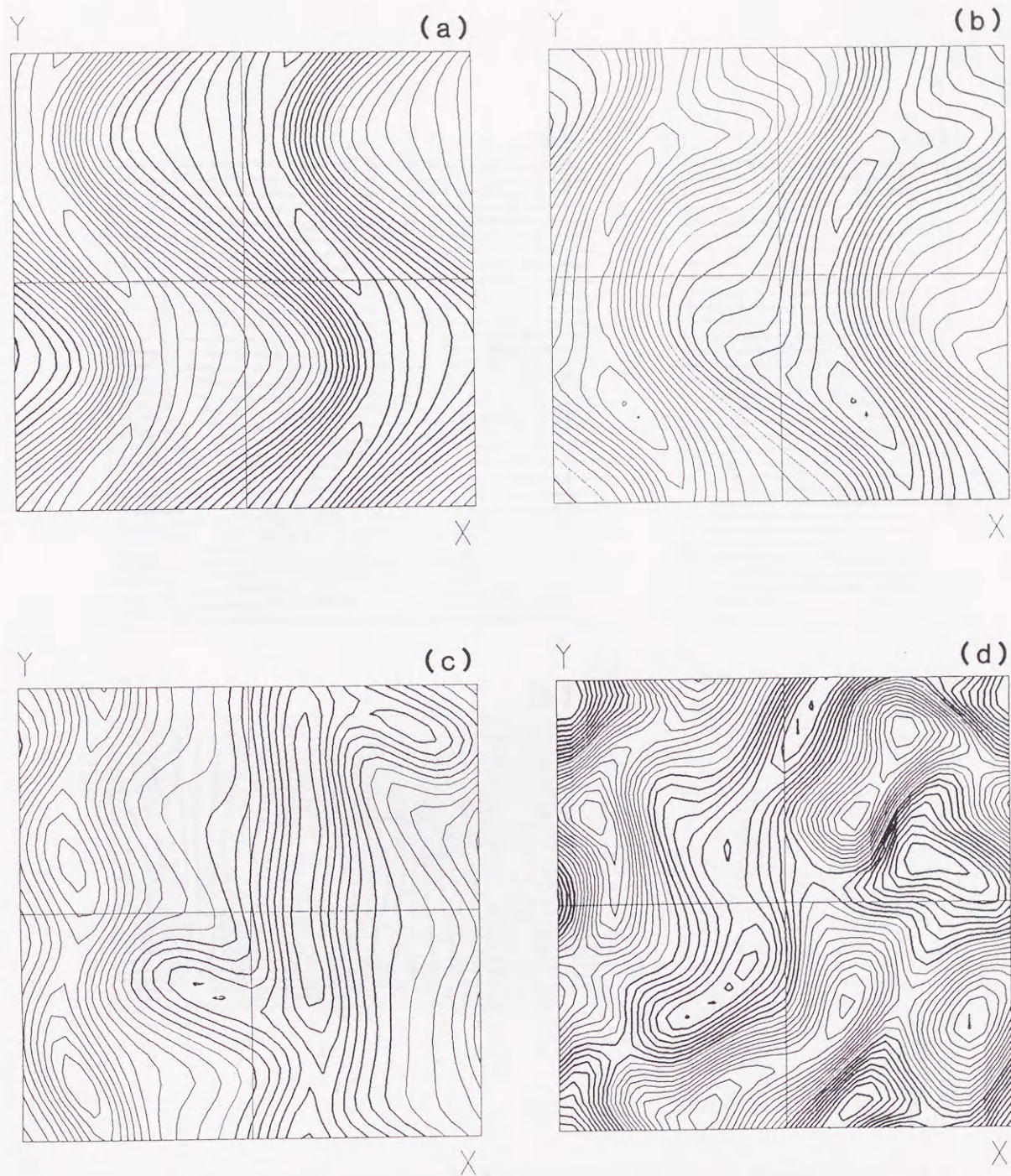


Figure 2.17 Contour plots of u_z . Same conditions as in Fig. 2.16. The interval of the contour lines is 2.

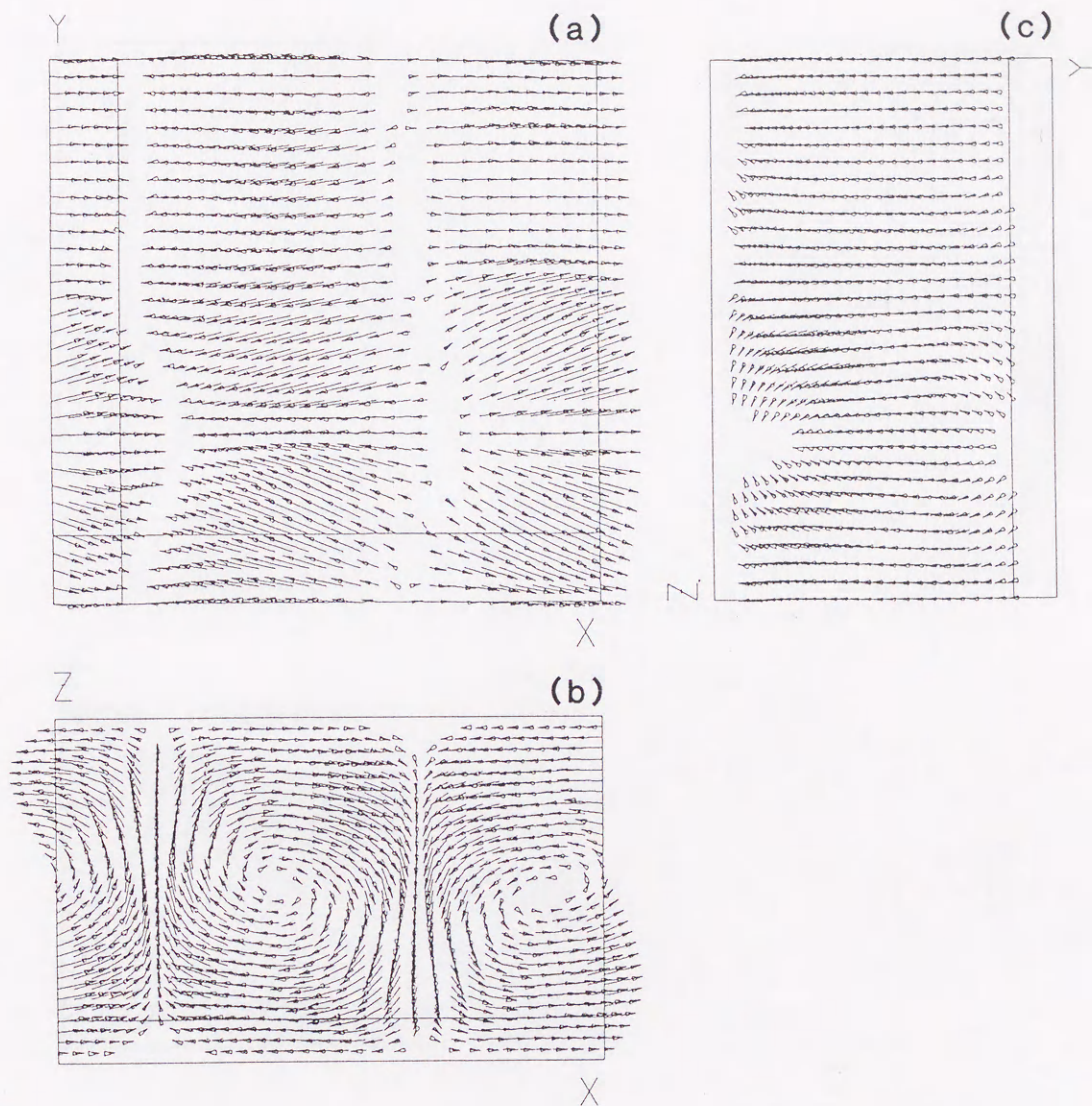


Figure 2.18 Velocity field for the non-rotating case on the planes at $z = -3/4$ (a), $y = \pi/4$ (b) and $x = \pi/4$ (c) at $t=4$. The straight lines in the graphs indicate the position of the cross sections.

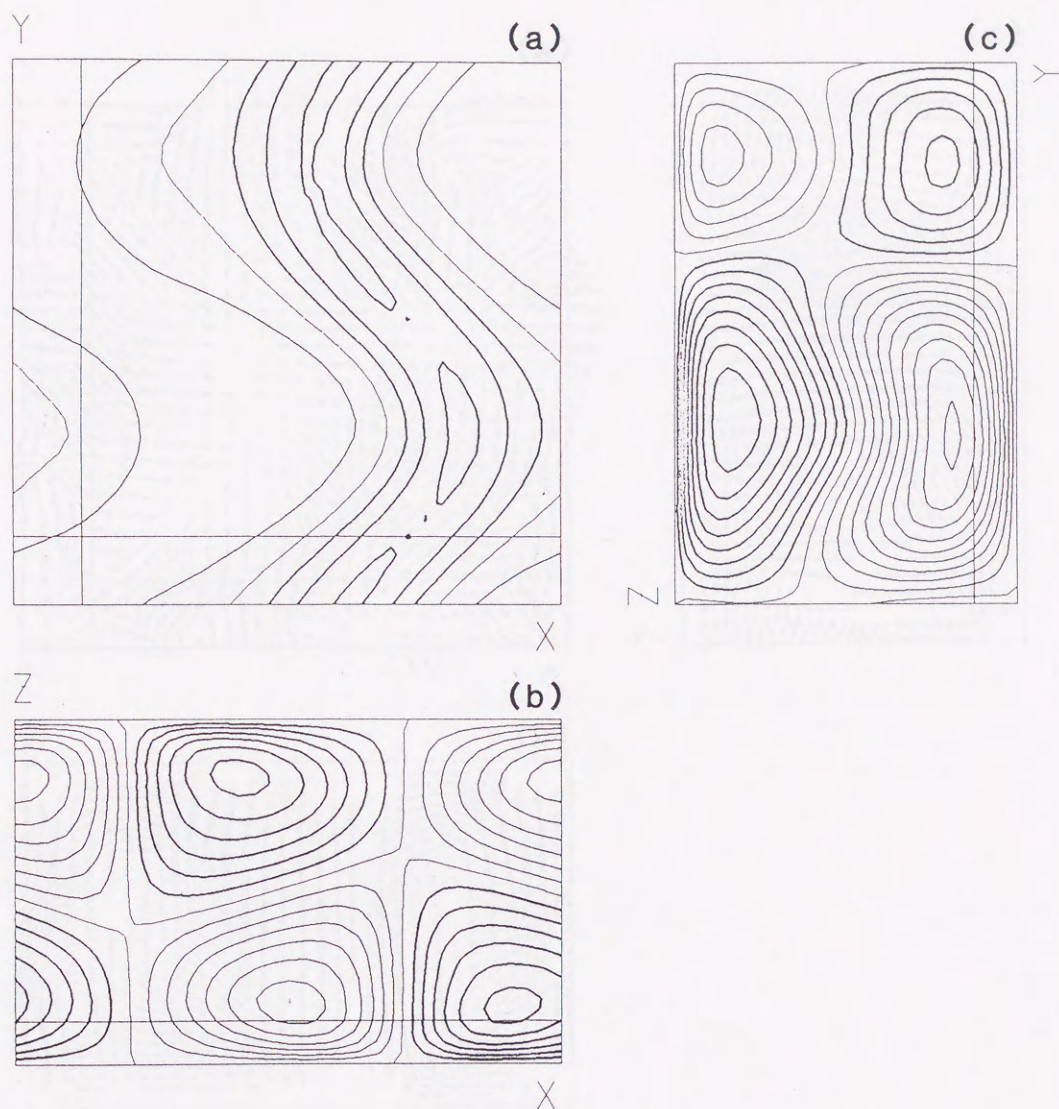


Figure 2.19 Contour maps of u_z (a), u_y (b) and u_x (c) for the non-rotating case. Same conditions as in Fig. 2.18.

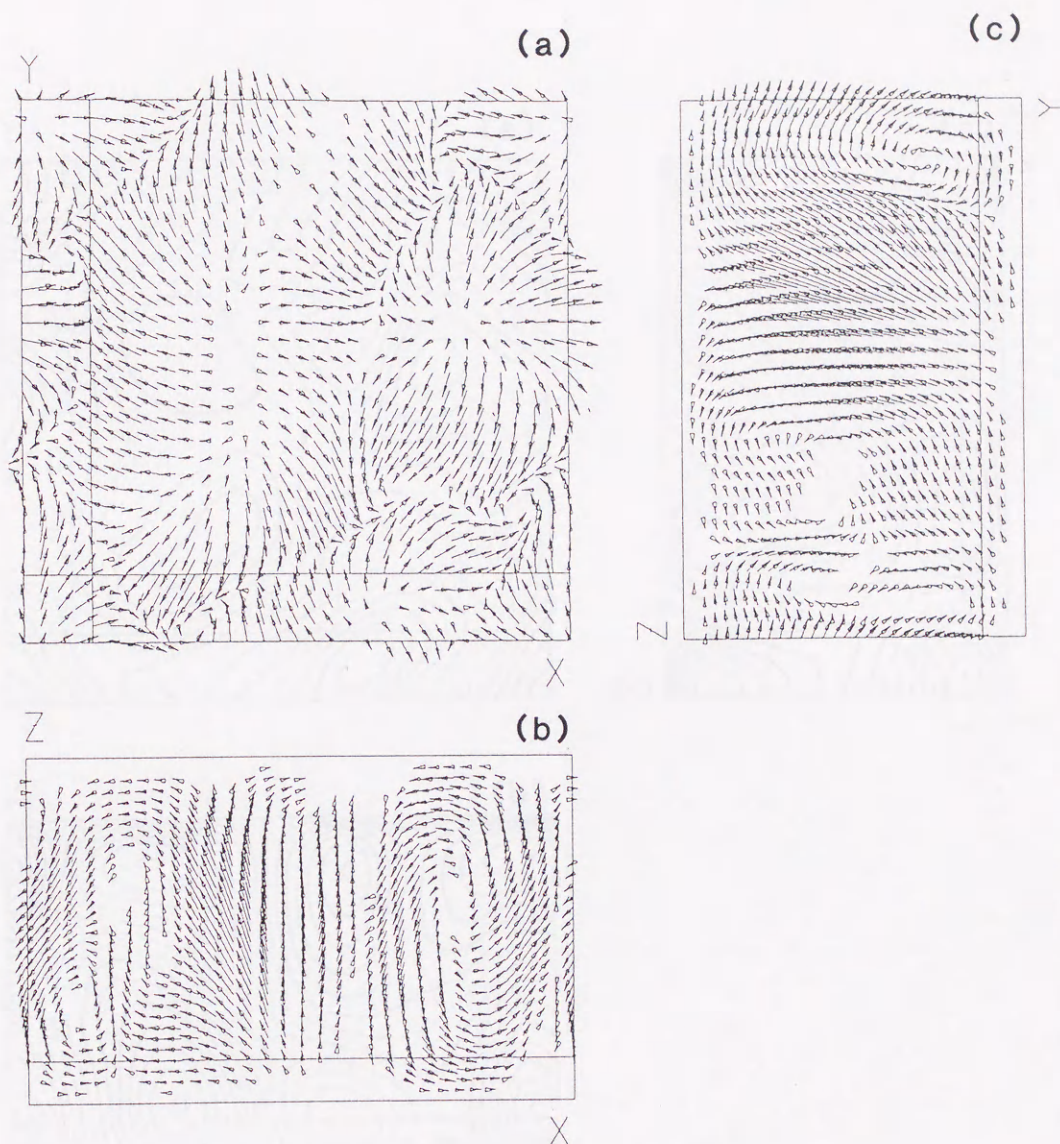


Figure 2.20 Velocity field for the rotating case ($T_a = 400$). Same conditions as in Fig. 2.19.

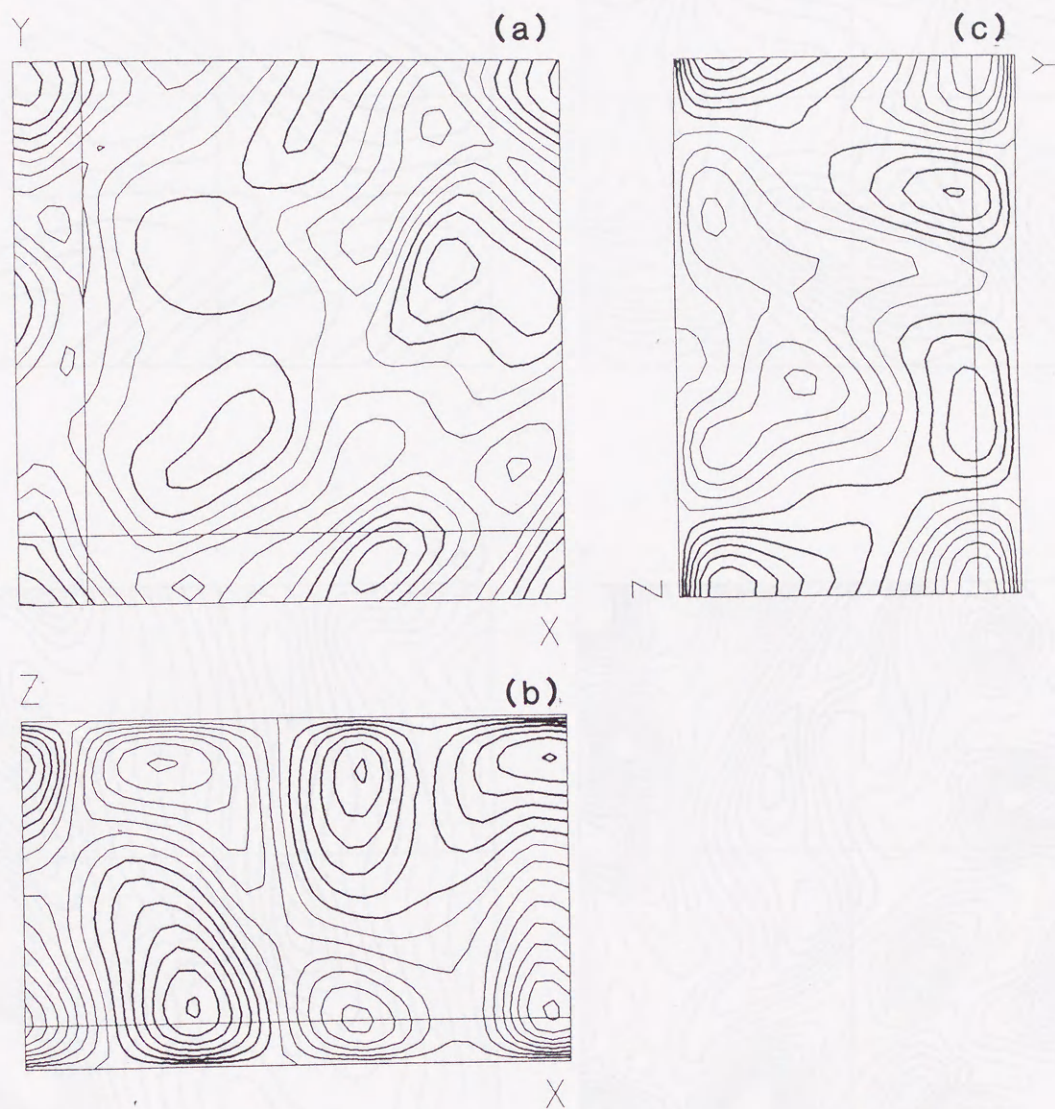


Figure 2.21 Contour maps of u_z (a), u_y (b) and u_x (c) for the rotating case. Same conditions as in Fig. 2.19.

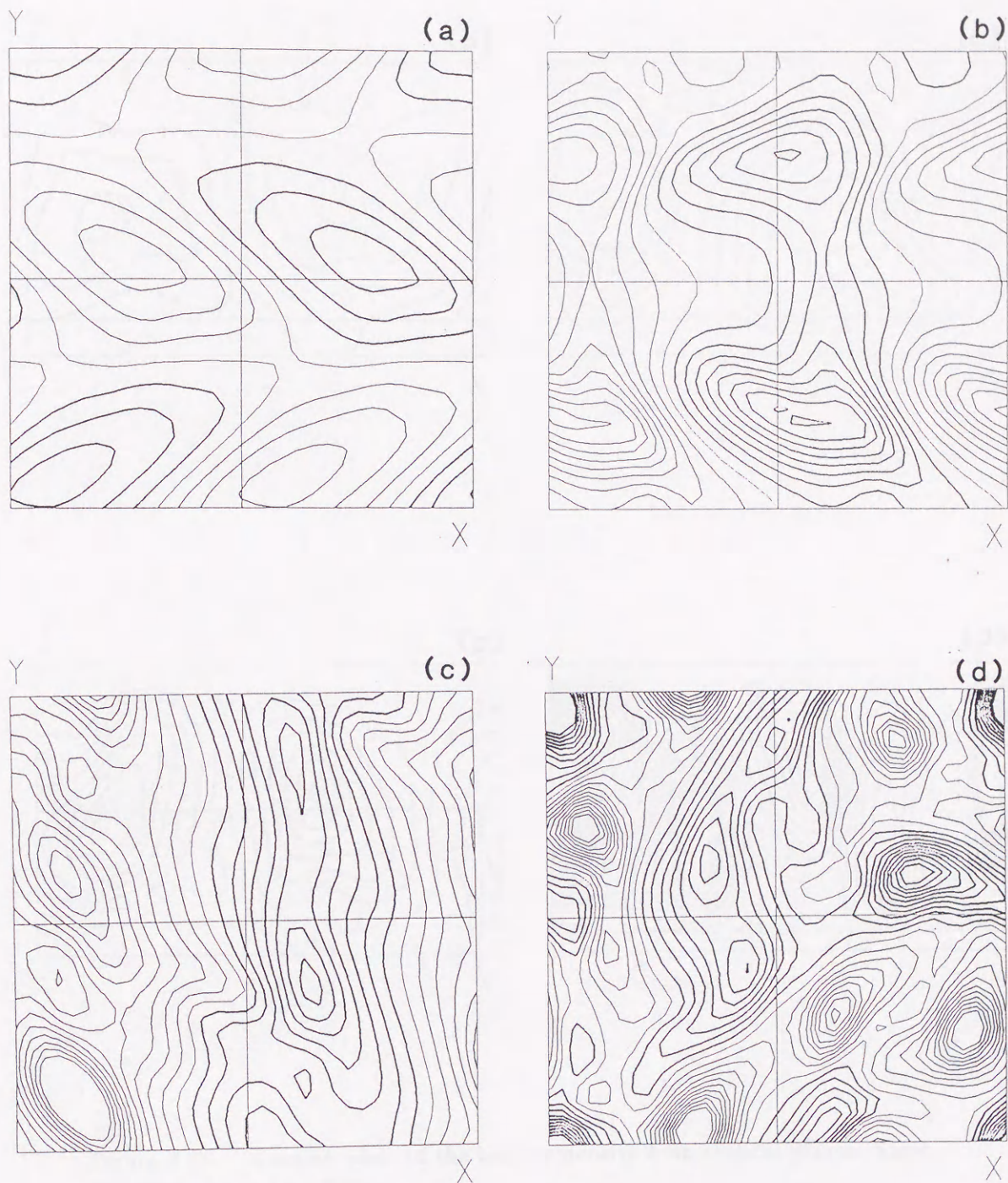


Figure 2.22 Contour plots of the helicity density h on the horizontal plane at $z = 0, t = 4$ for four cases, $T_a = 0$ (a), 25 (b), 100 (c) and 400 (d). The interval between the contour lines is 100.

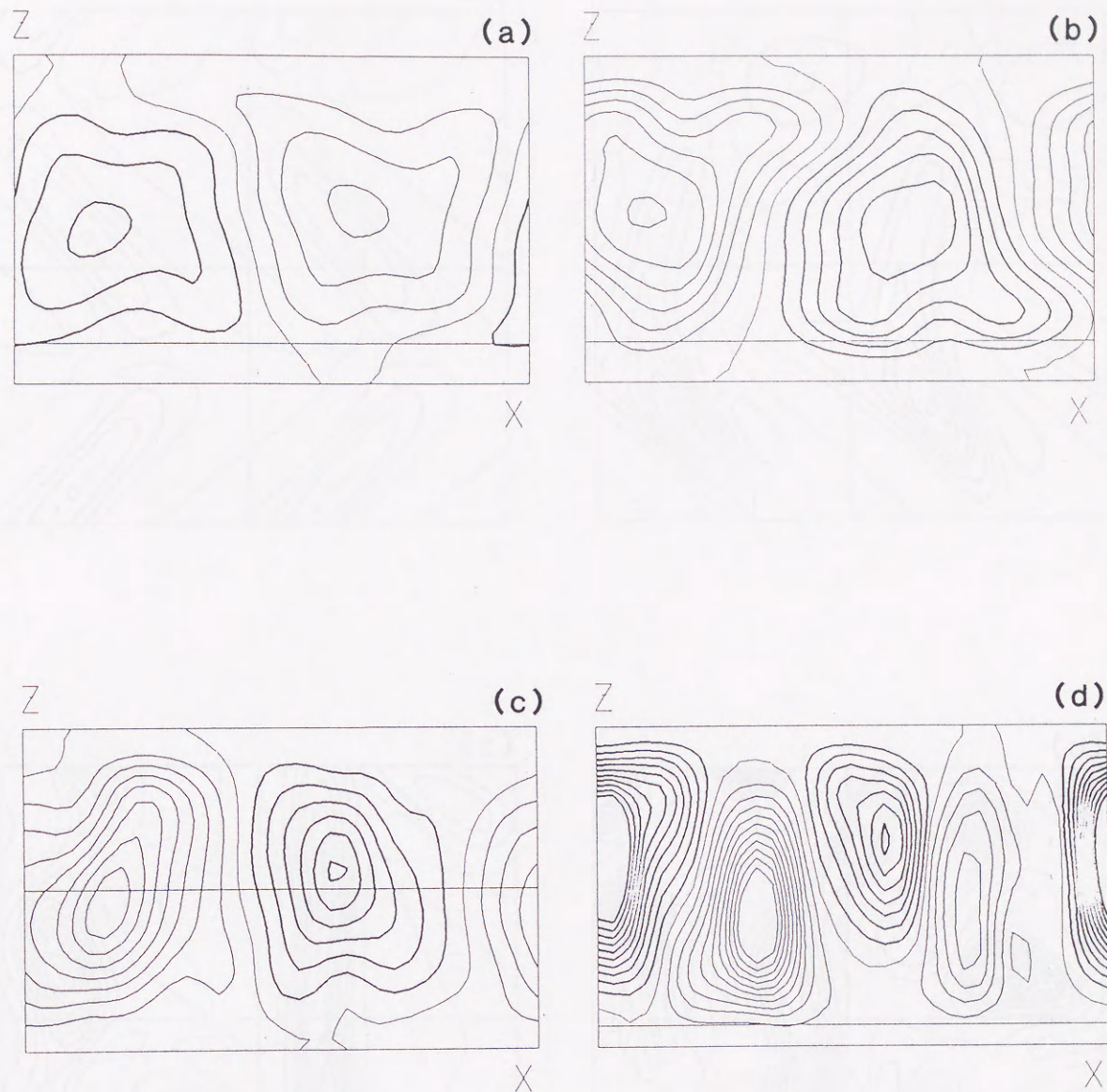


Figure 2.23 Contour plots of the helicity density h on vertical planes. Same conditions as in Fig. 2.22.

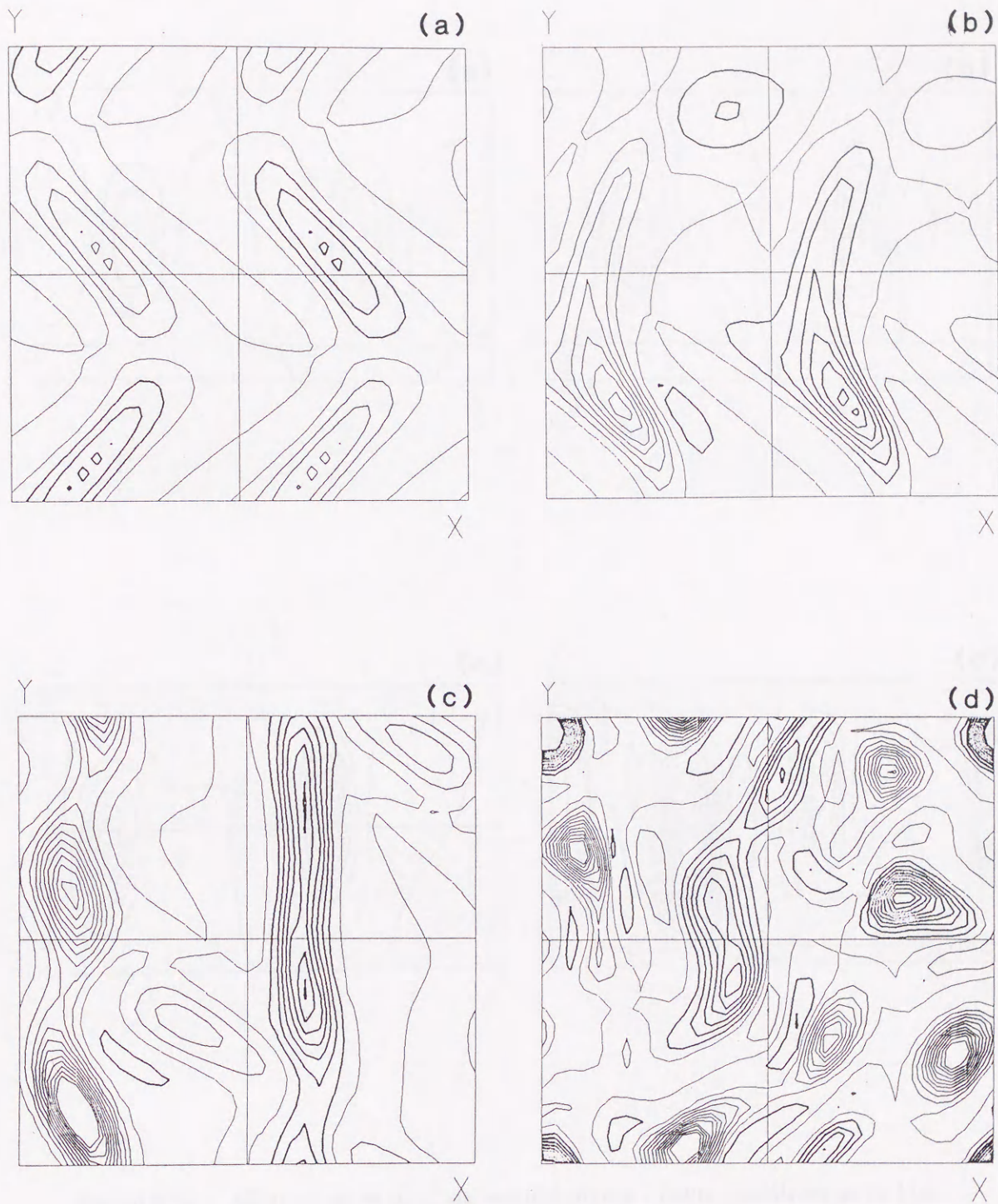


Figure 2.24 Contour maps of a part of helicity density h_z on the horizontal plane. Same conditions as in Fig. 2.22.

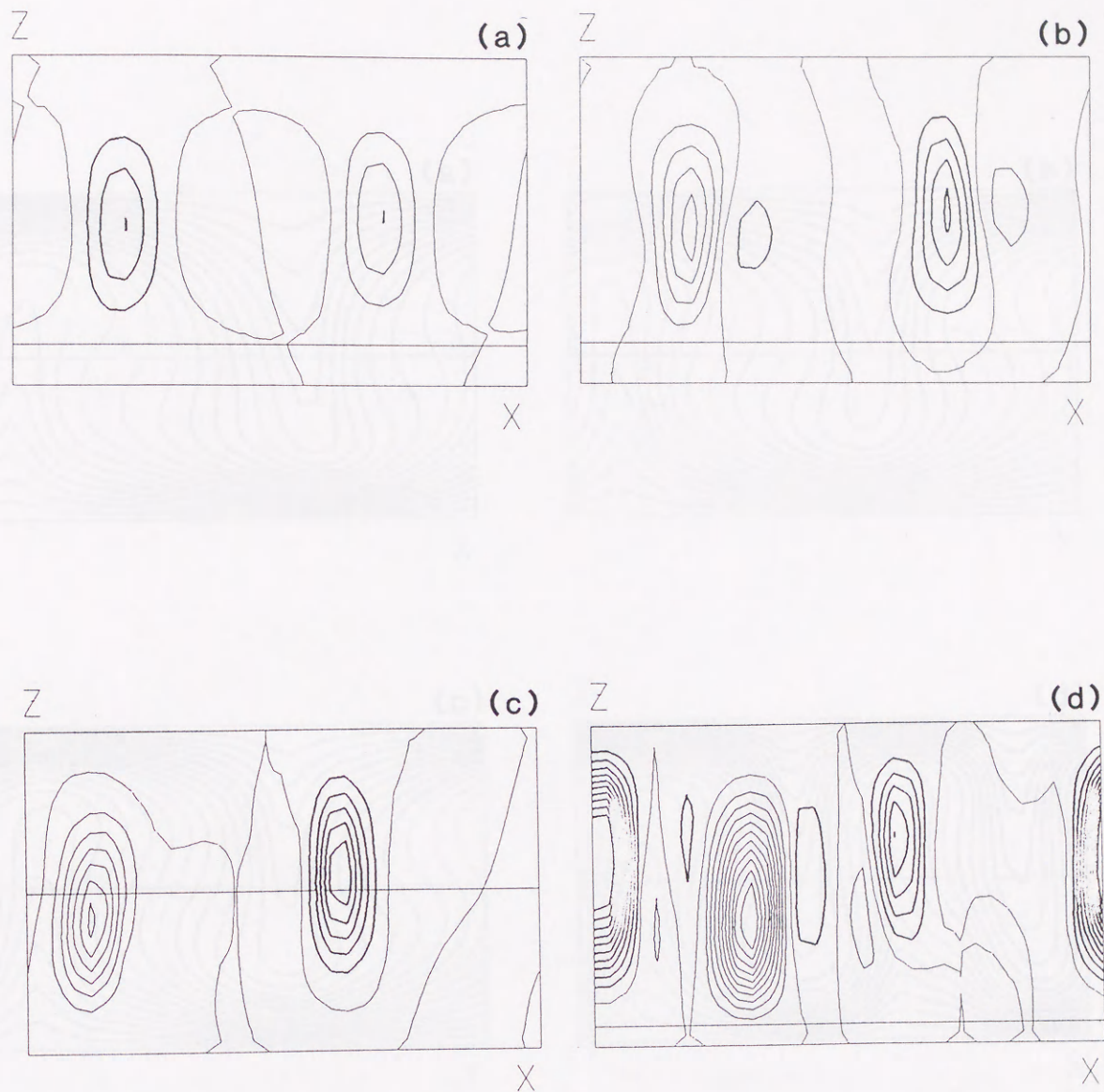


Figure 2.25 Contour plots of h_z on vertical planes . Same conditions as in Fig. 2.23.

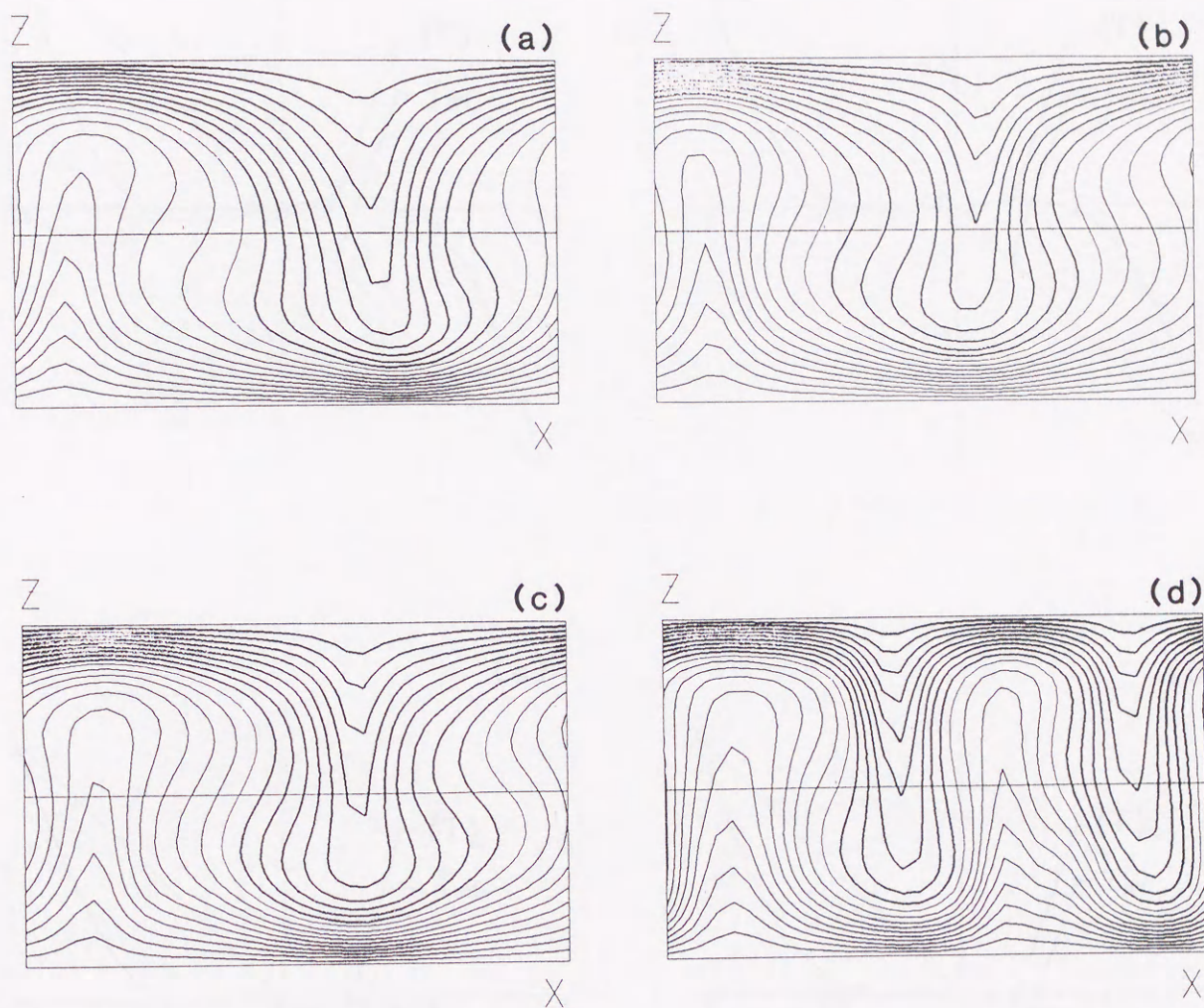


Figure 2.26 Contour plots of the temperature field T on the vertical plane at $y = \pi/2$ at $t = 4$ for $T_a = 0$ (a), 25 (b), 100 (c) and 400 (d).

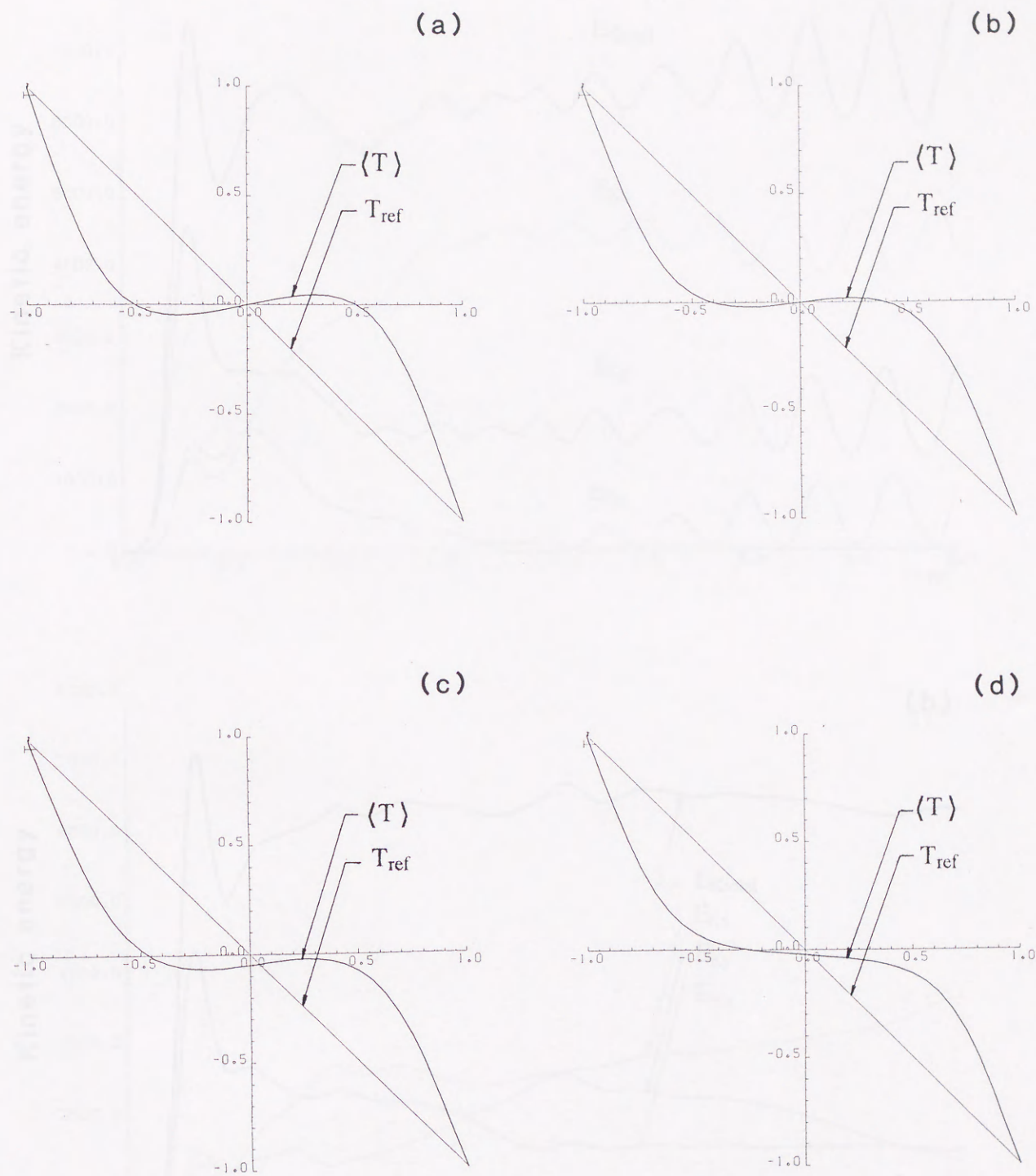


Figure 2.27 Horizontally averaged temperature field $\langle T(z) \rangle$ at $t = 4$ for $T_a = 0$ (a), 25 (b), 100 (c) and 400 (d). Thermal conduction profile $T_{ref} = -z$ is also presented.

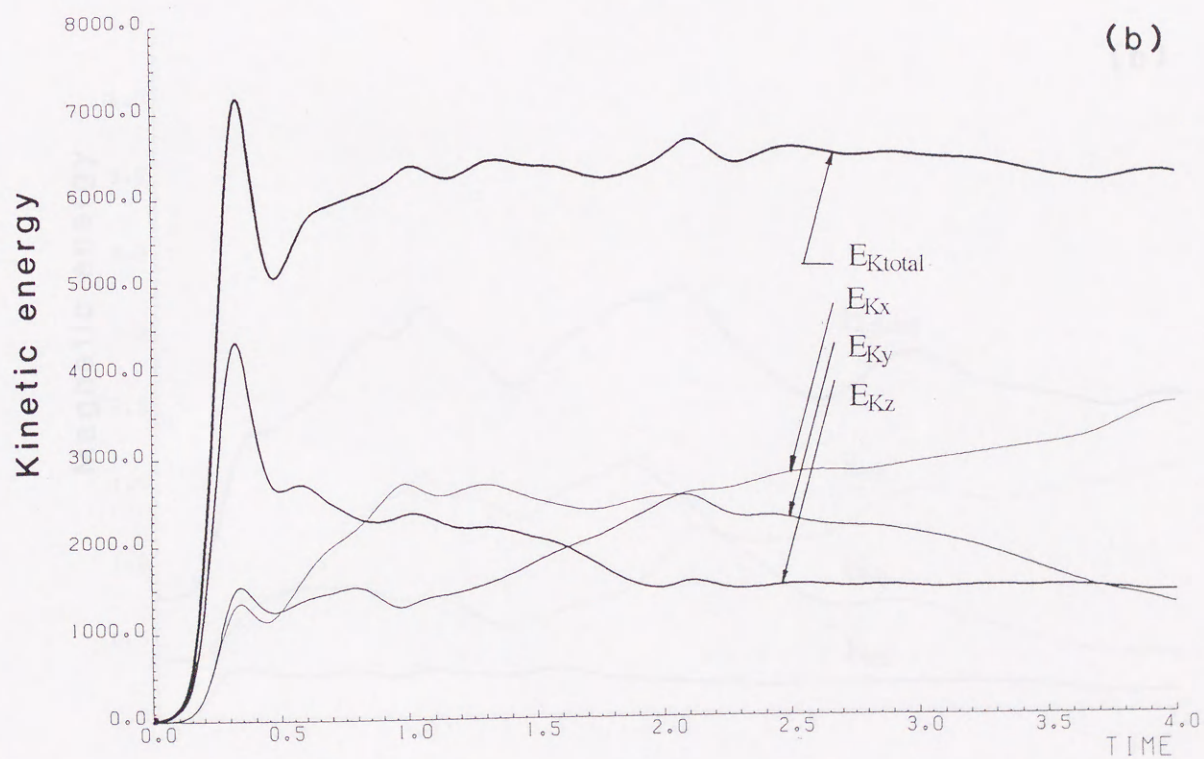
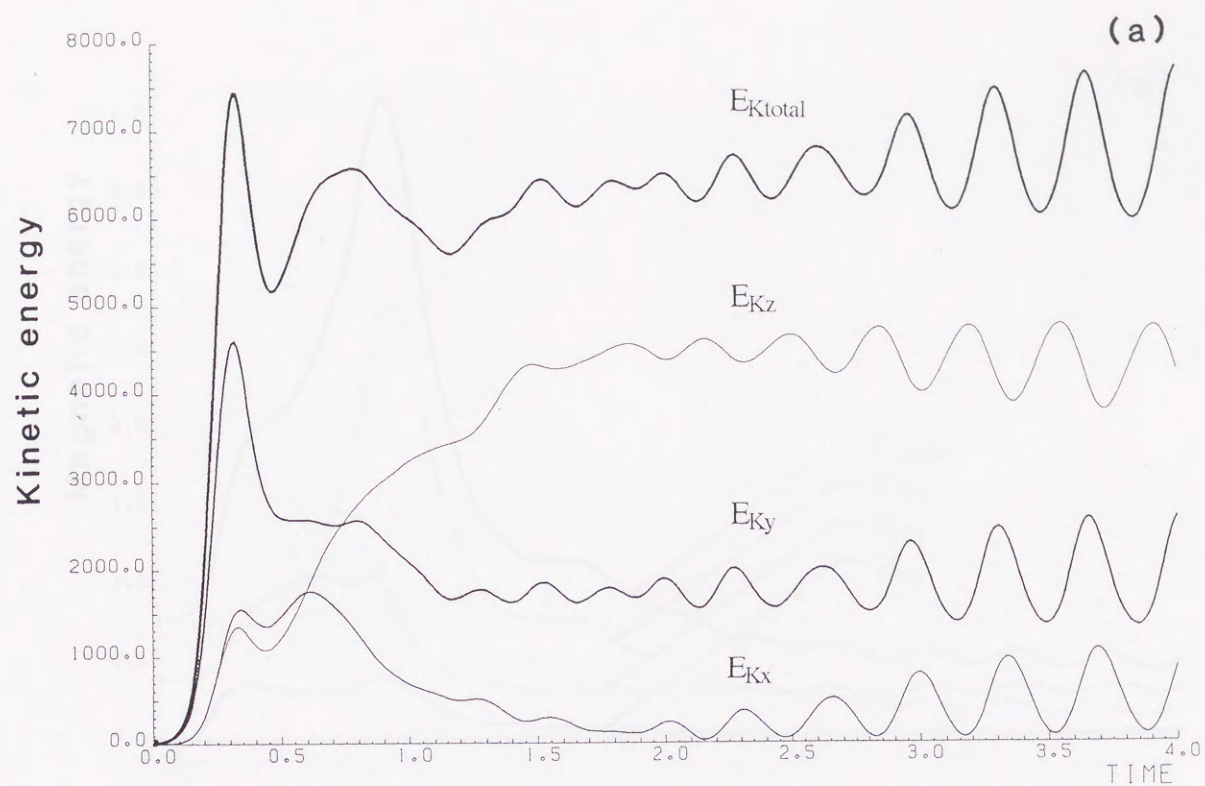


Figure 2.28 Time evolution of the kinetic energy for $T_a = 0$ (a) and 100 (b).

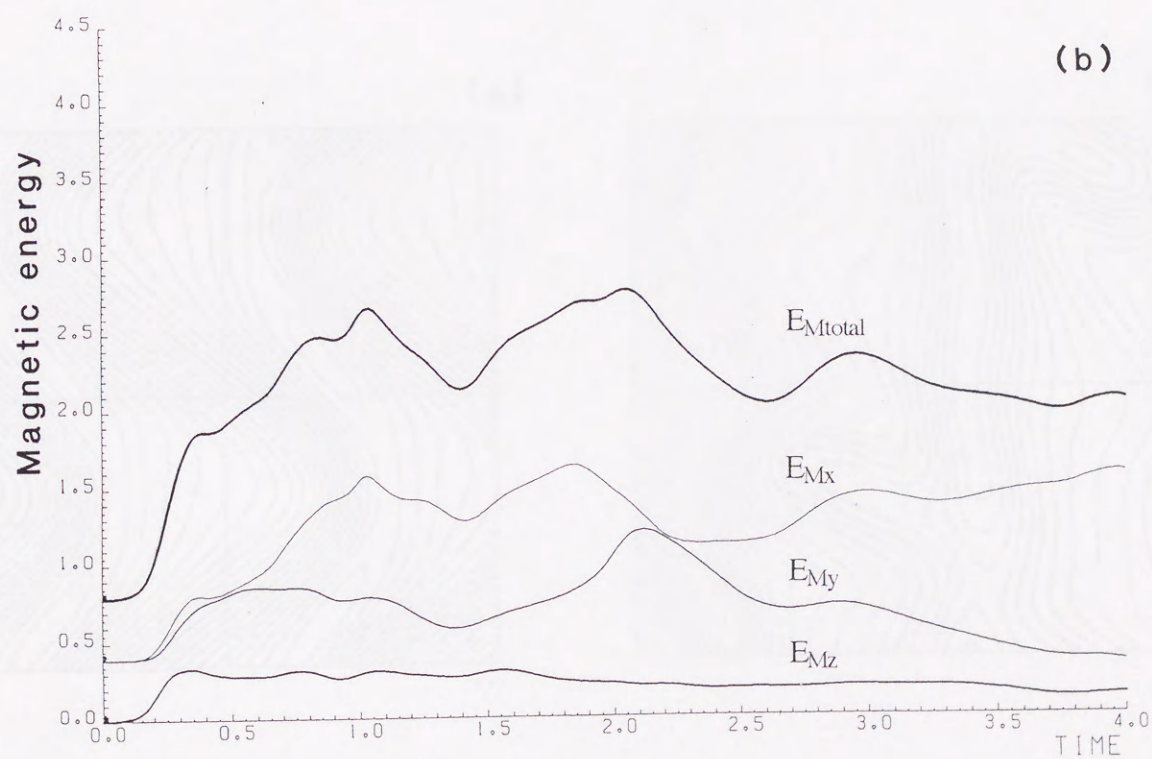
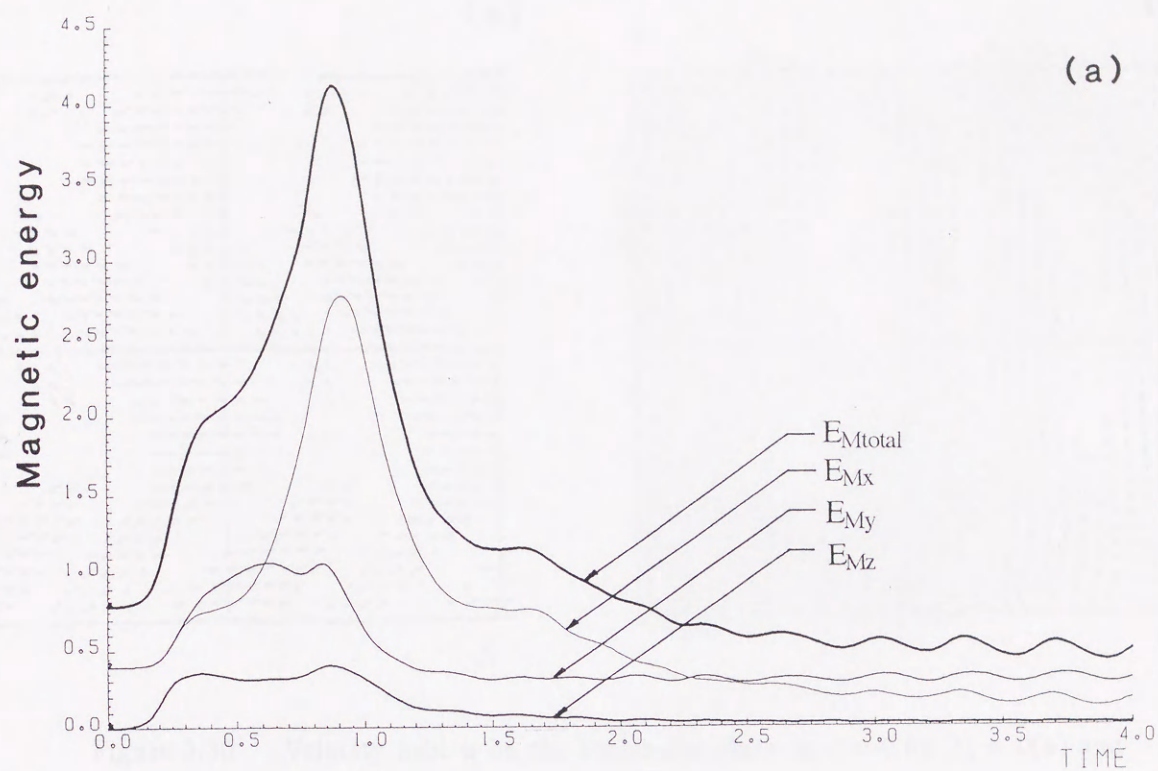


Figure 2.29 The magnetic energy as a function of time for $T_a = 0$ (a) and 100 (b).

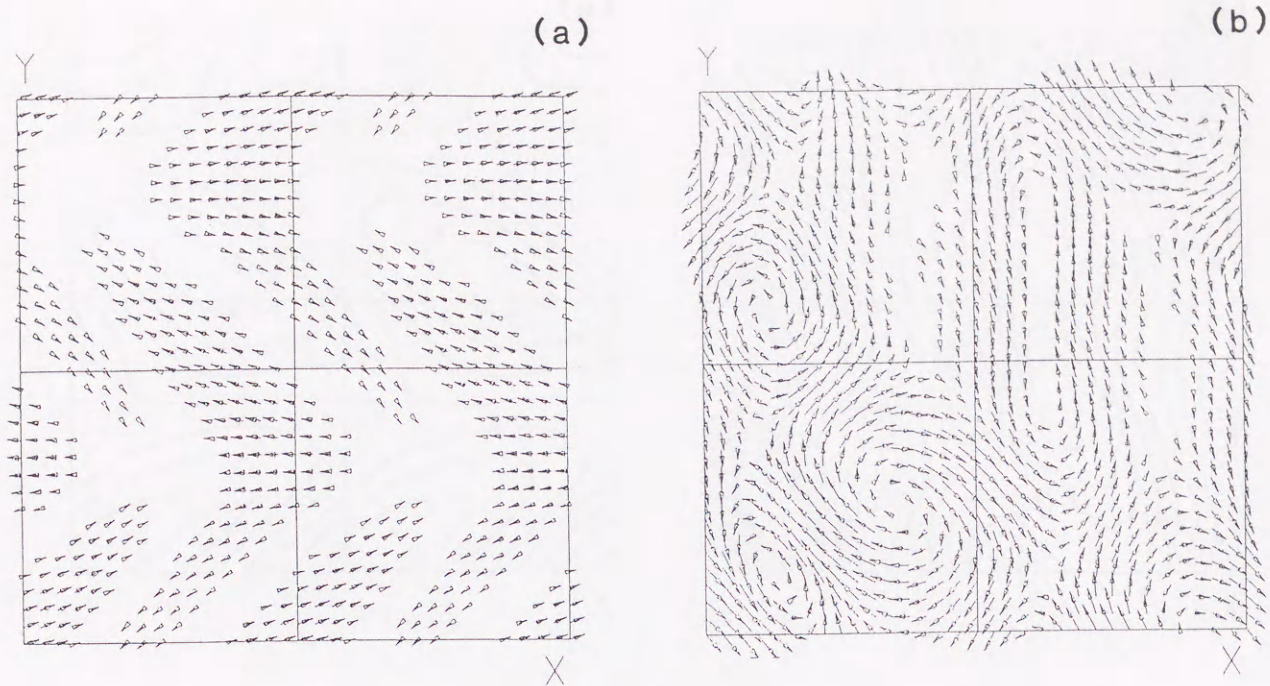


Figure 2.30 Velocity field u on the horizontal plane at $z = 0$ for $T_a = 0$ (a) and 100 (b).

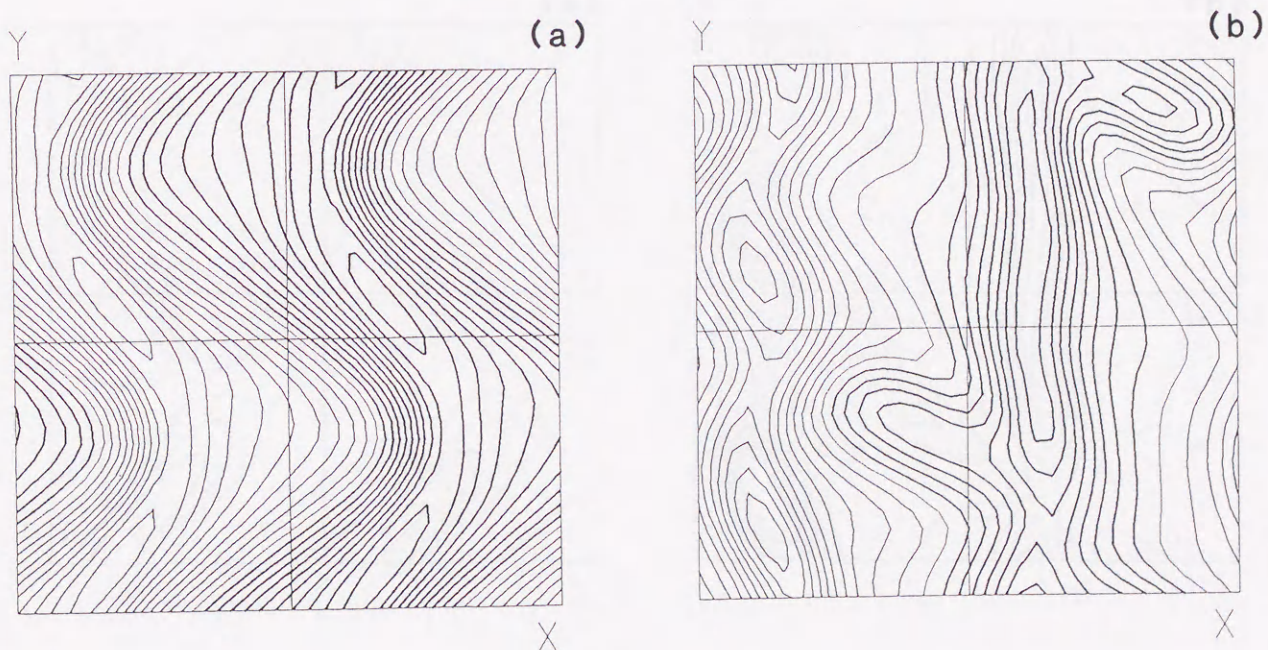


Figure 2.31 Contour plots of u_z on the horizontal plane at $z = 0$ at $t = 4$ for $T_a = 0$ (a) and 100 (b).

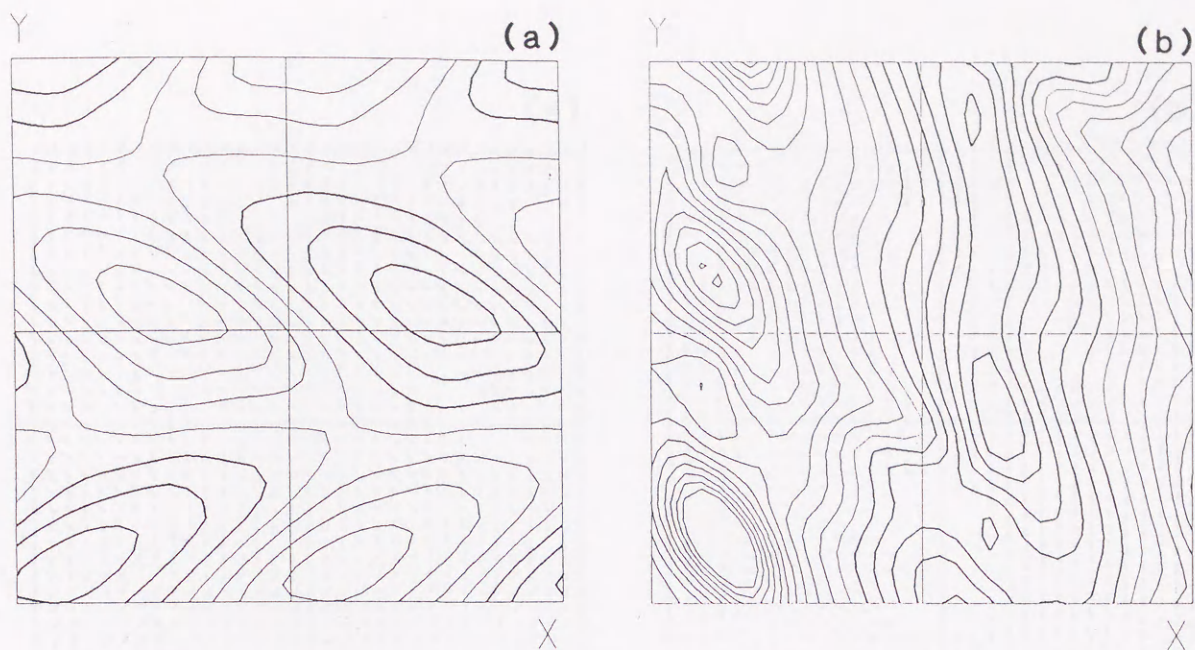


Figure 2.32 Contour plots of h on the horizontal plane at $z = 0$ at $t = 4$ for $T_a = 0$ (a) and 100 (b).

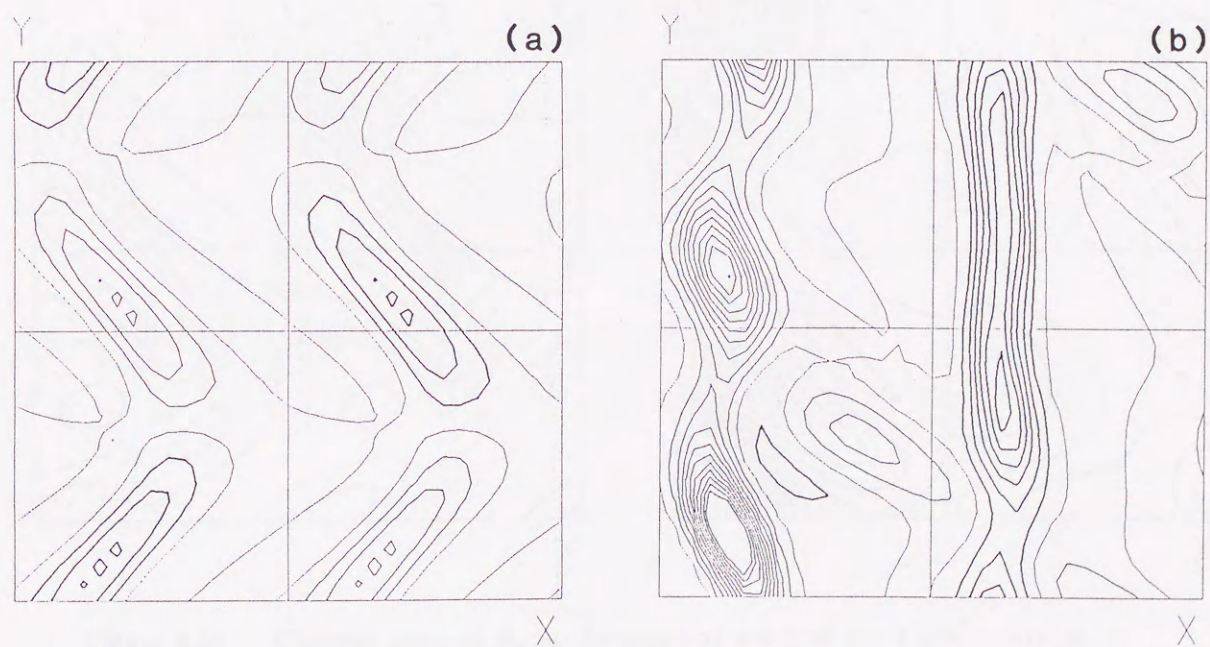


Figure 2.33 Contour maps of h_z . Same conditions as in Fig. 2.32.

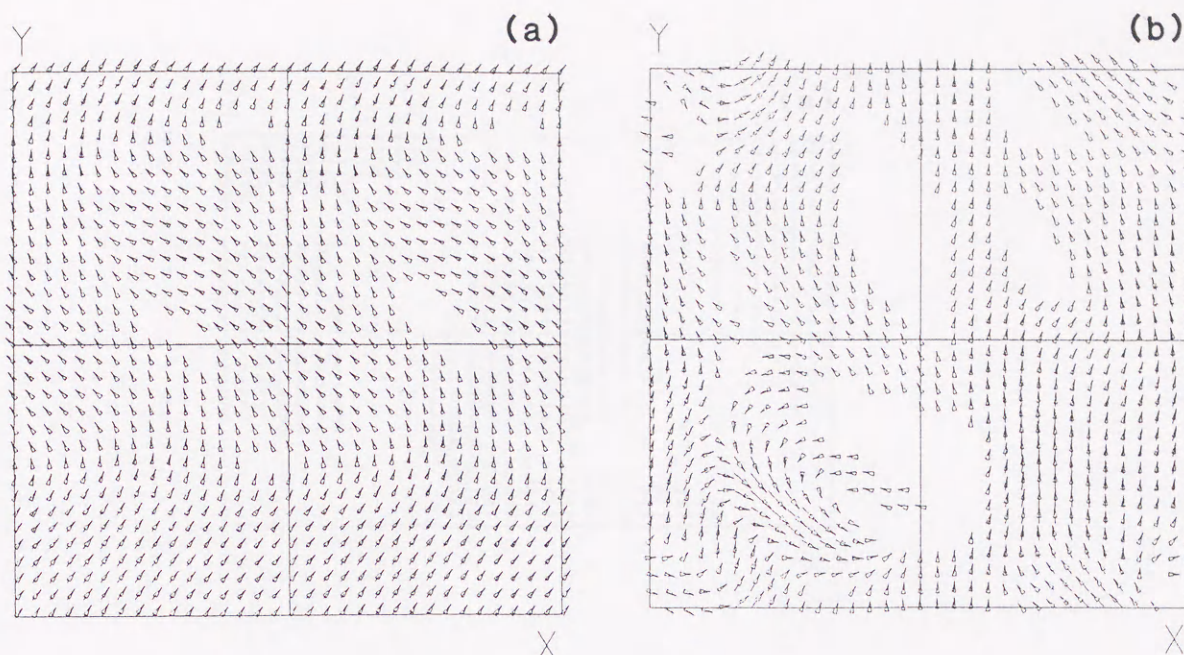


Figure 2.34 Magnetic field \mathbf{B} in the horizontal plane at $z = 0$ at $t = 4$ for the non-rotating (a) and rotating (b) cases.

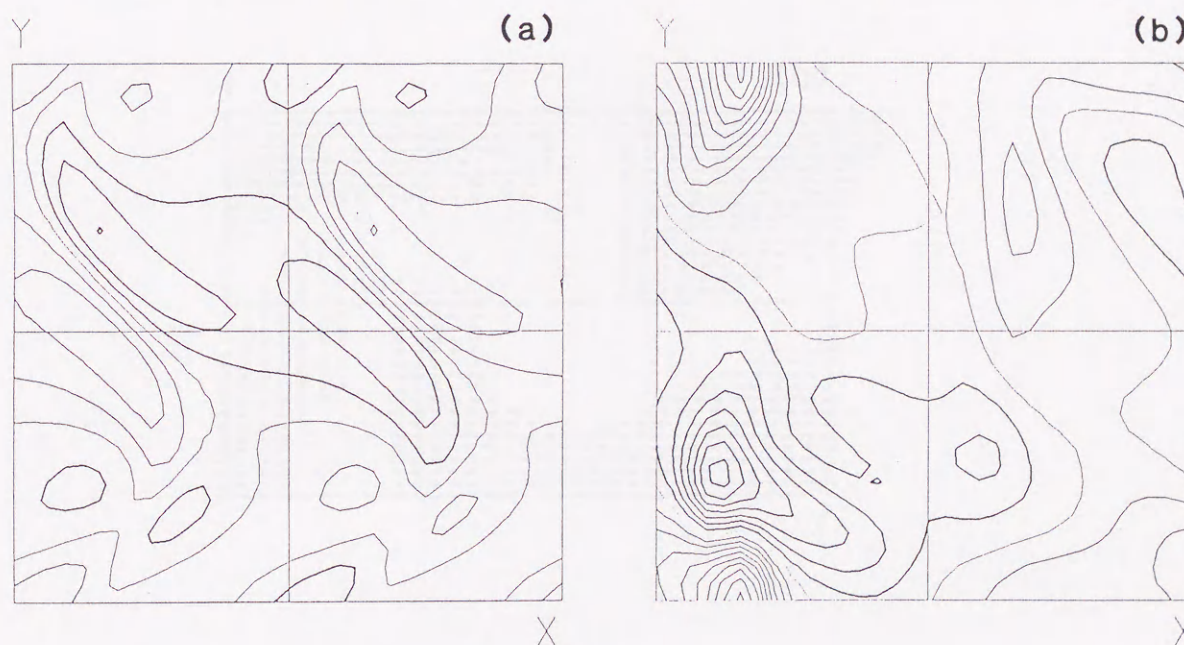


Figure 2.35 Contour plots of B_z in the plane at $z = 0$ at $t = 4$. The intervals between the contour are 0.02 for the non-rotating case (a) and 0.04 for the rotating case (b).

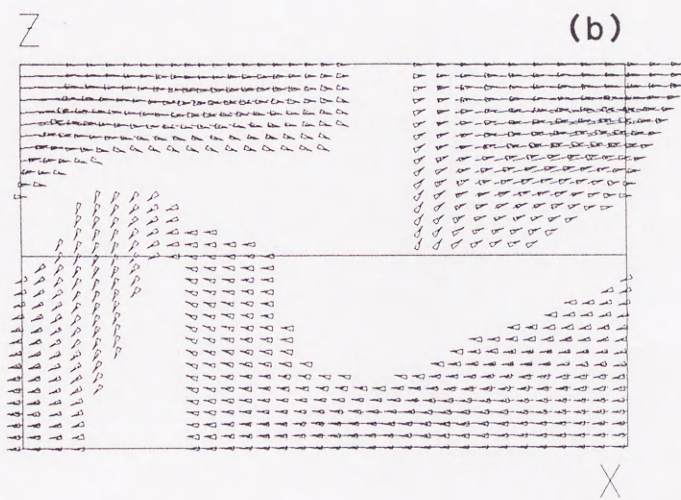
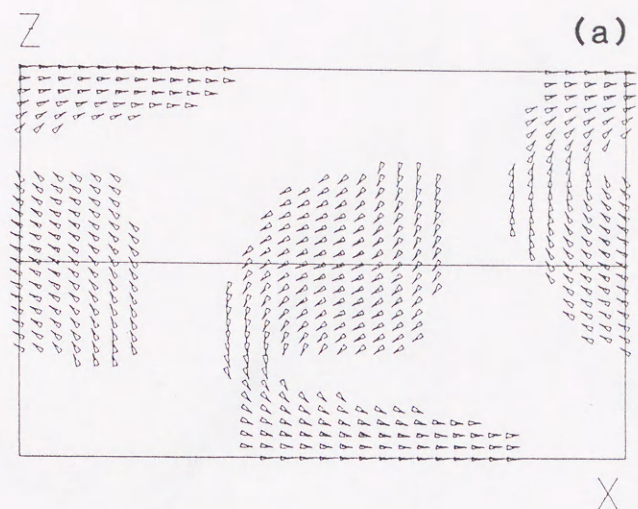


Figure 2.36 Magnetic field in the vertical plane at $y = \pi/2$ at $t = 4$ for the non-rotating (a) and rotating (b) cases.

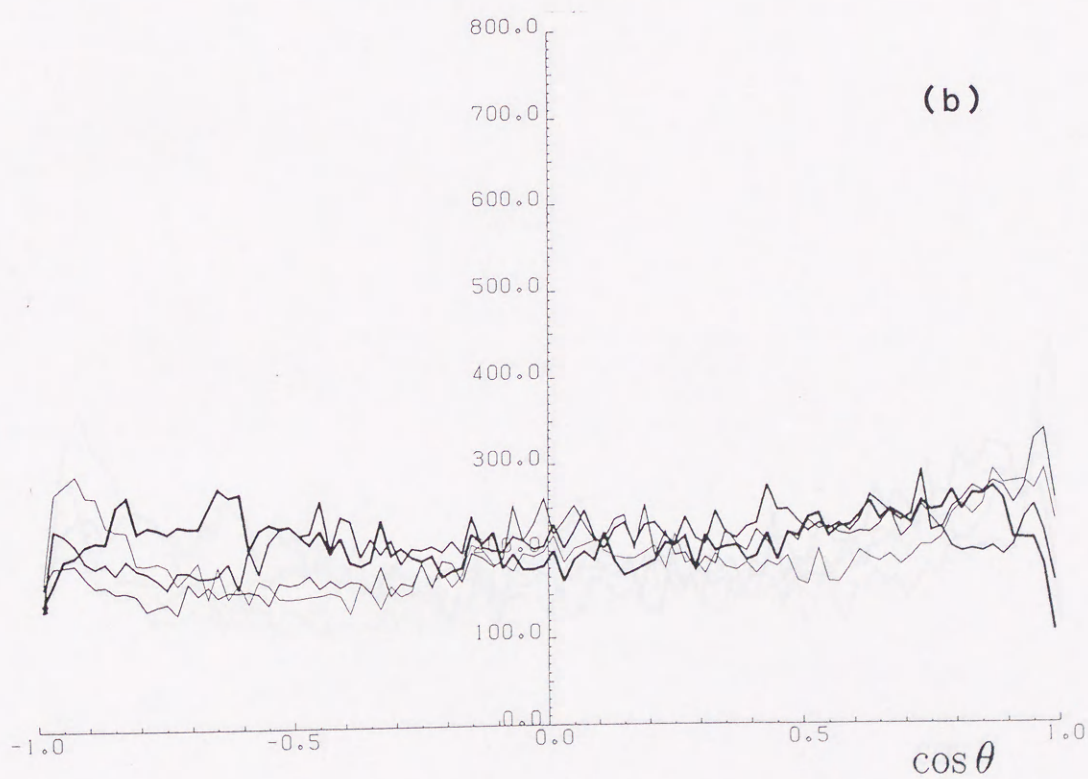
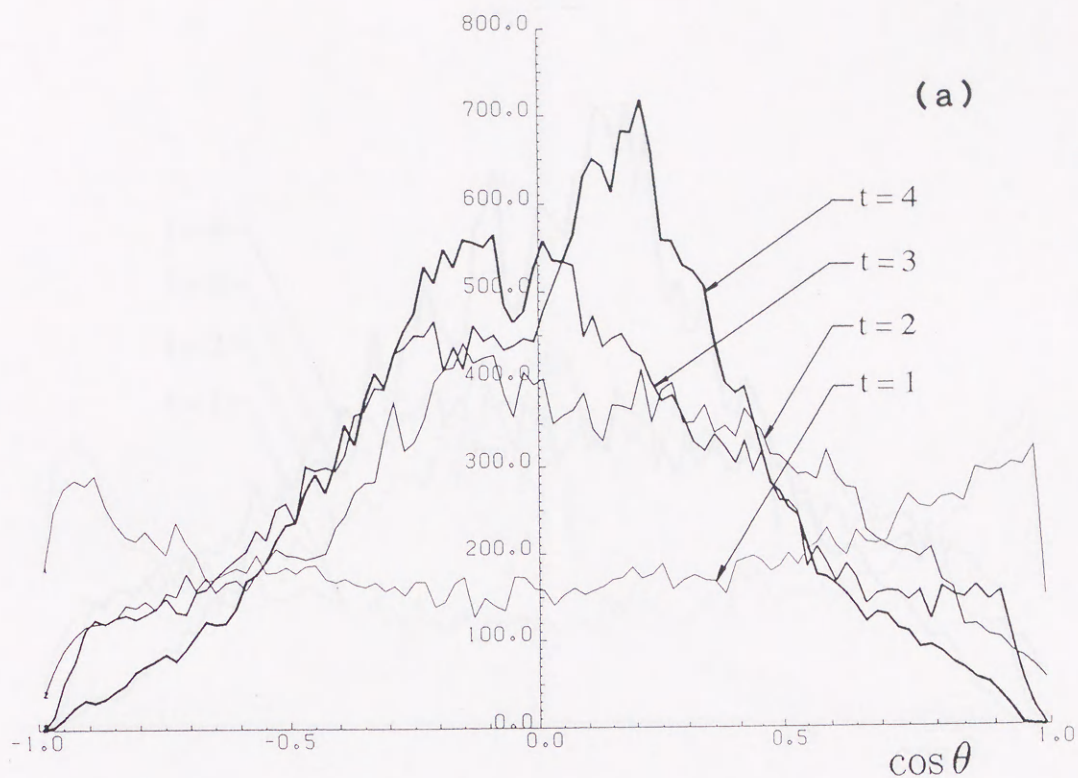


Figure 2.37 Geometrical relation between u and B . Histogram of $\cos \theta$ for four different times, i.e. $t = 1, 2, 3$ and 4 , where θ is an angle between u and B vectors at a spatial point for the non-rotating (a) and rotating (b) cases. All spatial points in the simulation box are analyzed.

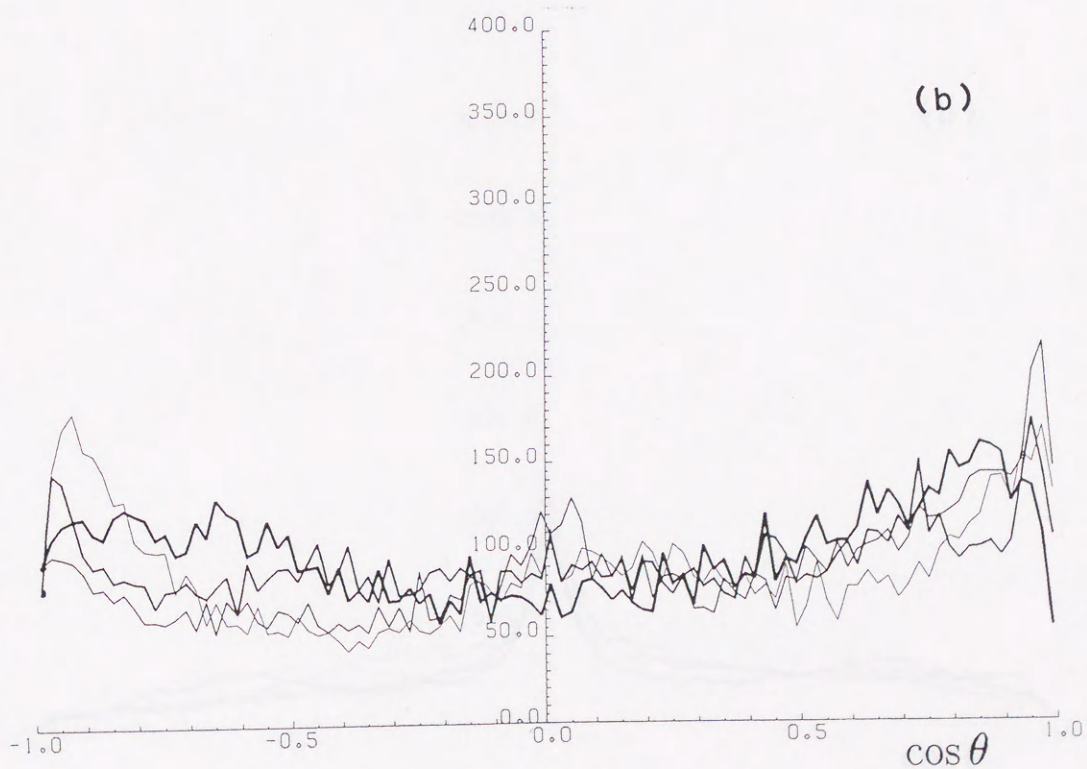
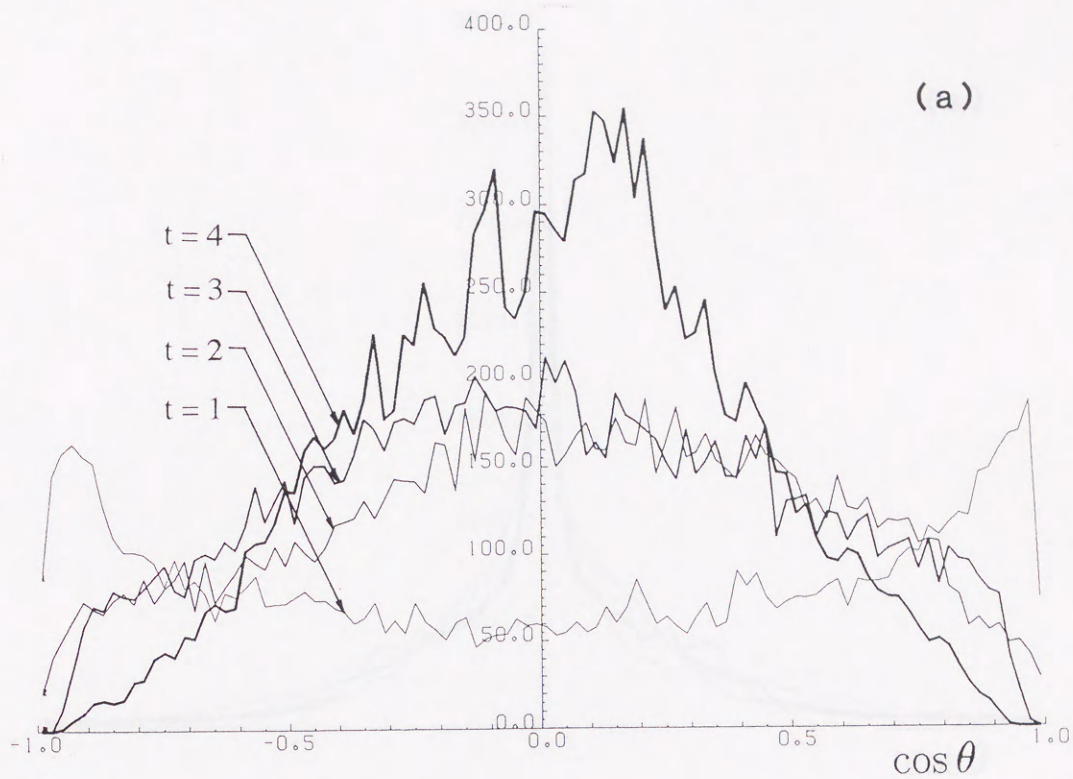


Figure 2.38 Geometrical relation between u and B . Histogram of $\cos \theta$. Same conditions as in Fig. 2.37. Only spatial points which satisfy the condition $|u| \geq u_{rms}$ are analyzed.

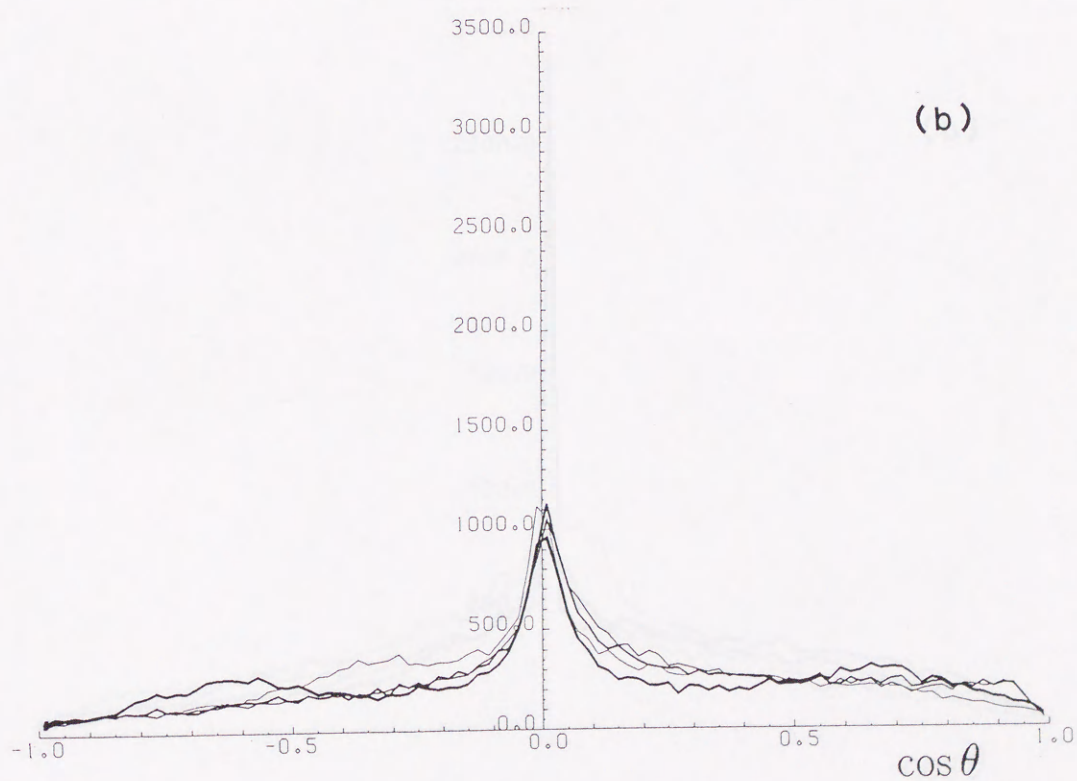
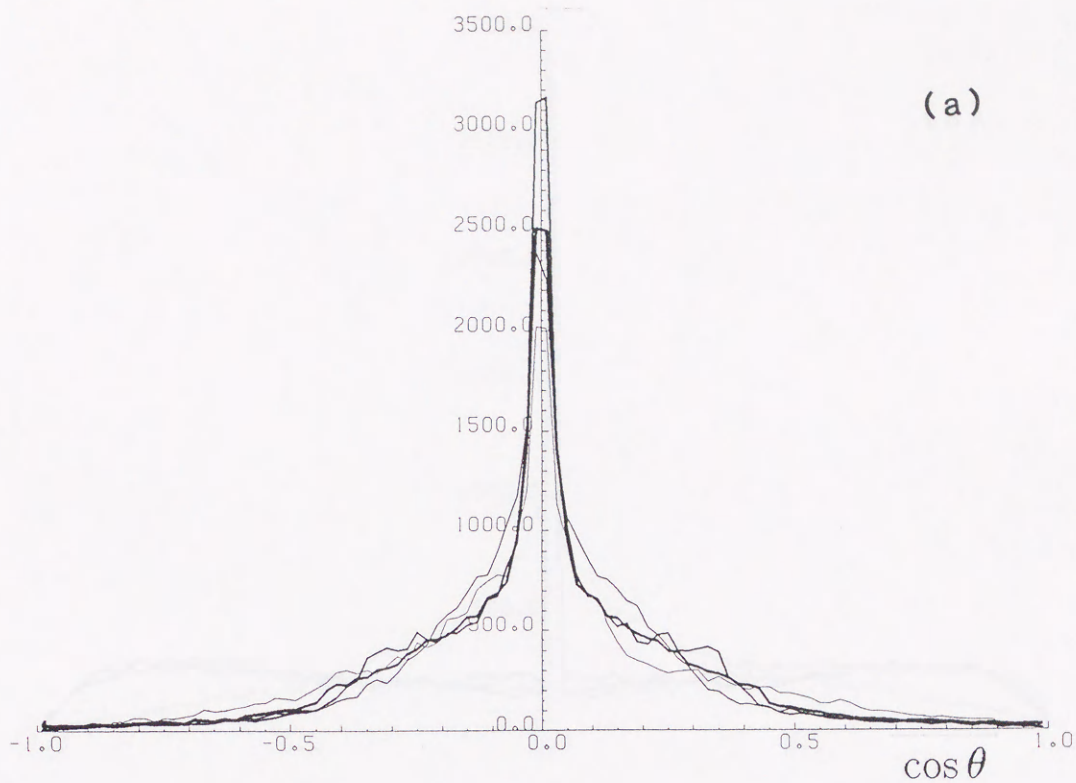


Figure 2.39 Geometrical relation between u and ω . Histogram of $\cos \theta$ where θ is an angle between u and ω vectors. Same conditions as in Fig. 2.37. All spatial points in the simulation box are analyzed.

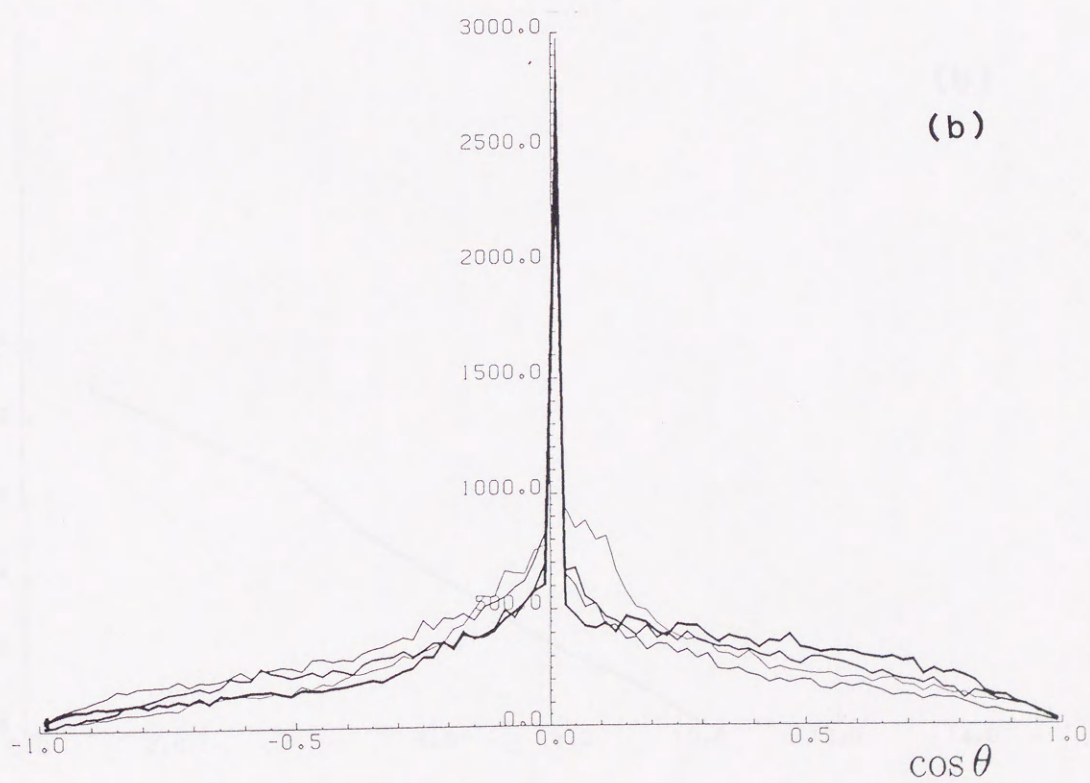
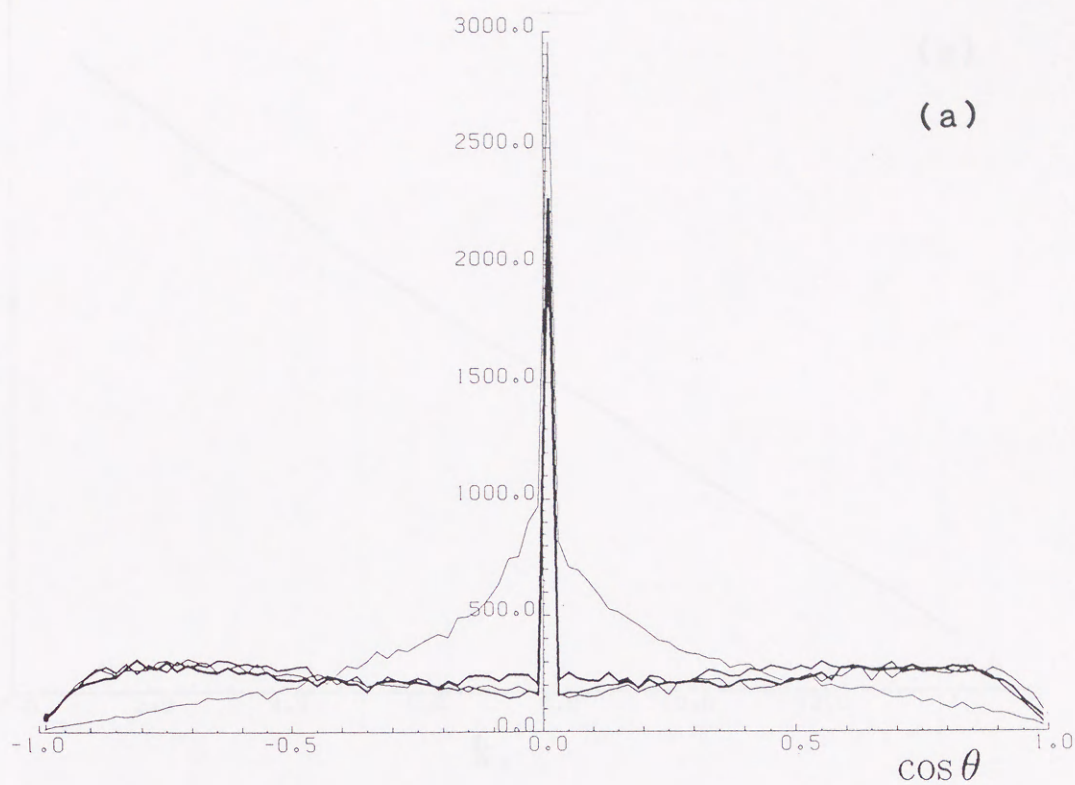


Figure 2.40 Geometrical relation between \mathbf{B} and \mathbf{J} . Histogram of $\cos \theta$ where θ is an angle between \mathbf{B} and \mathbf{J} vectors. Same conditions as in Fig. 2.37. All spatial points in the simulation box are analyzed.

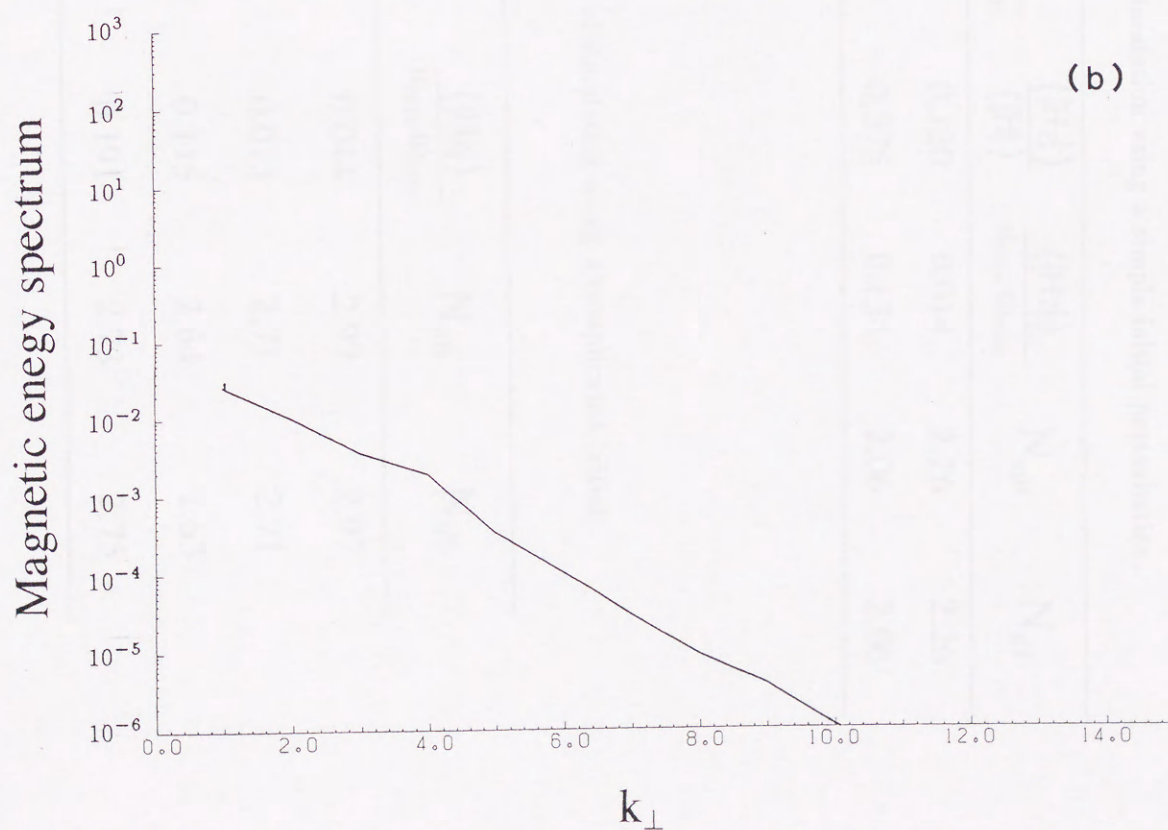
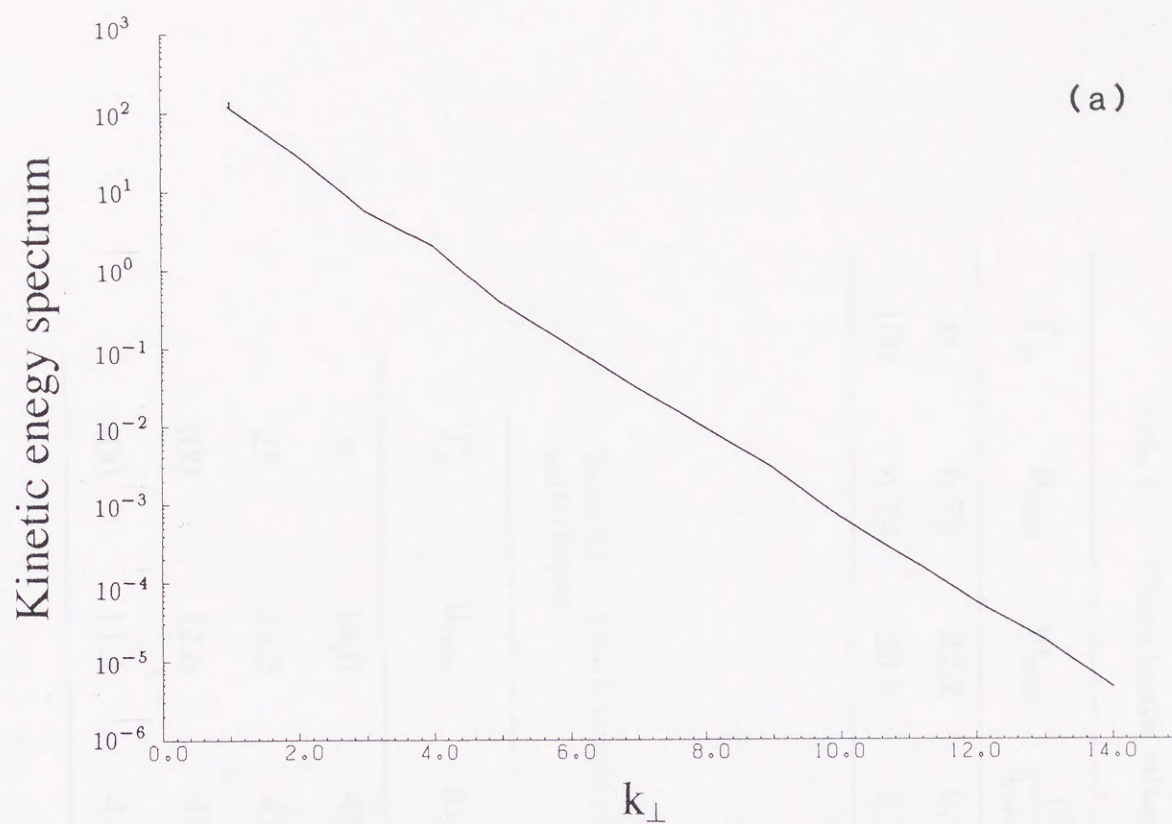


Figure 2.41 Kinetic (a) and magnetic (b) energy spectrum as a function of the horizontal wavenumber k_{\perp} for $T_a = 100$ at $t = 4$.

Table 2.1 Characteristic values of simulation using a simple initial perturbation.

T_a	u_{rms}	ω_{rms}	$\frac{\langle H \rangle}{u_{rms} \omega_{rms}}$	$\frac{\langle Hz \rangle}{\langle H \rangle}$	$\frac{\langle Hz \rangle}{u_{rms} \omega_{rms}}$	N_{uB}	N_{uT}
0	6.72	22.2	0.119	0.120	0.014	2.26	2.26
100	6.29	20.4	0.357	0.375	0.134	2.06	2.06

Table 2.2 Characteristic values of simulation using a complicated initial perturbation.

T_a	u_{rms}	ω_{rms}	$\frac{\langle Hz \rangle}{u_{rms} \omega_{rms}}$	N_{uB}	N_{uT}
0	14.0	45.6	0.044	2.97	2.97
25	13.2	41.5	0.073	2.71	2.71
100	12.6	40.1	0.115	2.64	2.63
400	11.1	41.5	0.191	2.73	2.75

3. Magnetoconvection in a spherical shell

3.1. Toroidal and Poloidal fields

In this section we investigate a spherical shell model for the study of magnetoconvection. The velocity vector \mathbf{u} is assumed to be purely poloidal, i.e. it has no azimuthal component. The magnetic field \mathbf{B} is assumed to be purely toroidal, i.e. it has only an azimuthal component. This is a reasonable approximation for the Earth's core, where the magnetic field is predominantly toroidal and the velocity field is predominantly poloidal. The ratio of the toroidal to the poloidal component of the magnetic field is of the order of unity, while the ratio of the toroidal to the poloidal component of the velocity field is of the order of 10^{-1} .

3. Magnetoconvection in a spherical shell

The angle formed by the gravity and angular velocity vectors gradually changes with latitude in contrast with the plane boundary model. The convection is assumed to be purely poloidal, i.e. it has no azimuthal component. The magnetic field \mathbf{B} is assumed to be purely toroidal, i.e. it has only an azimuthal component. This is a reasonable approximation for the Earth's core, where the magnetic field is predominantly toroidal and the velocity field is predominantly poloidal. The ratio of the toroidal to the poloidal component of the magnetic field is of the order of unity, while the ratio of the toroidal to the poloidal component of the velocity field is of the order of 10^{-1} .

It is well established that the magnetic field in the Earth's core is predominantly toroidal. This is in contrast with the plane boundary model, where the magnetic field is assumed to be purely poloidal. The convection is assumed to be purely poloidal, i.e. it has no azimuthal component. The magnetic field \mathbf{B} is assumed to be purely toroidal, i.e. it has only an azimuthal component. This is a reasonable approximation for the Earth's core, where the magnetic field is predominantly toroidal and the velocity field is predominantly poloidal. The ratio of the toroidal to the poloidal component of the magnetic field is of the order of unity, while the ratio of the toroidal to the poloidal component of the velocity field is of the order of 10^{-1} .

3 Magnetoconvection in a spherical shell

3.1 Toroidal and Poloidal fields

In this section we investigate a spherical shell model for the study of magnetoconvection relating to the generation process of the celestial magnetic field. The various conditions of the spherical model are, therefore, adjusted to simulate magnetoconvection of the Earth's outer core though some non-dimensional parameters are quite different from those in the Earth's outer core. The ratio of the inner radius of the shell to the outer one is set at 0.4 in the present model, meanwhile this ratio of the Earth's outer core is about 0.35. The gravity g is assumed to be in direct proportional to r . In the spherical shell model the angle formed by the gravity and angular velocity vectors gradually changes with latitude in contrast with the plane boundary model. The conducting fluid is adjoining an insulator at the outer boundary corresponding the core-mantle boundary and adjoining the conducting solid at inner boundary corresponding to the inner core boundary.

It is well established that any solenoidal vector field can be separated into toroidal and poloidal vector fields (Bullard and Gellman, 1954 ; Bacus, 1958 ; Chandrasekhar , 1961). Since we adopt the Boussinesq approximation, in the present study, divergence of \mathbf{u} is zero. In addition, divergence of \mathbf{B} is naturally zero from Maxwell equation. Therefore, \mathbf{u} and \mathbf{B} can be expressed as a sum of toroidal and poloidal fields. By introducing toroidal and poloidal fields, the interaction between \mathbf{u} and \mathbf{B} is shown in a simple way. In addition, the boundary condition of \mathbf{B} , which requires that \mathbf{B} in a shell is connected to a potential field at the outer boundary, is easily satisfied using the toroidal-poloidal decomposition.

A solenoidal vector field, such as the magnetic field \mathbf{B} consists of the toroidal \mathbf{T} and poloidal \mathbf{S} vector components, as

$$\mathbf{B} = \mathbf{T} + \mathbf{S}, \quad (3.1)$$

where

$$\mathbf{T} = \nabla \times \left(\Psi \frac{\mathbf{r}}{r} \right), \quad (3.2)$$

and

$$\mathbf{S} = \nabla \times \nabla \times \left(\Phi \frac{\mathbf{r}}{r} \right), \quad (3.3)$$

for toroidal scalar function Ψ and poloidal scalar function Φ . In spherical coordinate system (r, θ, ϕ) (Fig. 3.1), the components of \mathbf{T} and \mathbf{S} are given by

$$T_r = 0, \quad T_\theta = \frac{1}{r \sin \theta} \frac{\partial \Psi}{\partial \phi}, \quad T_\phi = -\frac{1}{r} \frac{\partial \Psi}{\partial \theta}, \quad (3.4)$$

$$S_r = \frac{1}{r^2} L^2 \Phi, \quad S_\theta = \frac{1}{r} \frac{\partial^2 \Phi}{\partial r \partial \theta}, \quad S_\phi = \frac{1}{r \sin \theta} \frac{\partial^2 \Phi}{\partial r \partial \phi}. \quad (3.5)$$

where L^2 represents the square of the angular momentum operator of quantum mechanics, given by,

$$L^2 = - \left\{ \frac{1}{\sin \theta} \frac{\partial}{\partial \theta} \left(\sin \theta \frac{\partial}{\partial \theta} \right) + \frac{1}{\sin^2 \theta} \frac{\partial^2}{\partial \phi^2} \right\}. \quad (3.6)$$

The operator L^2 generates the relation,

$$L^2 Y_l^m(\theta, \phi) = l(l+1) Y_l^m(\theta, \phi) \quad (3.7)$$

where $Y_l^m(\theta, \phi)$ is the spherical harmonic function defined by

$$Y_l^m(\theta, \phi) = P_l^m(\cos \theta) \exp^{im\phi} \quad (3.8)$$

and $P_l^m(\cos \theta)$ is the associated Legendre function of degree l and order m .

We expand Ψ and Φ in spherical harmonics as in Bullard and Gellman (1954), that is,

$$\Psi(r, \theta, \phi) = \sum_{l=1}^{\infty} \sum_{m=-l}^l T_l^m(r) Y_l^m(\theta, \phi) \quad (3.9)$$

$$\Phi(r, \theta, \phi) = \sum_{l=1}^{\infty} \sum_{m=-l}^l S_l^m(r) Y_l^m(\theta, \phi) \quad (3.10)$$

where $T_l^m(r)$ and $S_l^m(r)$ are the coefficients in spherical harmonic expansion of Ψ and Φ , respectively. Therefore, the spherical harmonic decompositions of the components of toroidal and poloidal fields result in

$$T_{rl}^m = 0, \quad T_{\theta l}^m = \frac{T_l^m(r)}{r \sin \theta} \frac{\partial Y_l^m(\theta, \phi)}{\partial \phi}, \quad T_{\phi l}^m = -\frac{T_l^m(r)}{r} \frac{\partial Y_l^m(\theta, \phi)}{\partial \theta} \quad (3.11)$$

$$S_{rl}^m = \frac{l(l+1)}{r^2} S_l^m(r) Y_l^m(\theta, \phi), \quad S_{\theta l}^m = \frac{1}{r} \frac{dS_l^m(r)}{dr} \frac{\partial Y_l^m(\theta, \phi)}{\partial \theta},$$

$$S_{\phi l}^m = \frac{1}{r \sin \theta} \frac{dS_l^m(r)}{dr} \frac{\partial Y_l^m(\theta, \phi)}{\partial \phi}. \quad (3.12)$$

Hence, the components of the magnetic field is expressed as

$$B_r = \sum_{l=1}^{\infty} \sum_{m=-l}^l \left\{ \frac{l(l+1)}{r^2} S_l^m(r) Y_l^m(\theta, \phi) \right\}, \quad (3.13)$$

$$B_{\theta} = \sum_{l=1}^{\infty} \sum_{m=-l}^l \left\{ \frac{T_l^m(r)}{r \sin \theta} \frac{\partial Y_l^m(\theta, \phi)}{\partial \phi} + \frac{1}{r} \frac{dS_l^m(r)}{dr} \frac{\partial Y_l^m(\theta, \phi)}{\partial \theta} \right\}, \quad (3.14)$$

$$B_{\phi} = \sum_{l=1}^{\infty} \sum_{m=-l}^l \left\{ -\frac{T_l^m(r)}{r} \frac{\partial Y_l^m(\theta, \phi)}{\partial \theta} + \frac{1}{r \sin \theta} \frac{dS_l^m(r)}{dr} \frac{\partial Y_l^m(\theta, \phi)}{\partial \phi} \right\}. \quad (3.15)$$

Thus, the toroidal-poloidal decomposition of \mathbf{B} with spherical harmonic expansion has been performed, as

$$\mathbf{B} = \sum_{l=1}^{\infty} \sum_{m=-l}^l (\mathbf{T}_l^m + \mathbf{S}_l^m) \quad (3.16)$$

The *curl* of \mathbf{T} is a poloidal field and the *curl* of \mathbf{S} is a toroidal field, i.e.

$$\text{curl} \mathbf{T}_l^m = \left\{ \frac{l(l+1)}{r^2} T_l^m(r) Y_l^m(\theta, \phi), \frac{1}{r} \frac{dT_l^m(r)}{dr} \frac{\partial Y_l^m(\theta, \phi)}{\partial \theta}, \frac{1}{r \sin \theta} \frac{dT_l^m(r)}{dr} \frac{\partial Y_l^m(\theta, \phi)}{\partial \phi} \right\}, \quad (3.17)$$

and

$$\text{curl} \mathbf{S}_l^m = \left\{ 0, \frac{Z_l^m(r)}{r \sin \theta} \frac{\partial Y_l^m(\theta, \phi)}{\partial \phi}, -\frac{Z_l^m(r)}{r} \frac{\partial Y_l^m(\theta, \phi)}{\partial \theta} \right\}, \quad (3.18)$$

where

$$Z_l^m = \frac{l(l+1)}{r^2} S_l^m - \frac{d^2 S_l^m}{dr^2}. \quad (3.19)$$

Moreover, $\text{curl}^2 \mathbf{T}_l^m$ results in a toroidal field again and $\text{curl}^2 \mathbf{S}_l^m$ represents a poloidal field, that is,

$$\text{curl}(\text{curl} \mathbf{T}_l^m) = \left(0, \frac{W_l^m(r)}{r \sin \theta} \frac{\partial Y_l^m(\theta, \phi)}{\partial \phi}, -\frac{W_l^m(r)}{r} \frac{\partial Y_l^m(\theta, \phi)}{\partial \theta} \right), \quad (3.20)$$

and

$$\text{curl}(\text{curl} \mathbf{S}_l^m) = \left(\frac{l(l+1)}{r^2} Z_l^m(r) Y_l^m(\theta, \phi), \frac{1}{r} \frac{dZ_l^m(r)}{dr} \frac{\partial Y_l^m(\theta, \phi)}{\partial \theta}, \frac{1}{r \sin \theta} \frac{dZ_l^m(r)}{dr} \frac{\partial Y_l^m(\theta, \phi)}{\partial \phi} \right). \quad (3.21)$$

where

$$W_l^m = \frac{l(l+1)}{r^2} T_l^m - \frac{d^2 T_l^m}{dr^2}. \quad (3.22)$$

Similarly, we can successively take the curl of toroidal and poloidal fields.

These properties of toroidal and poloidal fields are used to reduce the basic equations in the next subsection.

3.2 Basic equations and boundary conditions

In this subsection we present the basic equations of magnetoconvection in a rotating spherical shell within the Boussinesq approximation. As given in Section 2.2, the basic

equations consists of the equations of motion, electromagnetic induction and heat conduction supplemented by the equations of continuity and state, as

$$\begin{aligned} \frac{\partial \mathbf{u}}{\partial t} = & \mathbf{u} \times \boldsymbol{\omega} - \frac{1}{\rho_0} \boldsymbol{\nabla} \left(p + \frac{1}{2} \rho_0 |\mathbf{u}|^2 - \frac{1}{2} \rho_0 |\boldsymbol{\Omega} \times \mathbf{u}|^2 \right) \\ & - \nu \boldsymbol{\nabla} \times \boldsymbol{\nabla} \times \mathbf{u} + \frac{\rho}{\rho_0} \mathbf{g} + \frac{1}{\rho_0} \mathbf{J} \times \mathbf{B} - 2 \boldsymbol{\Omega} \times \mathbf{u}, \end{aligned} \quad (3.23)$$

$$\frac{\partial \mathbf{B}}{\partial t} = \boldsymbol{\nabla} \times (\mathbf{u} \times \mathbf{B}) - \lambda \boldsymbol{\nabla} \times \boldsymbol{\nabla} \times \mathbf{B}, \quad (3.24)$$

$$\frac{\partial T}{\partial t} + (\mathbf{u} \cdot \boldsymbol{\nabla}) T = \kappa \nabla^2 T, \quad (3.25)$$

$$\boldsymbol{\nabla} \cdot \mathbf{u} = 0, \quad (3.26)$$

$$\rho = \rho_0 \{1 - \alpha(T - T_0)\}, \quad (3.27)$$

where

$$\boldsymbol{\omega} = \boldsymbol{\nabla} \times \mathbf{u}, \quad (3.28)$$

$$\mathbf{J} = \frac{1}{\mu_0} \boldsymbol{\nabla} \times \mathbf{B}. \quad (3.29)$$

The symbols represent the same quantities as in Section 2. In the present model we assume that the gravity g is directly proportional to r as is relevant to a homogeneous sphere of constant density ρ_0 . Namely,

$$\mathbf{g} = (g(r), 0, 0), \quad \text{where } g(r) = -\frac{3}{4} \pi G \rho_0 r. \quad (3.30)$$

The system rotates counterclockwise with constant angular velocity, hence,

$$\boldsymbol{\Omega} = (\Omega \cos \theta, -\Omega \sin \theta, 0) \quad (3.31)$$

where Ω is a positive constant (Fig. 3.1).

The equation of motion (3.23) is reduced in the similar way described in Section 2.

We take the *curl* of Eq. (3.25) and obtain the equation for $\boldsymbol{\nabla} \times \mathbf{u} (= \boldsymbol{\omega})$ written by

$$\frac{\partial}{\partial t} (\boldsymbol{\nabla} \times \mathbf{u}) = \boldsymbol{\nabla} \times \left(\mathbf{u} \times \boldsymbol{\omega} + \frac{\rho}{\rho_0} \mathbf{g} + \frac{1}{\rho_0} \mathbf{J} \times \mathbf{B} - 2 \boldsymbol{\Omega} \times \mathbf{u} \right) - \nu \boldsymbol{\nabla} \times \boldsymbol{\nabla} \times \boldsymbol{\omega}. \quad (3.32)$$

From the r -component of Eq. (3.32) the equation for the toroidal scalar function of the velocity field, T_{Vl}^m is obtained ;

$$\frac{\partial T_{Vl}^m}{\partial t} = \frac{r^2}{l(l+1)} \left[\nabla \times \left(\mathbf{u} \times \boldsymbol{\omega} + \frac{1}{\rho_0} \mathbf{J} \times \mathbf{B} - 2\boldsymbol{\Omega} \times \mathbf{u} \right) \right]_l^m + \nu \left\{ \frac{\partial^2 T_{Vl}^m}{\partial r^2} - \frac{l(l+1)}{r^2} T_{Vl}^m \right\} \quad (3.33)$$

Taking the *curl* of Eq. (3.32) again, the equation for $\nabla \times \nabla \times \mathbf{u}$ results in

$$\begin{aligned} \frac{\partial}{\partial t}(\nabla \times \nabla \times \mathbf{u}) &= \nabla \times \nabla \times \left(\mathbf{u} \times \boldsymbol{\omega} + \frac{\rho}{\rho_0} \mathbf{g} + \frac{1}{\rho_0} \mathbf{J} \times \mathbf{B} - 2\boldsymbol{\Omega} \times \mathbf{u} \right) \\ &\quad - \nu \nabla \times \nabla \times \nabla \times \boldsymbol{\omega} . \end{aligned} \quad (3.34)$$

Using the r -component of Eq. (3.17), the equation for Z_{Vl}^m becomes

$$\begin{aligned} \frac{\partial Z_{Vl}^m}{\partial t} &= \frac{r^2}{l(l+1)} \left[\nabla \times \nabla \times \left(\mathbf{u} \times \boldsymbol{\omega} + \frac{1}{\rho_0} \mathbf{J} \times \mathbf{B} - 2\boldsymbol{\Omega} \times \mathbf{u} \right) \right]_l^m \\ &\quad - g(r)\alpha T + \nu \left\{ \frac{\partial^2 Z_{Vl}^m}{\partial r^2} - \frac{l(l+1)}{r^2} Z_{Vl}^m \right\} \end{aligned} \quad (3.35)$$

We obtain the equation for the poloidal scalar function of the magnetic field, S_{Ml}^m from the r -component of the induction equation (3.24), written by

$$\frac{\partial S_{Ml}^m}{\partial t} = \frac{r^2}{l(l+1)} [\nabla \times (\mathbf{u} \times \mathbf{B})]_l^m + \lambda \left\{ \frac{\partial^2 S_{Ml}^m}{\partial r^2} - \frac{l(l+1)}{r^2} S_{Ml}^m \right\} \quad (3.36)$$

Taking the *curl* of the induction equation (3.24), we have

$$\begin{aligned} \frac{\partial}{\partial t}(\nabla \times \mathbf{B}) &= \nabla \times \nabla \times (\mathbf{u} \times \mathbf{B}) \\ &\quad - \lambda \nabla \times \nabla \times \nabla \times \mathbf{B}, \end{aligned} \quad (3.37)$$

Using the r -component of Eq. (3.37), we obtain the equation for the toroidal scalar function of the magnetic field, given by,

$$\frac{\partial T_{Ml}^m}{\partial t} = \frac{r^2}{l(l+1)} [\nabla \times \nabla \times (\mathbf{u} \times \mathbf{B})]_l^m + \lambda \left\{ \frac{\partial^2 T_{Ml}^m}{\partial r^2} - \frac{l(l+1)}{r^2} T_{Ml}^m \right\} \quad (3.38)$$

Thus, the basic equations of the velocity and magnetic fields have been obtained. We rewrite the equation of heat conduction by separating the temperature field T into the thermal conduction field T_{ref} and the deviation field \hat{T} from T_{ref} , that is,

$$T(r, \theta, \phi) = T_{ref} + \hat{T}(r, \theta, \phi) \quad (3.39)$$

Since we assume that there is no heat source in a shell and the temperature on the inner and outer boundary surface is uniform, the thermal conduction profile results in

$$T_{ref} = \beta_0 + \frac{\beta_1}{r} \quad (3.40)$$

The equation for \hat{T} is given by

$$\frac{\partial T}{\partial t} = \frac{\beta_1}{r^2} u_r - (\mathbf{u} \cdot \nabla) T + \kappa \nabla^2 T \quad (3.41)$$

From now on, \hat{T} is expressed as T for simplicity. We obtain the non-dimensional form of the basic equations, using the outer radius R_0 as the scale of length, R_0^2/κ as the scale of time, β_1/R_0 as the scale of temperature and $\sqrt{\rho_0\mu_0\kappa}/L$ as scale of the magnetic field. Thus, the non-dimensional basic equations are written by

$$\begin{aligned} \frac{\partial T_{Vl}^m}{\partial t} &= \frac{r^2}{l(l+1)} [\nabla \times (\mathbf{u} \times \boldsymbol{\omega} + \mathbf{J} \times \mathbf{B} - 2\boldsymbol{\Omega} \times \mathbf{u})]_l^m \\ &+ P_r \left\{ \frac{\partial^2 T_{Vl}^m}{\partial r^2} - \frac{l(l+1)}{r^2} T_{Vl}^m \right\} \end{aligned} \quad (3.42)$$

$$\begin{aligned} \frac{\partial Z_{Vl}^m}{\partial t} &= \frac{r^2}{l(l+1)} [\nabla \times \nabla \times (\mathbf{u} \times \boldsymbol{\omega} + \mathbf{J} \times \mathbf{B} - 2\boldsymbol{\Omega} \times \mathbf{u})]_l^m \\ &- g(r) \alpha T + P_r \left\{ \frac{\partial^2 Z_{Vl}^m}{\partial r^2} - \frac{l(l+1)}{r^2} Z_{Vl}^m \right\} \end{aligned} \quad (3.43)$$

$$\frac{\partial S_{Ml}^m}{\partial t} = \frac{r^2}{l(l+1)} [\nabla \times (\mathbf{u} \times \mathbf{B})]_l^m + \frac{P_r}{P_{rM}} \left\{ \frac{\partial^2 S_{Ml}^m}{\partial r^2} - \frac{l(l+1)}{r^2} S_{Ml}^m \right\} \quad (3.44)$$

$$\frac{\partial T_{Ml}^m}{\partial t} = \frac{r^2}{l(l+1)} [\nabla \times \nabla \times (\mathbf{u} \times \mathbf{B})]_l^m + \frac{P_r}{P_{rM}} \left\{ \frac{\partial^2 T_{Ml}^m}{\partial r^2} - \frac{l(l+1)}{r^2} T_{Ml}^m \right\} \quad (3.45)$$

$$\frac{\partial T}{\partial t} = \frac{1}{r^2} u_r - (\mathbf{u} \cdot \nabla) T + \nabla^2 T . \quad (3.46)$$

In the above equations, the non-dimensional numbers, i.e., B_C (the boundary parameter), T_a (the Taylor number), P_r (the Prandtl number) and P_{rM} (the magnetic Prandtl number) are defined as,

$$B_C = \frac{g\alpha\beta_1 R_0^2}{\nu\kappa}, T_a = \frac{4\Omega^2 R_0^4}{\nu^2}, P_r = \frac{\nu}{\kappa}, P_{rM} = \frac{\nu}{\lambda} .$$

The time integration of these non-dimensional equations is performed by the numerical analysis method described in next section. Now, we consider the boundary conditions of the velocity and magnetic fields. Since both the inner and outer boundaries are assumed to be rigid, for $r = 0.4$ and $r = 1$

$$\mathbf{u} = 0 . \quad (3.47)$$

From Eqs. (3.47) and (3.11) and (3.12), on the boundary surface

$$T_{Vl}^m = 0, \quad S_{Vl}^m = 0, \quad \frac{dS_{Vl}^m}{dr} = 0. \quad (3.48)$$

Therefore, from Eq. (3.19)

$$Z_{Vl}^m = -\frac{d^2 S_{Vl}^m}{dr^2}. \quad (3.49)$$

To obtain the boundary condition for \mathbf{B} and \mathbf{J} we rewrite Eq. (3.1) as

$$\mathbf{B} = \nabla \times \left(\Psi \frac{\mathbf{r}}{r} \right) + \nabla \left(\frac{\partial \Phi}{\partial r} \right) - \mathbf{r} \nabla^2 \left(\frac{\Phi}{r} \right) \quad (3.50)$$

Hence, $\mathbf{J}(= \nabla \times \mathbf{B})$ is expressed as

$$\mathbf{J} = \nabla \times \nabla \times \left(\Psi \frac{\mathbf{r}}{r} \right) - \nabla \left\{ \mathbf{r} \nabla^2 \left(\frac{\Phi}{r} \right) \right\} \quad (3.51)$$

Since the exterior region ($r > R_o$) of the shell, corresponding to the Earth's mantle, is assumed to be an electric insulator, no electric current crosses the outer boundary, that

is,

$$J_r = 0 \quad \text{for } r = R_o = 1. \quad (3.52)$$

Therefore, it follows from Eq. (3.51),

$$T_{Ml}^m = 0, \quad \nabla^2 S_{Ml}^m = 0. \quad (3.53)$$

Since $\nabla \times \mathbf{B} = 0$ in an insulator, \mathbf{B} is written in terms of a scalar potential V ;

$$\mathbf{B} = -\nabla V \quad (3.54)$$

By expanding in spherical harmonics series, V is given by

$$V = R_o \sum_{l,m} f_l^m(r) Y_l^m(\theta, \phi) \left(\frac{R_o}{r} \right)^{l+1}. \quad (3.55)$$

Meanwhile, as \mathbf{T} is zero in an insulator, \mathbf{B} is given by

$$\mathbf{B} = \nabla \times \nabla \times \left(\Phi \frac{\mathbf{r}}{r} \right), \quad (3.56)$$

From the r -component of Eqs. (3.54) and (3.56), it follows that

$$\frac{l}{r^2} S_{Ml}^m = f_l^m \left(\frac{R_o}{r} \right)^{l+2}. \quad (3.57)$$

Using the θ (or ϕ)-component of Eqs. (3.54) and (3.56), we have

$$\frac{\partial S_{Ml}^m}{\partial r} = -r f_l^m \left(\frac{R_o}{r} \right)^{l+2}. \quad (3.58)$$

Thus, we obtain the condition for S_{Ml}^m on the outer boundary surface from Eqs. (3.57)

and (3.58), i.e.

$$\frac{\partial S_{Ml}^m}{\partial r} + \frac{l}{r} S_{Ml}^m = 0. \quad (3.59)$$

The interior region ($r < R_o$) of the shell, corresponding to the Earth's inner core, is assumed to be the electric conducting solid whose conductivity is the same with that of the

conducting fluid in the shell. Therefore, the magnetic field in the outer core is smoothly connected to that in the inner core on the inner boundary surface. The magnetic field in the inner core is obtained by solving the diffusion equation of the magnetic field, i.e.

$$\frac{\partial T_{Ml}^m}{\partial t} = \frac{r^2}{l(l+1)} + \lambda \left\{ \frac{\partial^2 T_{Ml}^m}{\partial r^2} - \frac{l(l+1)}{r^2} T_{Ml}^m \right\} \quad (3.60)$$

$$\frac{\partial S_{Ml}^m}{\partial t} = \frac{r^2}{l(l+1)} + \lambda \left\{ \frac{\partial^2 S_{Ml}^m}{\partial r^2} - \frac{l(l+1)}{r^2} S_{Ml}^m \right\} \quad (3.61)$$

The time evolution of the basic equations under the obtained boundary conditions are carried out by the numerical analysis method described in the next subsection.

3.3 Methods of numerical analysis - Algorithm for simulation

For the model and basic equations of magnetoconvection in a rotating spherical shell given in the previous section, numerical simulation has been made applying the following procedure. In the first step, the time integration of $T_{Vl}^m, Z_{Vl}^m, S_{Ml}^m, T_{Ml}^m$ and T_l^m is carried out using Eqs. (3.42) to (3.46) followed by the second step where the poloidal scalar function of the velocity field S_{Vl}^m is obtained from Z_{Vl}^m by solving the Poisson equation (3.19). In the third step, $\mathbf{u}, \boldsymbol{\omega}, \mathbf{B}, \mathbf{J}$ and \mathbf{T} in the physical space are calculated from $S_{Vl}^m, T_{Vl}^m, Z_{Vl}^m, S_{Ml}^m, T_{Ml}^m$ and T_l^m including the processes to acquired the non-linear terms in the physical space. In the final step, these nonlinear terms are transformed into the spectral space. Thus, the evolution of one time-step has been completed.

We use the pseudo-spectral method with spherical harmonic expansion to evaluate the spatial derivatives in the horizontal (i.e. θ, ϕ) direction (Orszag, 1980). In the spherical shell model the quantities, T_V, S_V and others are expanded in spherical harmonic series. The derivative with respect to θ is calculated by using recursion formulae of the associated

Legendre function, such as

$$\sin \theta \frac{dP_l^m}{d\theta} = \frac{1}{2l+1} \left\{ l(l-m+1)P_{l+1}^m - (l+1)(l+m)P_{l-1}^m \right\}, \quad (3.62)$$

and

$$\cos \theta P_l^m = \frac{1}{2l+1} \left\{ (l-m+1)P_{l+1}^m + (l+m)P_{l-1}^m \right\}. \quad (3.63)$$

The derivative with respect to ϕ is readily obtained by the nature of the trigonometric function. In the vertical (r) direction, the spatial derivative is evaluated by the second-order finite difference method. The time integration is performed by the improved Euler method as in Section 2. To calculate the nonlinear terms in a simple way, the following treatment of the nonlinear terms are applied (Glatzmaier, 1984). For non-linear term \mathbf{F} which represents terms, such as $\mathbf{u} \times \boldsymbol{\omega}$, $\mathbf{u} \times \mathbf{B}$ and $\mathbf{u}T$, quantities, f_1, f_2 and f_3 are defined as

$$f_1 = r^2 F_r, \quad f_2 = \frac{F_\theta}{r \sin \theta}, \quad f_3 = \frac{F_\phi}{r \sin \theta}. \quad (3.64)$$

Since the nonlinear terms appear in the form of $[\nabla \times \mathbf{F}]_r$, $[\nabla \times \nabla \times \mathbf{F}]_r$ and $[\nabla \cdot \mathbf{F}]_r$, in the basic equations, the nonlinear terms are written by using f_1, f_2 and f_3 as

$$[\nabla \times \mathbf{F}]_r = 2 \cos \theta f_3 + \sin \theta \frac{\partial f_3}{\partial \theta} - \frac{\partial f_2}{\partial \phi}, \quad (3.65)$$

$$[\nabla \times \nabla \times \mathbf{F}]_r = \frac{1}{r^4} L^2 f_1 + \frac{1}{r^2} \frac{\partial}{\partial r} \left[r^2 \left\{ 2 \cos \theta f_2 + \sin \theta \frac{\partial f_2}{\partial \theta} + \frac{\partial f_3}{\partial \phi} \right\} \right], \quad (3.66)$$

$$[\nabla \cdot \mathbf{F}]_r = \frac{1}{r^2} \frac{\partial f_1}{\partial r} + 2 \cos \theta f_2 + \sin \theta \frac{\partial f_2}{\partial \theta} + \frac{\partial f_3}{\partial \phi}. \quad (3.67)$$

Therefore, after transforming f_1, f_2 and f_3 to the spectral space, we can calculate these nonlinear terms by utilizing the recursion formulae presented above. To transform the quantities in the physical space into the spectral space, we use a Gaussian quadrature for the Legendre transform in colatitude and apply a Fast Fourier Transform scheme for the Fourier transform in longitude.

Here, we should note our treatment for solving the diffusion equation of the magnetic field in the inner core. The directly solving scheme is however suffered from numerical instability in the vicinity of the origin $r = 0$. To inhibit the instability, therefore, we have applied a technical solution by decreasing the magnetic field near the origin multiplying the function for $r \leq 0.2$.

$$G(r) = \exp \left\{ -\frac{(r - 0.2)^2}{h^2} \right\} \quad (3.68)$$

In the present simulation the value of h in Eq. (3.68) is chosen to 0.1. The effect of this treatment will be discussed in Section 5.

In the present calculation, the number of the mesh points in the r direction is set to be 30. The spherical harmonic expansion is performed up to degree 10. The number of the colatitudinal collocation points for Gaussian quadrature is chosen to 16, and that of the longitudinal collocation points for Fourier transform is 32. The interval for the time evolution is set to be 1.0×10^{-4} .

At the initial time of the simulation, the fluid is at rest and a perturbation is given to the temperature field to cause convection. The weak magnetic field with low degree of the spherical harmonics is assumed initially.

We have numerically investigated the critical value of the buoyancy parameter B_c for the various degrees of the spherical harmonics in the case when heat source exists only in a shell and distributes uniformly in a shell. These numerical results have been compared with the critical value derived by the linear stability theory (Chandrasekhar, 1961). The critical values obtained by our calculation is slightly smaller than the values of the linear theory. In general, however, the present results are consistent with those of the linear theory.

The simulations were carried out on the NEC SX-2N and Fujitsu VP-200 computers.

On the SX-2N computer, the time integration of 5000 time-steps requires about 110 minutes.

3.4 Results and discussion

3.4.1 Velocity field

Before considering the magnetic field generation, we present the results of the obtained velocity field and discuss the effect of rotation on convection. Although the results reported in this subsection contain the magnetic field, the magnetic energy is much smaller than the kinetic energy throughout the computational run. Therefore, the effect of the magnetic field on convection can be neglected, i.e. the system is in the kinematic state.

(a) Effect of rotation on convection

As in Section 2, we show the results for $T_a = 0$ (non-rotating case referred to Run 1) and $T_a = 1.6 \times 10^5$ (rotating case referred to Run 2) in parallel to see the rotation effect clearly. Other non-dimensional parameters are set as $B_C = 5.0 \times 10^4$, $P_r = 1$ and $P_{rM} = 1$. The initial perturbation of the temperature field contains the all spherical harmonic modes with degree $l = 1$ and 2. The radial dependence of all these modes is assumed to be

$$T_l^m(r, t = 0) = 0.01\{0.3^2 - (r - 0.7)^2\} \quad (3.69)$$

Since non-axisymmetric convection appears in the present simulation, the convective pattern changes with latitude. Therefore, we present a typical pattern on a meridional plane though in some cases several patterns on the various meridional planes and the longitudinally averaged pattern are given.

In Fig. 3.2 the velocity field \mathbf{u} in the meridional plane at $\phi = \pi/8$ (Fig. 3.2(a)) and $\phi = \pi/4$ (Fig. 3.2(b)) at $t = 0.5$ is indicated. In the non-rotating case (Fig. 3.2(a)), a simple convective appears for a case of relatively small buoyancy parameter. Four rolls is pattern is generated in this meridional plane with two upward and two downward flows. In the rotating case (Fig. 3.2(b)) the number of the regions for upward and downward flows becomes larger and the horizontal scale of convection becomes smaller than those of the non-rotating case. The contour plot of u_ϕ in the meridional plane at $\phi = \pi/8$ (Fig. 3.3(a)) and $\phi = \pi/4$ (Fig. 3.3(b)) is shown in Fig. 3.3 where thin and thick lines represent respectively the fluid motion into and out of the sheet plane of the diagram (meridional plane) and the interval between the contour lines is 2. In the non-rotating case (Fig. 3.3(a)) a simple structure is formed, and the boundary between the region with positive u_ϕ and that with negative u_ϕ is nearly parallel to the spherical surface. On the other hand, in the rotating case the boundary between the region with positive u_ϕ and that with negative u_ϕ is approximately parallel to the rotation axis of the shell, indicating the existence of the convective roll whose axis is approximately parallel to the rotation axis. The appearance of such a cylindrical convective rolls is consistent with the theoretical and experimental studies of convection in a rotating spherical shell (Busse, 1970 ; Busse and Carrigan, 1976 ; Hart, Glatzmaier and Toomre, 1986). Near the north pole an upward flow exists. Since the Coriolis force affects in the polar region, the horizontal flow in the bottom side, makes convergence toward the region of the upward flow with counterclockwise rotation and diverges in the top of the upward flow with clockwise rotation. This situation is similar to that of the plane boundary model discussed in Section 2.4. There is a upward flow in the south polar region too. Therefore, the helical flow similar to that in the north polar region appears though rotation is clockwise (counterclockwise) in the bottom (top

) region. The longitudinally averaged velocity $\langle \mathbf{u} \rangle$ in the meridional plane is shown in Fig. 3.4 where unit length of the arrow in the non-rotating case expresses five times larger value than that in the rotating case. Namely, the meridional circulation in the non-rotating case is larger than that in the rotating case. The contour plot of the values of $\langle u_\phi \rangle$ is given in Fig. 3.5 where the interval between the contour lines is 0.02 for the non-rotating case and 0.4 for the rotating case. In the rotating case, the differential rotation is effectively generated and becomes strong in low latitudes. In the polar region, the differential rotation associated with helical flow described above appears.

The velocity field \mathbf{u} in the equatorial plane is shown in Fig. 3.6 where the non-axisymmetric convective pattern is clearly seen. In the non-rotating case there are two upward and two downward flows in the equatorial plane. Meanwhile, four upward and four downward flows exist for the rotating case. Four remarkable rolls, whose longitudinal scale is smaller than that of rolls for $T_a = 0$ are formed. The contour map of u_θ in the equatorial plane is given in Fig. 3.7. The meaning of the thin and thick lines and the interval of the contour lines are same as those in Fig. 3.3. For the non-rotating case the contour map shows similarity to that in the meridional plane (Fig. 3.3(a)) because there is no special difference of the condition between the meridional and equatorial planes. On the contrary, the contour plot for the rotating case in the equatorial plane is quite different from that in the meridional plane (Figs. 3.7(b) and 3.3(b)). The velocity component, u_θ is apparently small in the equatorial plane, reflecting the symmetric nature of convection with respect to the equatorial plane. Although we are adopting the initial perturbation which contains both symmetric and anti-symmetric mode with respect to the equatorial plane, a nearly symmetric convective flow appears as a result of the rotation effect. To see the horizontal structure of convection, we present the contour map of u_r on the spherical

surface $r = 0.7$ in Fig. 3.8. In the non-rotating case, we can see the simple convective pattern with two marked upward flow appears. On the other hand, the pattern shows a complicated feature in the rotating case. The longitudinal scale of convection becomes rather small compared with that in the non-rotating case. Convection contains four upward and four downward flows, and the region of these flows extends in the north-south direction, indicating the convective rolls whose axes are approximately parallel to the rotation axis.

(b) Distribution of helicity density

In Fig. 3.9, the helicity density h for $T_a = 0$ is given in several meridional planes; thin and thick lines represent, respectively, positive and negative values and the interval of the contour lines is 20. When the convective velocity is infinitesimal, i.e. the linear theory is applicable, the convective flow is purely poloidal (Chandrasekhar, 1961) in the non-rotating case. Consequently, h is equal to zero everywhere in the system. In the present state, the convective velocity takes a finite value and the advection term generates h as has been obtained in the plane boundary model described in Section 2.4(a). However, the magnitude of h is much smaller than that for $T_a = 1.6 \times 10^5$ which is shown in Fig. 3.10. In the rotating case, the helical motion is enhanced due to the Coriolis force, resulting the large h value. Although the distribution of h varies with longitude, these patterns on the various meridional planes show a common feature. Namely, in the northern hemisphere h is roughly negative in the region out of the cylindrical plane which is adjoining the inner boundary and whose axis is parallel to the rotation axis. In the region within the cylindrical plane h is approximately positive in the bottom part and negative in the top part, and the absolute value of h in the bottom part is larger than that in the top part. In the southern hemisphere, the sign of h is opposite to that

in the northern hemisphere and the distribution of h is similar to that in the northern hemisphere except for the sign of h . These characteristics of the distribution of h is more clearly shown by averaging h in the longitudinal direction. We present the contour map of the longitudinally averaged helicity density $\langle h \rangle$ in Fig. 3.11 where the interval between the contour lines is 100. A similar distribution of h has been obtained by Gilman and Miller (1981) though several conditions of Gilman and Miller (1981), such as the boundary condition for the velocity field and the radial dependence of the gravity field, are different from those of the present simulation. Therefore, the distribution of $\langle h \rangle$ shown in Fig. 3.11 is considered as a typical one for convection in a rotating spherical shell within the Boussinesq approximation. A schematic description of the generation mechanism of h has been provided in Gilman (1983). Since the simulation of Gilman and Miller (1981) have treated the region between latitude 75° north and 75° south in their simulation, the weakly negative h region near the north pole which appears in our simulation could not be seen in their result. This weak negative region near the north pole, however, does not exist in the case of the low Prandtl number as shown below.

We present another result referred here to Run 3 in which the radial dependence of the initial perturbation of the temperature field is given by

$$T_l^m(r, t = 0) = -0.01\{0.3^2 - (r - 0.7)^2\} , \quad (3.70)$$

that is, the sign of T_{dis} is opposite to that in Run 1 and Run 2. The spherical harmonic modes of T_{dis} and the non-dimensional numbers are same as in Run 2. The velocity field \mathbf{u} at $t = 0.4$ is shown in Fig. 3.12. In Fig. 3.12(a) \mathbf{u} in the meridional plane is indicated. The convective pattern is similar to that of Run 2 (Fig. 3.2(b)) though the initial condition is different. The contour plot of u_ϕ is shown in Fig. 3.12(b) where the interval of the contour lines is 4. The convective rolls with axes approximately parallel to the

rotation axis appear as in Run 2. In the polar region, the vortexes accompanied by the upward and downward flows are seen. The velocity field of \mathbf{u} on the equatorial plane is given in Fig. 3.12(c) which is similar to that of Run 2. Four remarkable rolls appear as in Fig. 3.4(b). In the equatorial plane, u_θ is so weak that only zero value line is indicated in the contour map for the interval 4 (Fig. 3.12(d)), reflecting the symmetric structure of convection with respect to the equatorial plane.

The longitudinally averaged velocity $\langle \mathbf{u} \rangle$ is shown in Fig. 3.13. The meridional motion shown in Fig. 3.13(a) is similar to that for Run 2 (Fig. 3.3(b)) though the initial condition for Run 3 is different from that for Run 2. The upward flow exists in the polar and equatorial region. The contour plot of $\langle u_\phi \rangle$ is given in Fig. 3.13(b) where the interval between the contour lines is 0.4. There is a remarkable similarity between the differential rotation for Run3 and that for Run2 (Fig. 3.5(b)). Namely, the differential rotation is strong in low latitudes, and the vortex structure of the convective motion appears in the polar region.

We indicate the contour map of the longitudinally averaged helicity density $\langle h \rangle$ in Fig. 3.14. where the interval between of the contour lines is 100. The distribution of $\langle h \rangle$ for Run 3 is very similar to that for Run 2 (Fig. 3.11). Hence, $\langle h \rangle$ given in Figs 3.11 and 14 is considered as a typical one for convection in a rotating spherical shell. Namely, in the northern (southern) hemisphere $\langle h \rangle$ is approximately negative (positive) out of the cylindrical surface which is adjoining the inner boundary and positive (negative) within the cylindrical surface except for the top region with small negative $\langle h \rangle$.

To study the time evolution of the convective motion, \mathbf{u} in the equatorial plane at different four times $t = 0.36, 0.37, 0.38$ and 0.39 is given in Fig. 3.15. The velocity field

\mathbf{u} at $t = 0.4$ in the equatorial plane has been given in Fig. 3.12(c). From Figs. 3.15 and 3.12(c) it is found that the convective pattern drifts longitudinally and that the direction of the drift is westward. To see this drift motion more clearly, the contour plots of u_ϕ on a meridional plane at various times are given in Fig. 3.16. Figures 3.16 and 3.12(b) together with Figs. 3.15 and 3.12(c) indicate the westward drift of the convective motion.

In the simulation 'Run 4' the non-dimensional parameters are set as , $B_C = 5.0 \times 10^4$, $T_a = 6.4 \times 10^5$, $P_r = 0.5$ and $P_{rM} = 1.0$. The initial condition of the temperature field is same as that of Run 3. Because of the larger value of T_a and the lower value of B_C and P_r than those of Run 2 and Run 3, the effect of rotation on convection is larger than that for Run 2 and Run 3. The velocity field \mathbf{u} at $t = 0.5$ is indicated in Fig. 3.17. In Fig. 3.17(a) \mathbf{u} in a meridional plane is given. The nearly symmetric convective motion is generated though the initial perturbation contains both symmetric and anti-symmetric modes with respect to the equatorial plane. In the polar region, the convective velocity is small. The contour map of u_ϕ on a meridional plane is given in Fig. 3.17(b) where the interval of contour lines is 1. In the region out of the cylindrical plane explained above, the convective rolls with axes approximately parallel to the rotation axis exist. Meanwhile, in the cylindrical plane vortexes appear. We indicate \mathbf{u} on the equatorial plane in Fig. 3.17(c) where several remarkable rolls are indicated. The convective motion is periodic in the longitudinal direction with period π though the initial condition of the temperature includes both $\cos m\phi$ and $\sin m\phi$ terms for $0 \leq m \leq 2$. Reflecting the symmetric property of the convective motion, only zero value line exists in the contour map of u_θ on the equatorial plane for the contour interval 1 (Fig. 3.17(d)). The longitudinally averaged velocity $\langle \mathbf{u} \rangle$ is indicated in Fig. 3.18 where the interval between the contour lines is 0.1. The differential rotation becomes strong in low latitudes. The vortex structure

in the polar region is apparent. We show the contour map of $\langle h \rangle$ in Fig. 3.19 where the interval between contour lines is 20. The distribution of $\langle h \rangle$ is similar to that for Run 2 and Run 3 though the weak negative (positive) region near the north (south) pole is can not be seen in Run 4.

Thus, we have studied the effect of rotation on convection. The common features of the convective motion for the rotating case are;

i) appearance of the convective rolls whose axes are parallel to the rotation axis and whose longitudinal scales are small compared with that in the non-rotating case, ii) symmetric nature of convection with respect to the equatorial plane, iii) the westward drift of convection, iv) the effective generation of the differential rotation, v) the large value of the helicity density, and vi) characteristic distribution of the helicity density described above.

The obtained convection contains the helical motion and differential rotation which are supposed to facilitate the magnetic field generation.

(c) Magnetic field

We focus our attention on the poloidal magnetic field with spherical harmonics with degree 1, i.e. the dipole field and the toroidal magnetic field with degree 2. These modes are supposed to play major roles in the large-scale, laminar dynamo process (Bullard and Gellman, 1954 ; Lilley, 1970). At the initial time of the simulation, weak poloidal and toroidal magnetic fields are given containing all spherical harmonics with degree 1 and 2. In all of four cases presented above, the magnetic field energy eventually vanishes. Figure 3.20 shows the temporal variation of S_{M1}^0 , S_{M1}^1 , and S_{M1}^{-1} on the spherical surface $r = 0.7$ for Run 1 and Run 2. For both non-rotating and rotating cases these scalar functions decrease with time though the decay rate of the rotating case is smaller than

that of the non-rotating case. The time evolution of these poloidal and toroidal scalar functions for Run 3 and Run 4 is given in Fig. 3.21 and 22 respectively. Both for Run 3 and Run 4 the amplitudes of these modes vanishes in the last period. However, for Run 3 the toroidal scalars exhibit complicated variation. The initial value of the toroidal scalars are about one-tenth of that of the poloidal scalars. The variation of T_{M2}^1 and T_{M2}^{-1} is large compared with other toroidal scalars; the amplitudes of T_{M2}^1 and T_{M2}^{-1} becomes several ten times larger than their initial values and change the sign during the evolution process. These complicated behaviors of the toroidal scalars can not be explained by the free decay process of the magnetic field, but the result is suggesting that there exists a generation process. In contrast with the toroidal scalars, the poloidal scalars decrease almost monotonically. For Run 4 the toroidal and poloidal scalars decrease with time though the toroidal scalars indicate T_{M2}^0 , T_{M2}^1 and T_{M2}^{-1} shows a little increase during the time evolution.

As indicated above, the velocity field in the rotating case contains the helical motion and differential rotation. However, the regenerative process does not occur in the above cases.

Another computational run referred to Run 5 is performed in which the non-dimensional parameters of Run 5 are chosen as, $B_C = 1.0 \times 10^5$, $T_a = 6.4 \times 10^5$, $P_r = 0.5$ and $P_{rM} = 2.5$. The toroidal and poloidal scalars as a function of time for Run 5 are given in Fig. 3.23. Although the time variation of the toroidal and poloidal scalars is much larger than those of Run 1 to Run 4, these scalar functions decrease with time, i.e. regeneration process does not occur.

Moreover, computational run referred to Run 6 with larger P_{rM} than that for Run 5 is carried out. The non-dimensional parameters of Run 6 are $B_C = 1.0 \times 10^5$, $T_a =$

6.4×10^5 , $P_r = 0.5$ and $P_{rM} = 2.5$. The time evolution of the toroidal and poloidal scalars as a function of time for Run 6 are given in Fig. 3.24. The amplitudes of the toroidal and poloidal scalars become much larger than the initial value and show the large variation including the reversals of the sign. However, the obtained magnetic field is rather intermittent as indicated in Fig. 3.25 and contains relatively large amplitude in the spherical harmonics with high degree. These features of the obtained magnetic field are not relevant to take as the origin of the geomagnetic field.

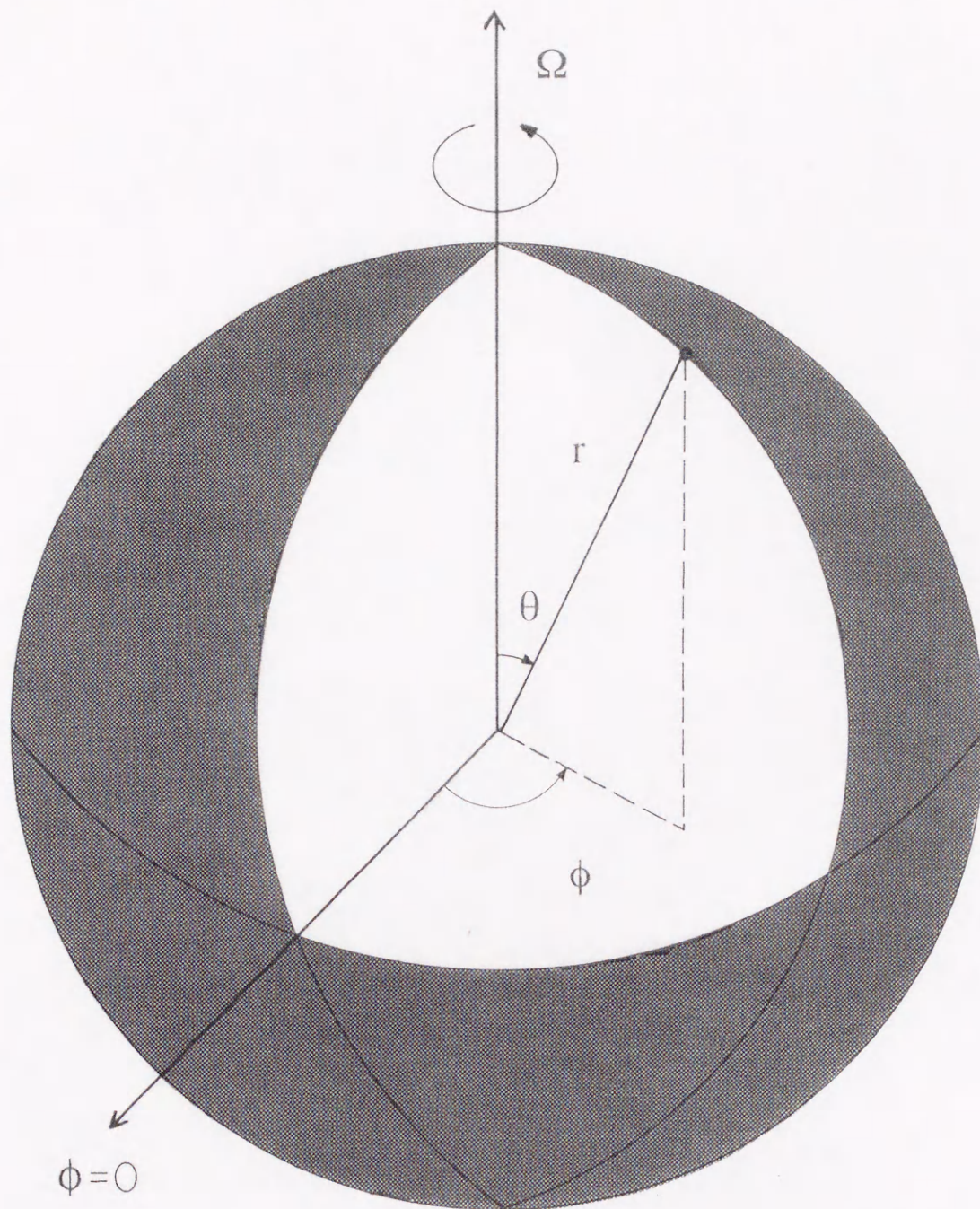


Figure 3.1 The coordinate of the spherical shell model.

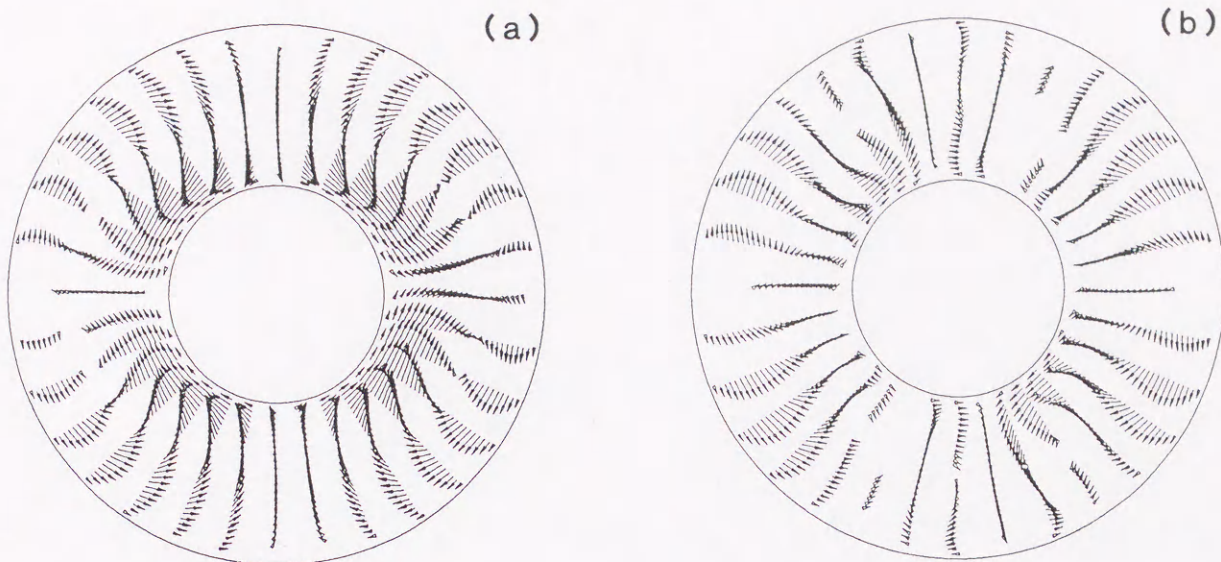


Figure 3.2 Velocity field at $t=0.5$ in the meridional plane at $\phi = \pi/8$ for Run 1 (a) and at $\phi = \pi/4$ for Run 2 (b).

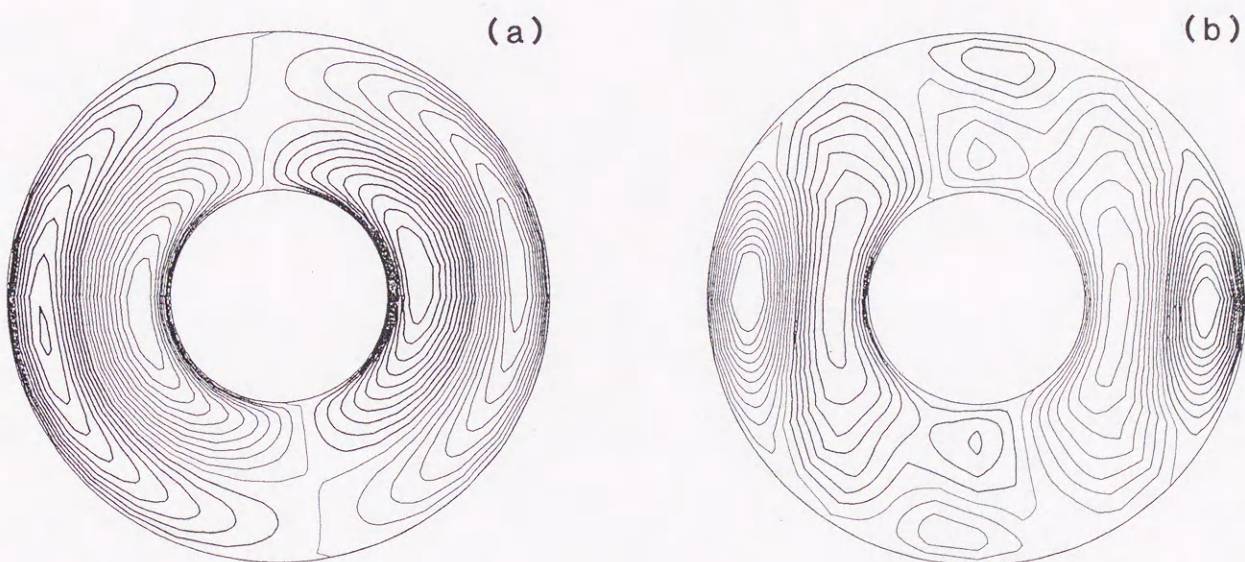


Figure 3.3 Contour plots of u_ϕ on the meridional plane. Same conditions as in Fig. 3.2. Thin lines represent the fluid motion into the paper and thick lines out of the paper. The interval of the contour lines is 2.

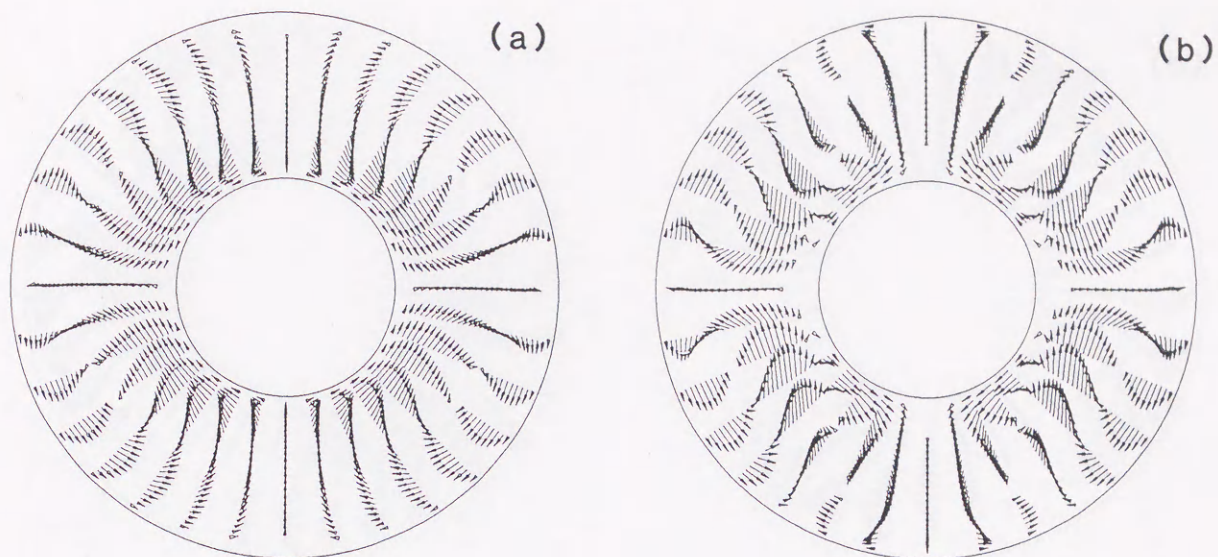


Figure 3.4 Longitudinally averaged velocity $\langle u \rangle$ at $t=0.5$ in the meridional plane for Run 1 (a) and Run 2 (b) cases. The unit length of the arrow in the non-rotating case expresses five times larger value than that in the rotating case

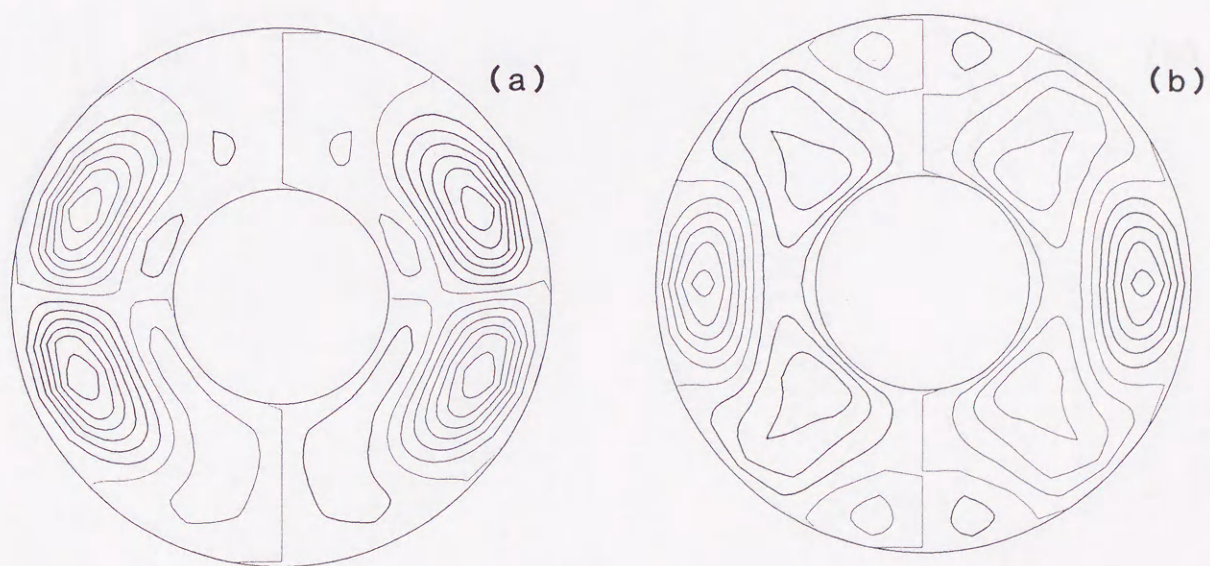


Figure 3.5 Contour plots of $\langle u_\phi \rangle$ at $t=0.5$ for Run 1 (a) and Run 2 (b). The interval between the contour lines is 0.02 for the non-rotating case and 0.4 for the rotating case.

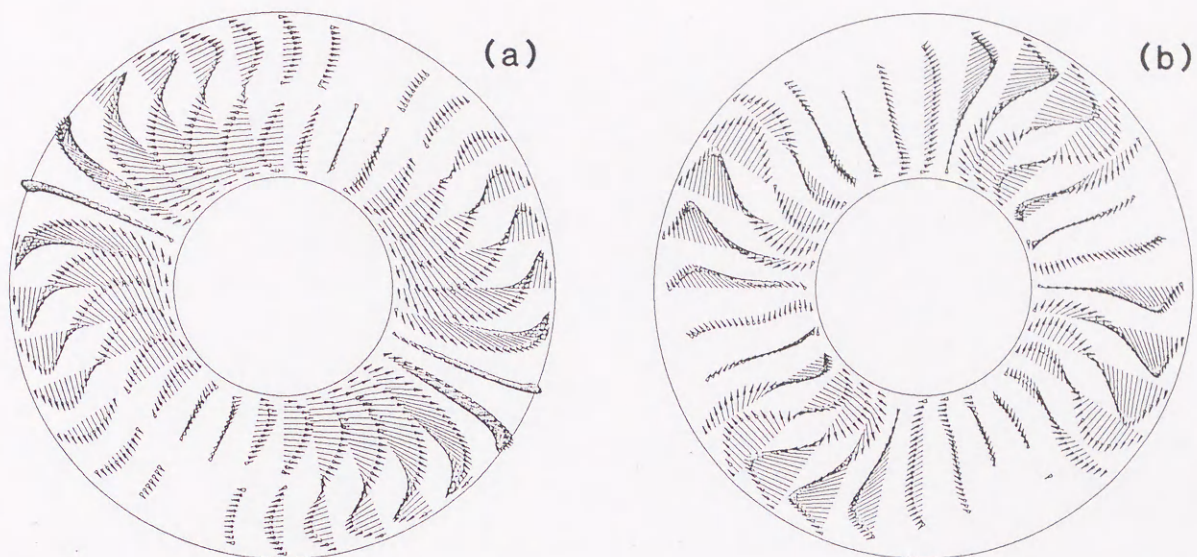


Figure 3.6 Velocity field u in the equatorial plane at $t=0.5$ for Run 1 (a) and Run 2 (b).

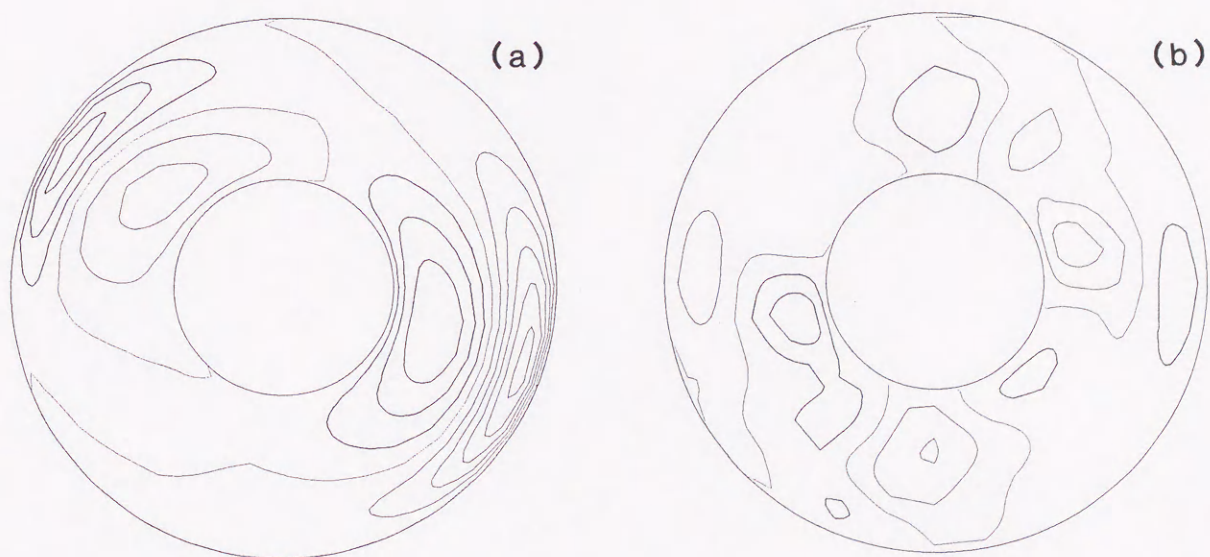


Figure 3.7 Contour plots of $\langle u_\theta \rangle$ at $t=0.5$ for Run 1 (a) and Run 2 (b). The interval between the contour lines is 2.

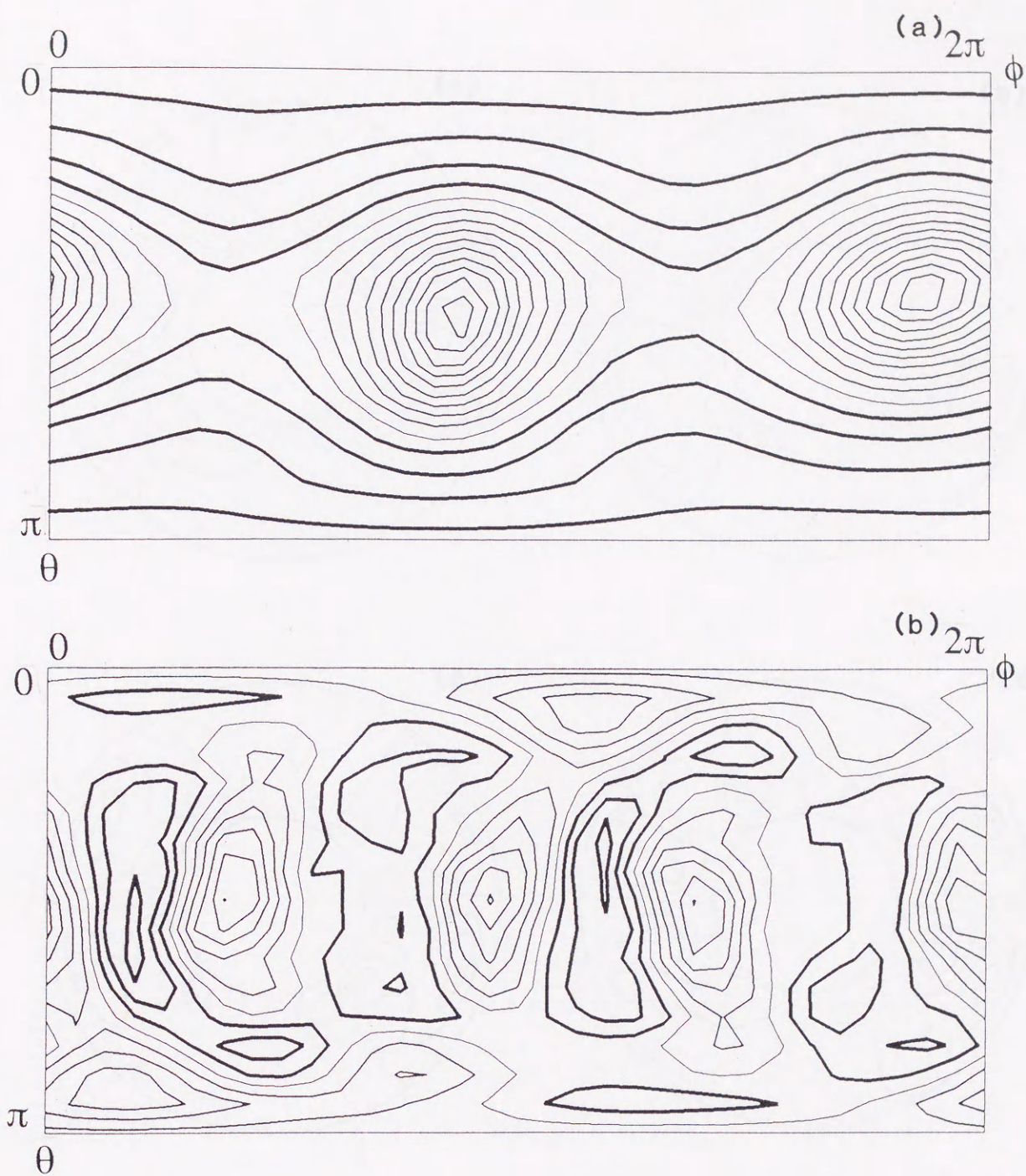


Figure 3.8 Contour plots of $\langle u_r \rangle$ at $t=0.5$ for Run 1 (a) and Run 2 (b) on the spherical surface at $r=0.7$. Thick lines express positive u_r and thin lines negative u_r . The interval between the contour lines is 4.

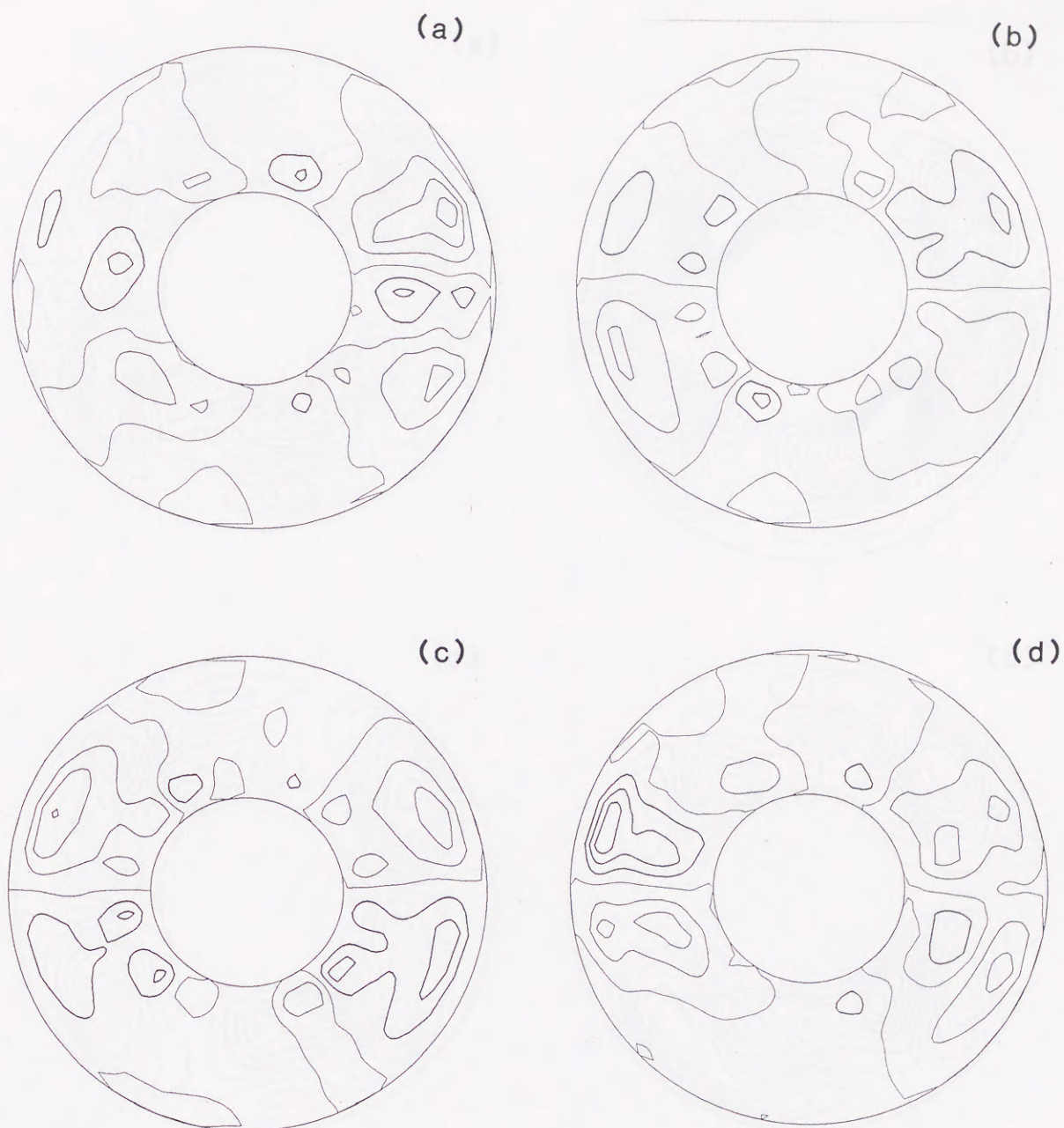


Figure 3.9 Contour plots of h at $t=0.5$ for Run 1 in several meridional planes, $\phi = 0(a), \pi/4(b), \pi/2(c)$ and $3/4\pi(d)$. The interval between the contour lines is 20.

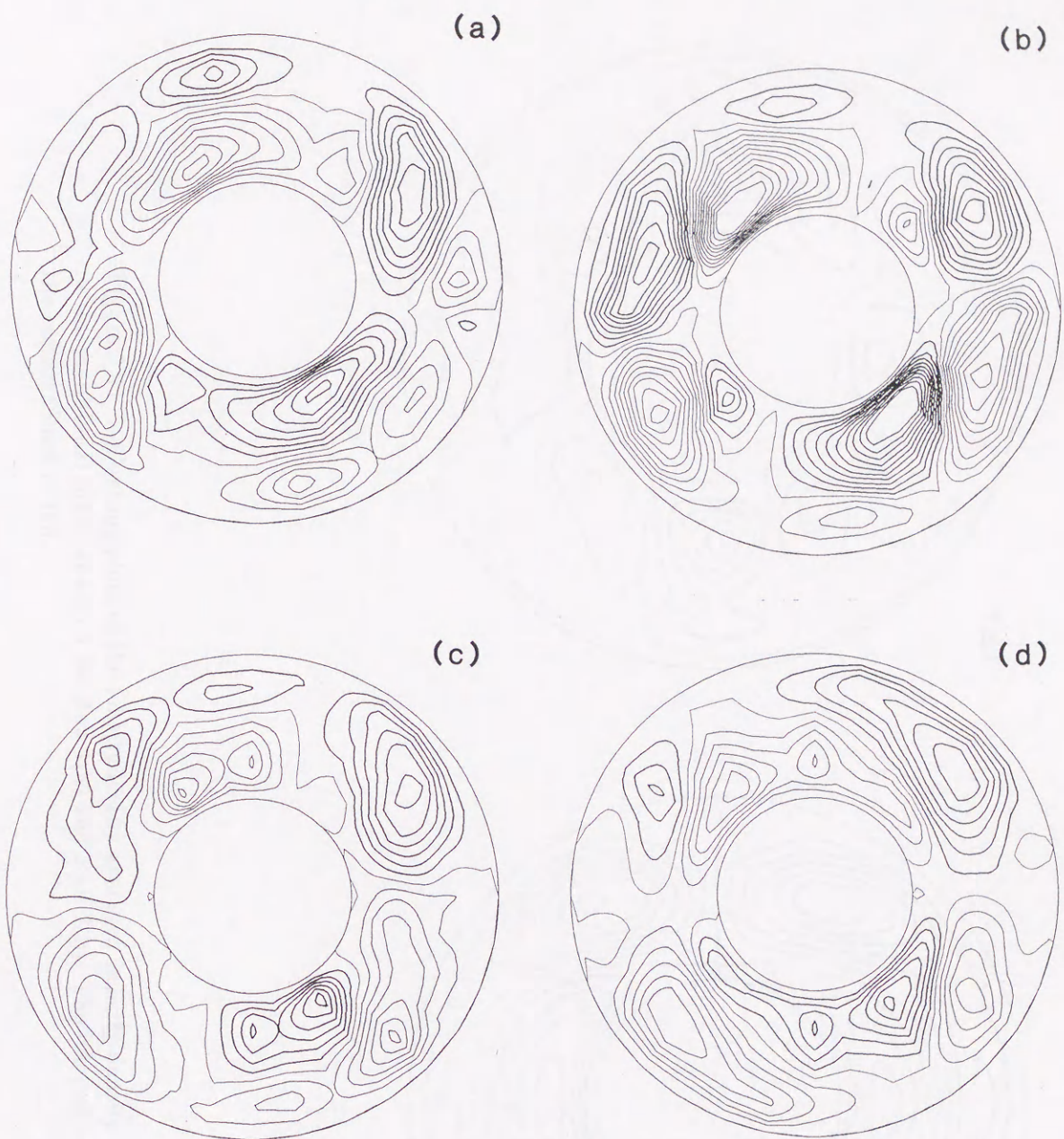
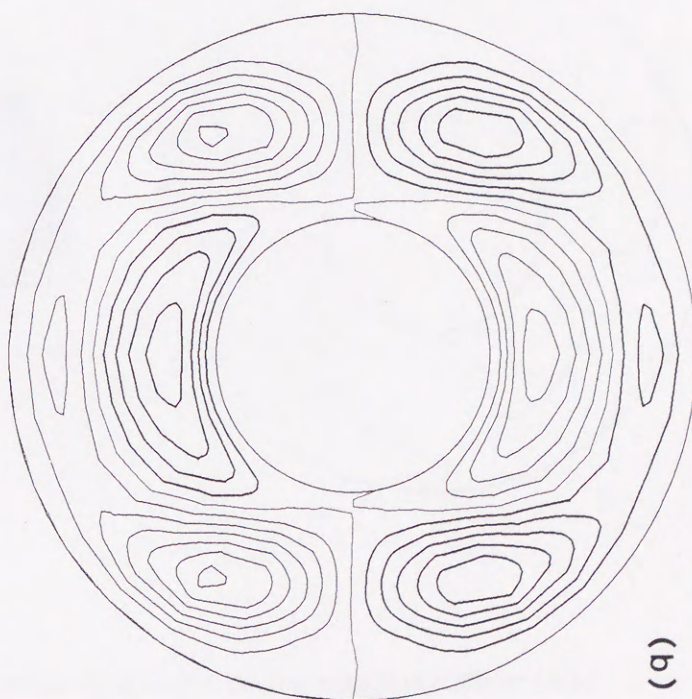


Figure 3.10 Contour plots of h at $t=0.5$ for Run 2. Same conditions as in Fig. 3.9. The interval between the contour lines is 100.



(a)



(b)

Figure 3.11 Contour plots of the longitudinally averaged helicity density $\langle h \rangle$ in the meridional plane at $t=0.5$ for Run 1(a) and Run 2(b). The interval between the contour lines is 100.

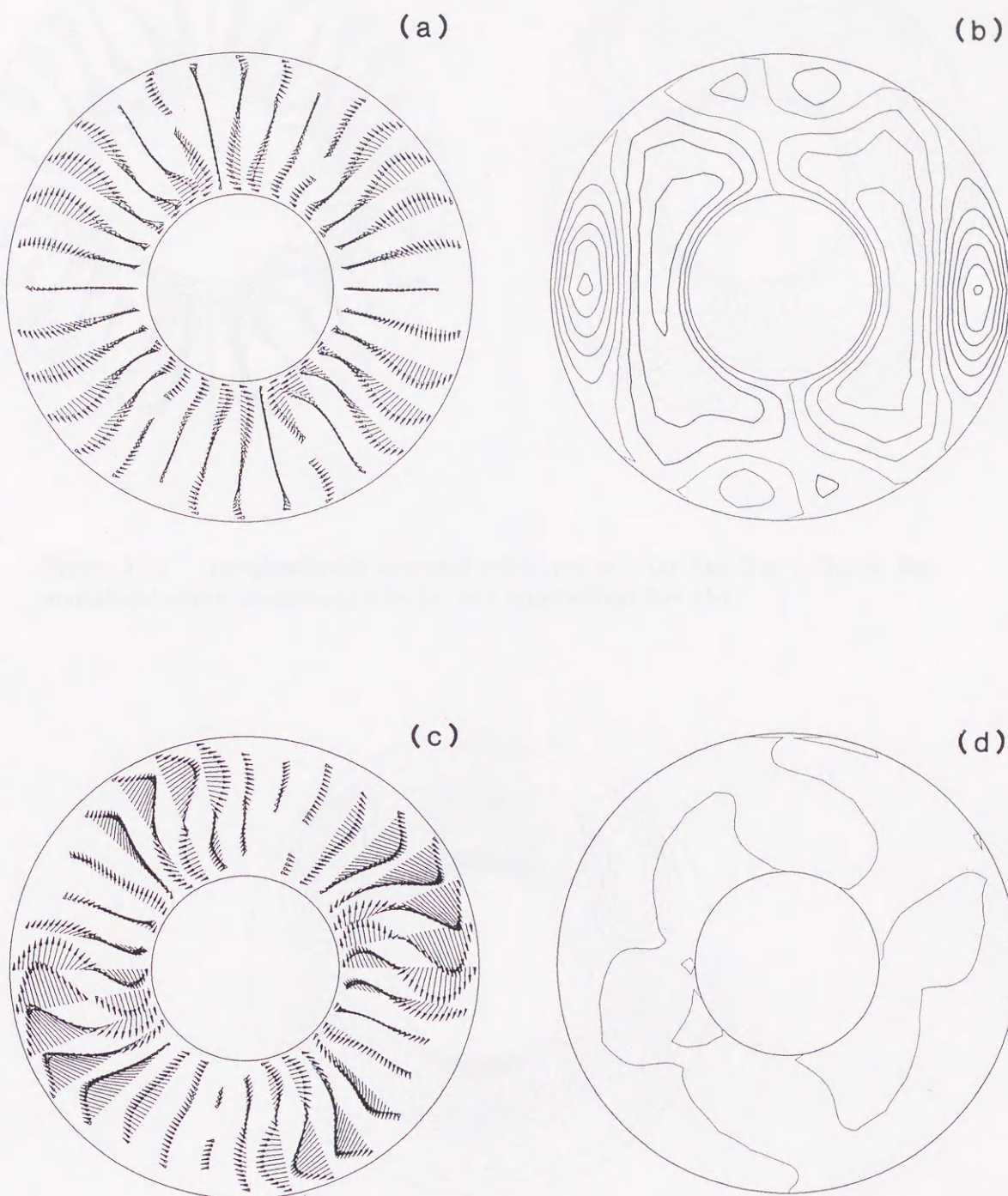


Figure 3.12 Velocity field u for Run 3 at $t=0.4$ on the meridional plane (a,b) and equatorial plane (c,d).

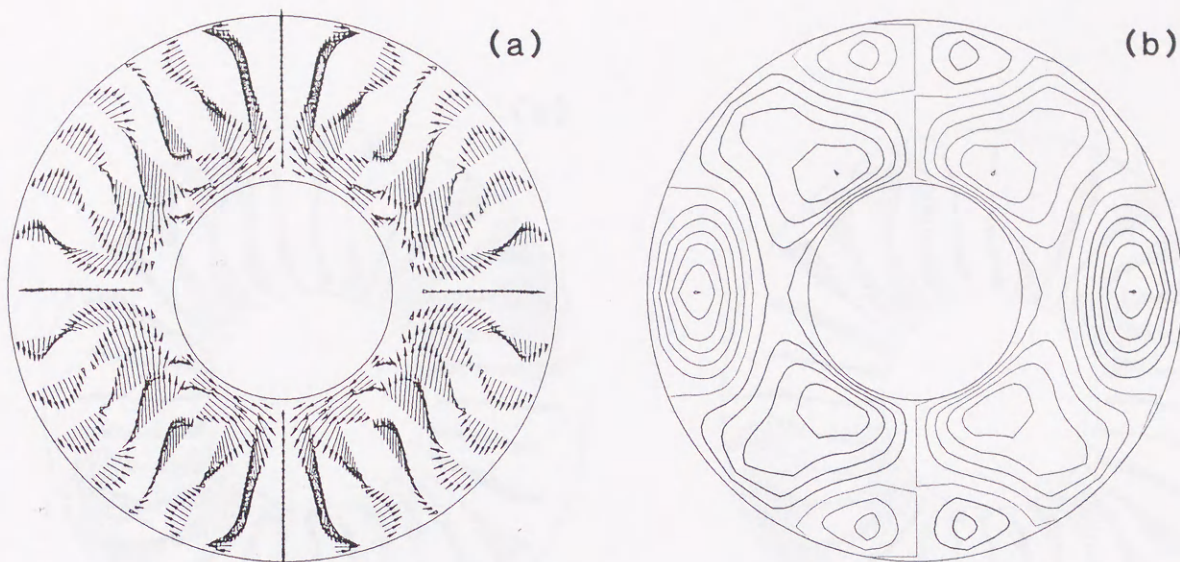


Figure 3.13 Longitudinally averaged velocity $\langle u \rangle$ for Run 3 at $t=0.4$ on the meridional plane; meridional flow (a) and longitudinal flow (b).

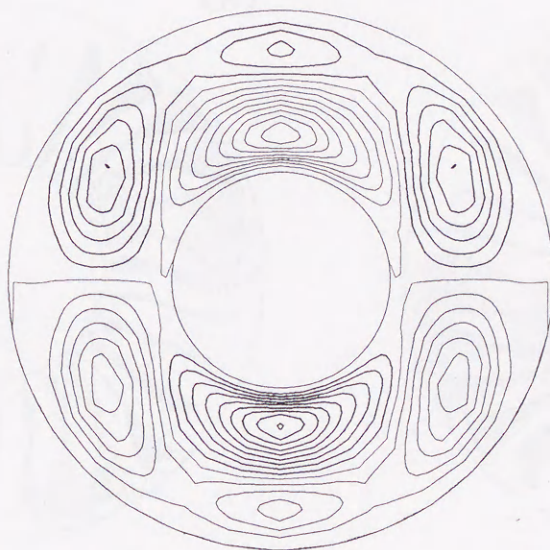


Figure 3.14 Longitudinally averaged helicity density $\langle h \rangle$ for Run 3 at $t=0.4$ on the meridional plane. The interval of the contour lines is 100.

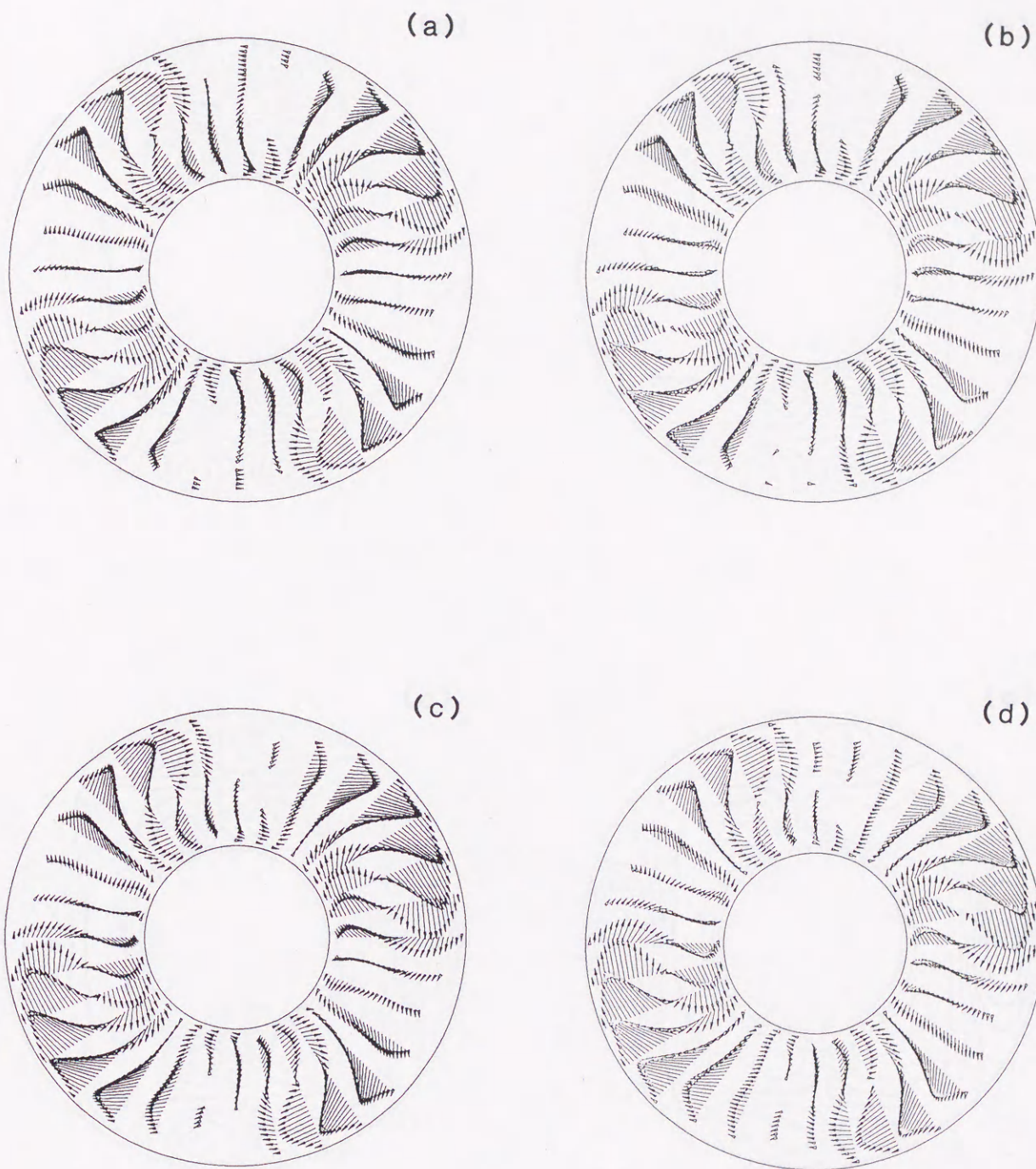


Figure 3.15 Velocity field u for Run 3 on the meridional plane at $\phi = 0$ at $t=0.36$ (a), 0.37 (b), 0.38 (c) and 0.39 (d).

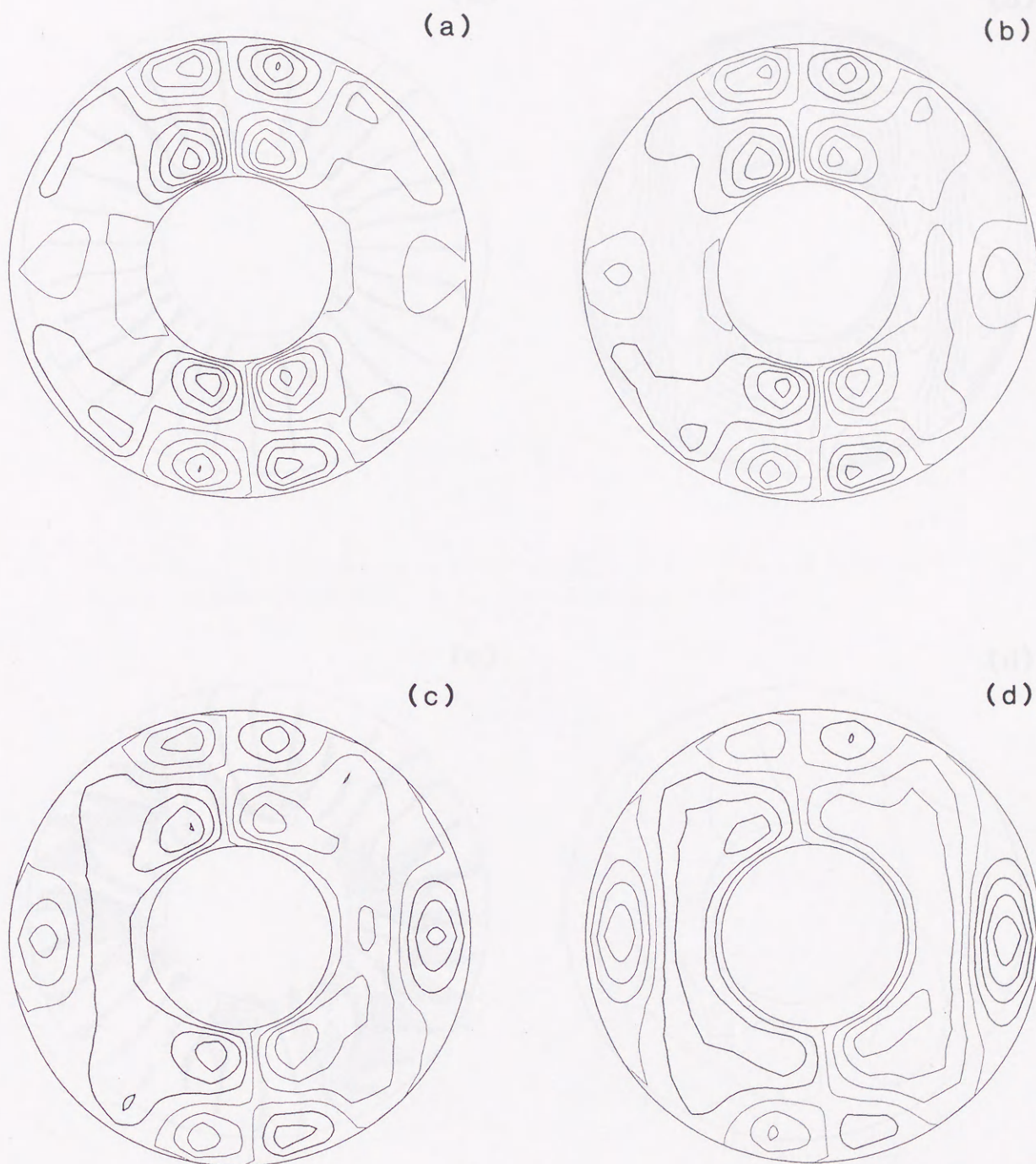


Figure 3.16 Contour plots of $\langle u_\phi \rangle$ for Run 3 on the meridional plane at $\phi = 0$ at $t=0.36$ (a), 0.37 (b), 0.38 (c) and 0.39 (d).

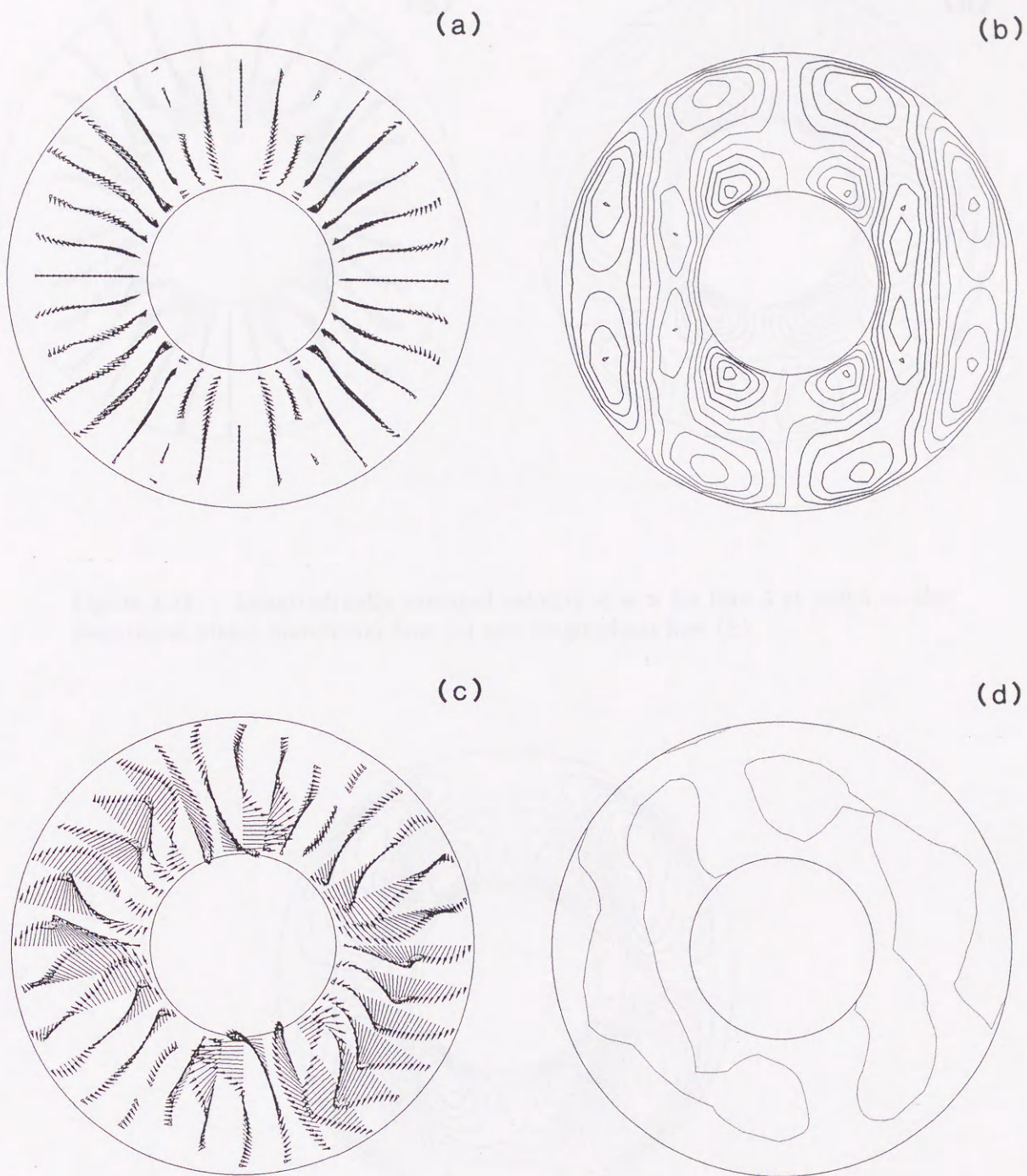


Figure 3.17 Velocity field u for Run 4 at $t=0.5$ on the meridional plane (a,b) and equatorial plane (c,d). The interval of the contour lines is 1.

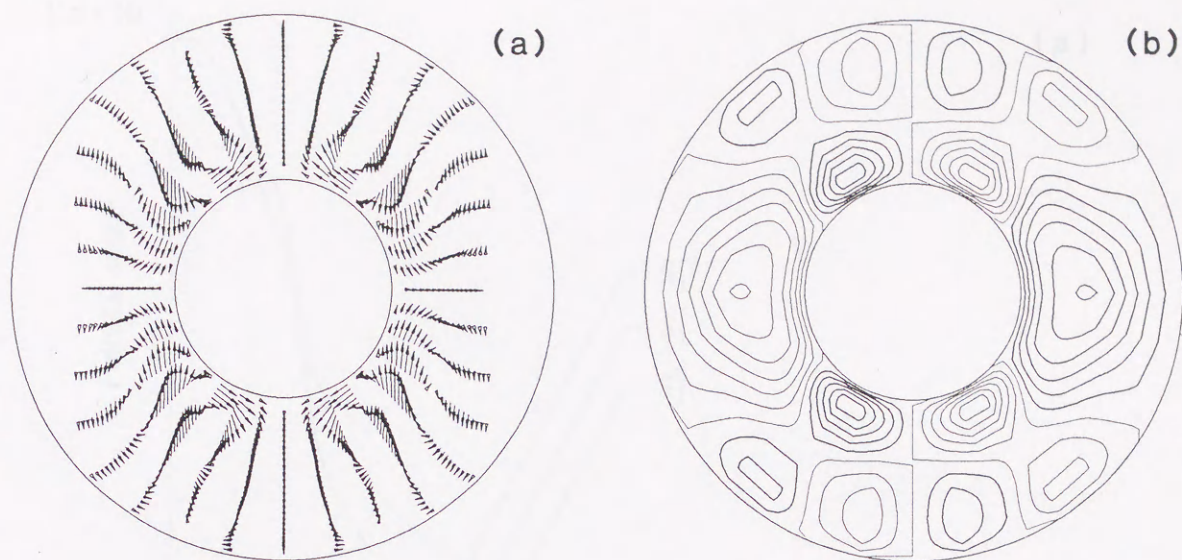


Figure 3.18 Longitudinally averaged velocity $\langle u \rangle$ for Run 5 at $t=0.5$ on the meridional plane; meridional flow (a) and longitudinal flow (b).

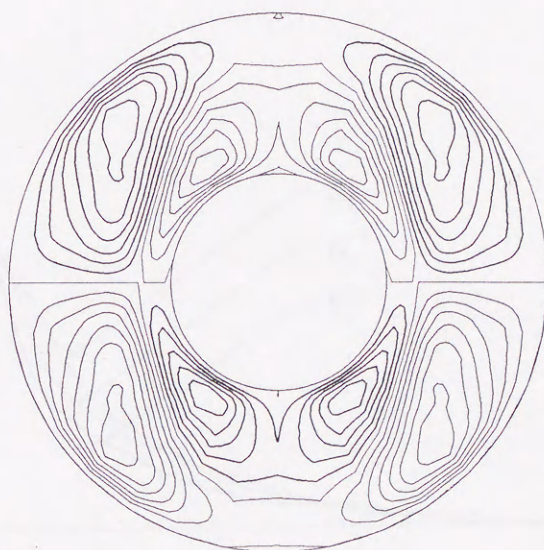


Figure 3.19 Longitudinally averaged helicity density $\langle h \rangle$ for Run 4 at $t=0.5$ on the meridional plane. The interval of the contour lines is 20.

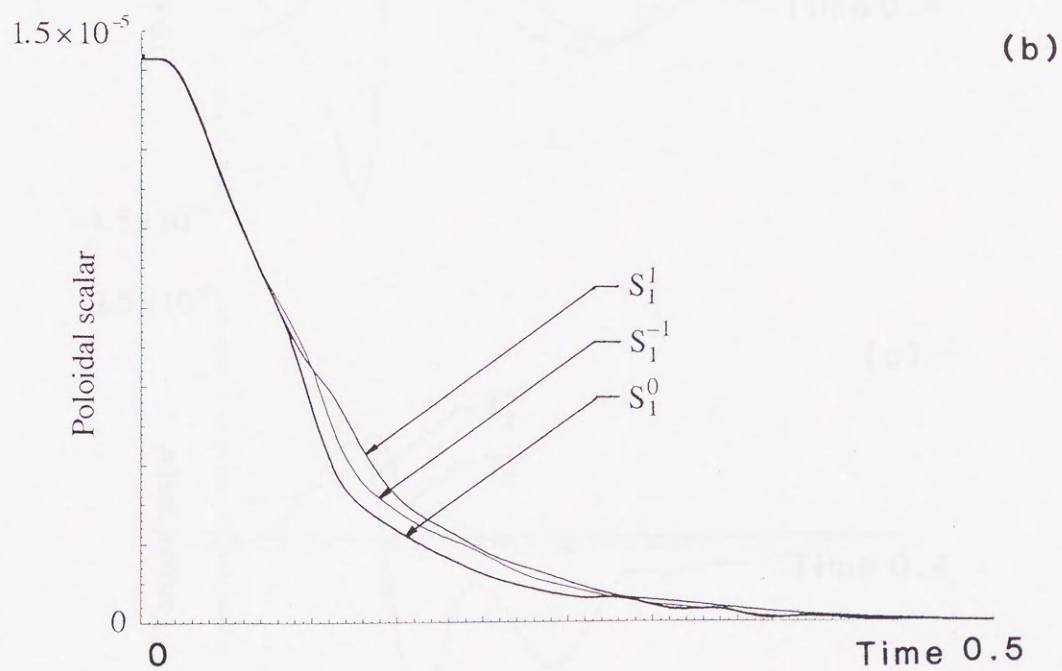
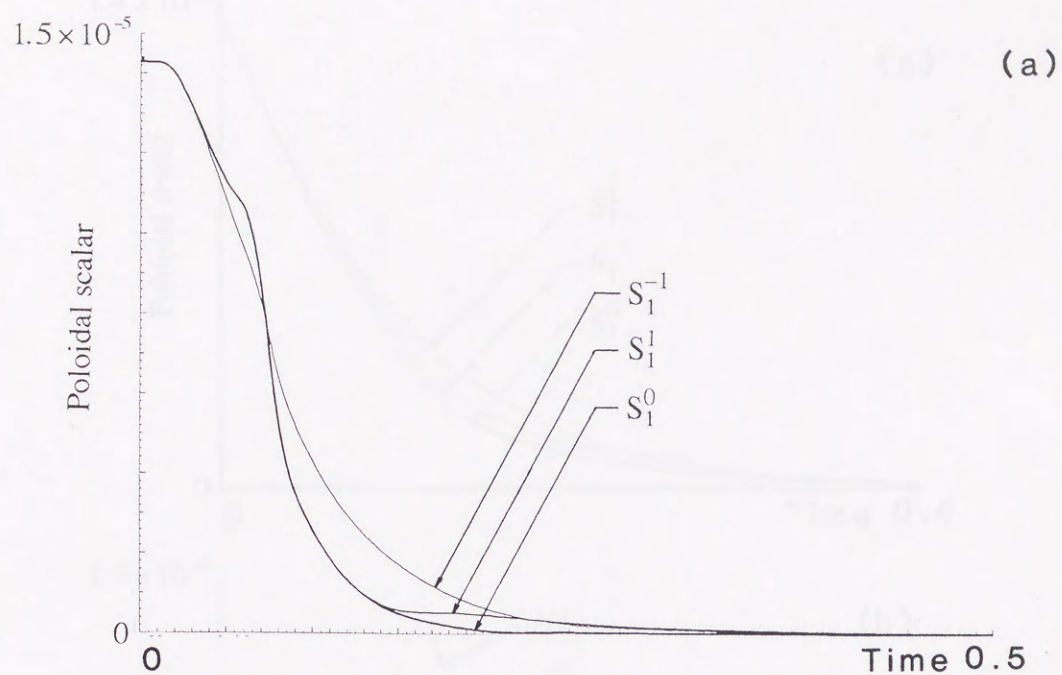


Figure 3.20 Time evolution of the poloidal scalar functions S_{M1}^0 , S_{M1}^1 , and S_{M1}^{-1} on the spherical surface $r = 0.7$ for Run 1(a) and Run 2(b).

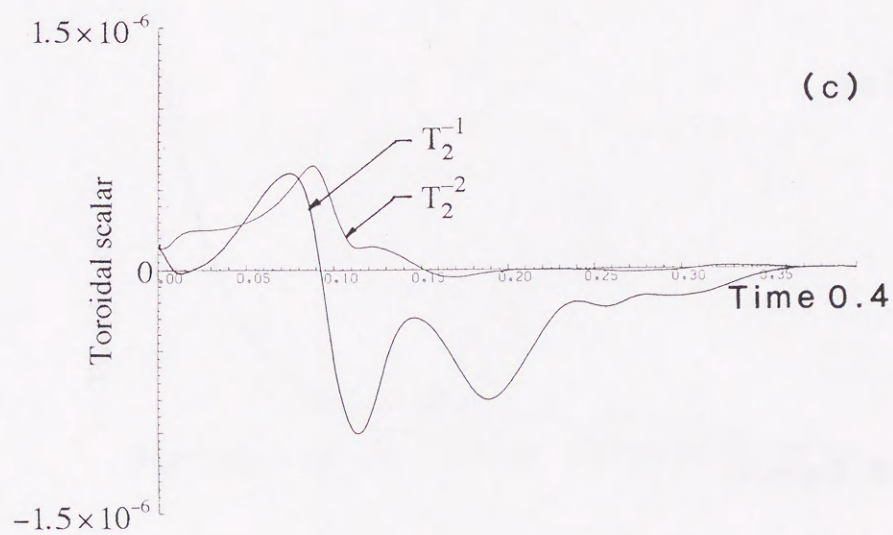
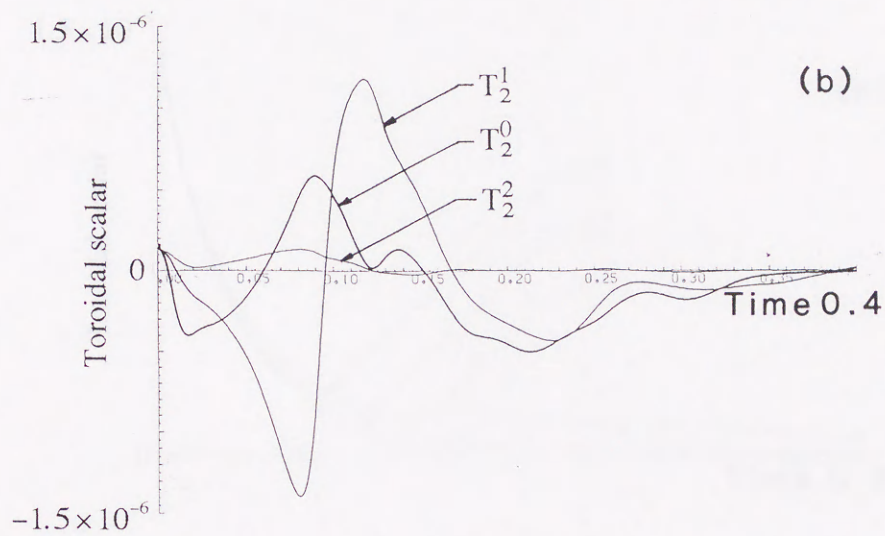
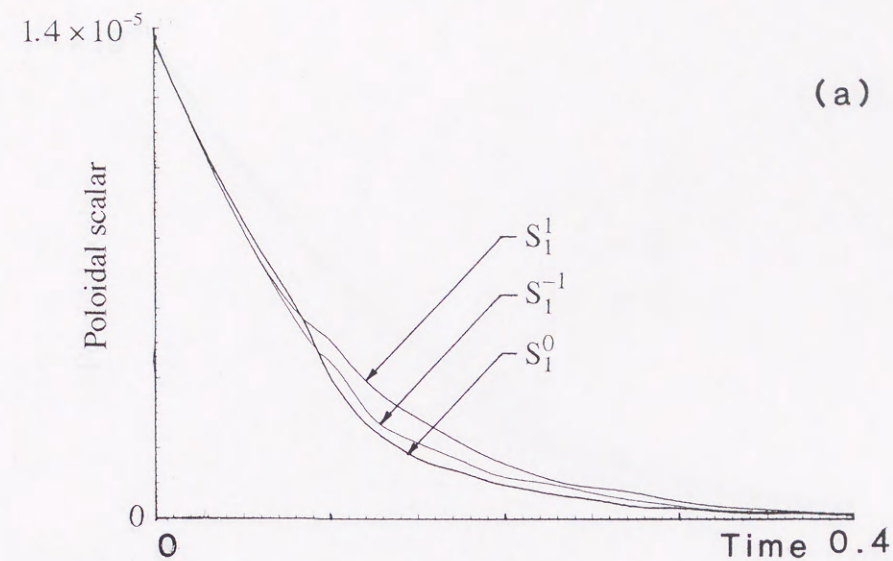


Figure 3.21 Time evolution of the poloidal (a) and toroidal (b),(c) scalar functions on the spherical surface $r = 0.7$ for Run 3.

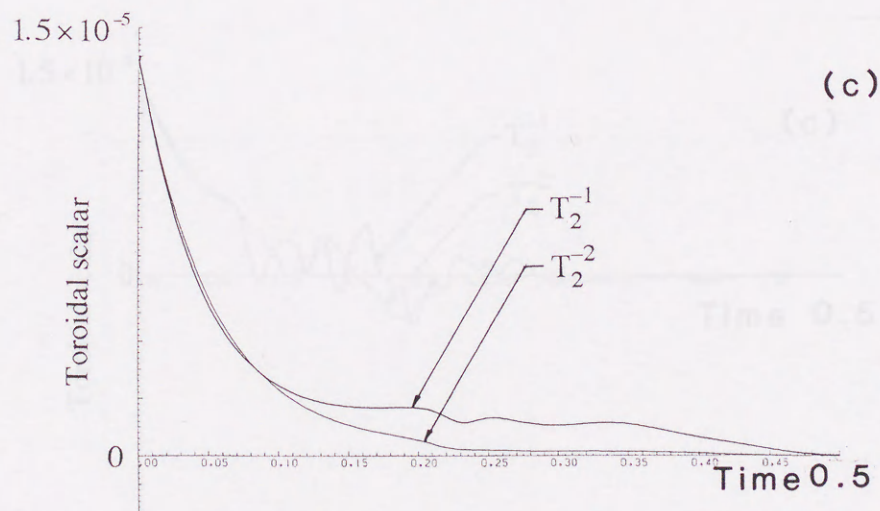
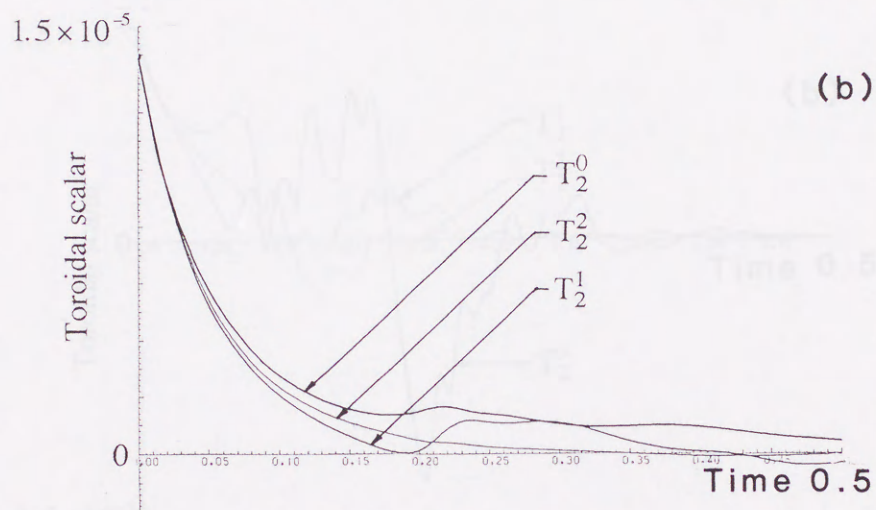
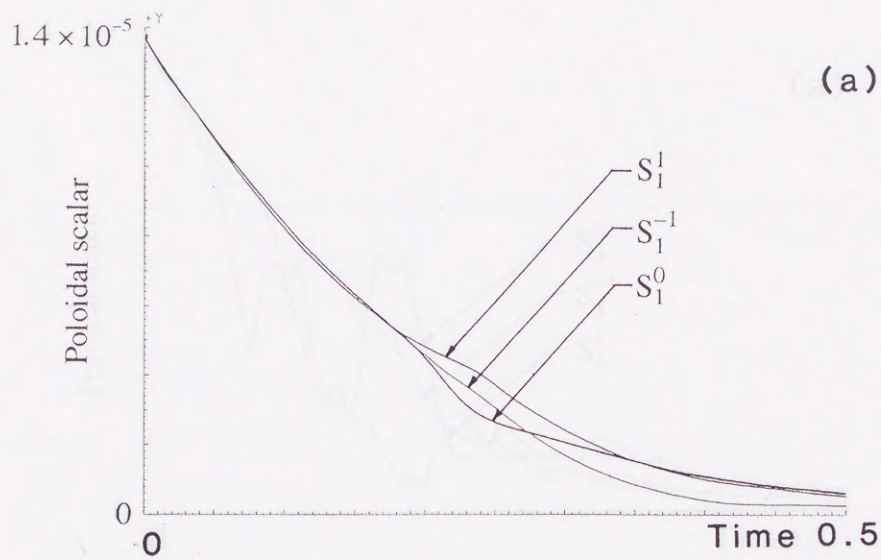


Figure 3.22 Time evolution of the poloidal (a) and toroidal (b),(c) scalar functions on the spherical surface $r = 0.7$ for Run 4.

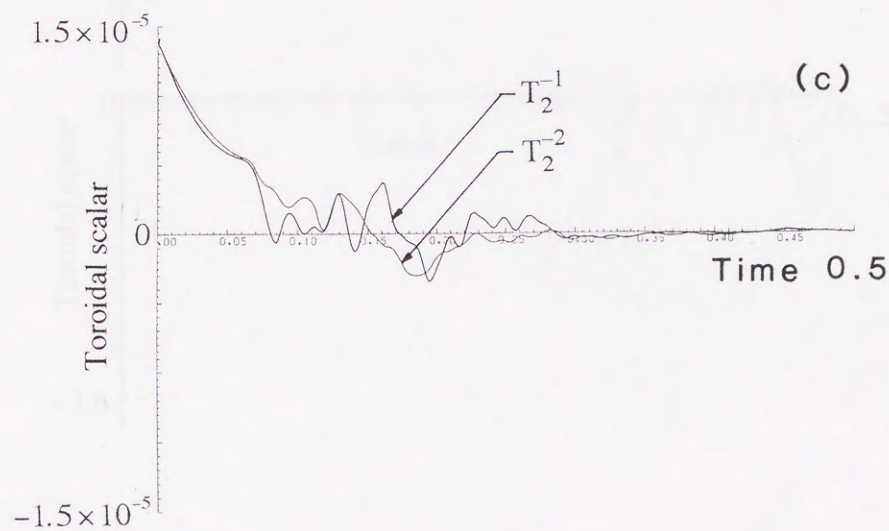
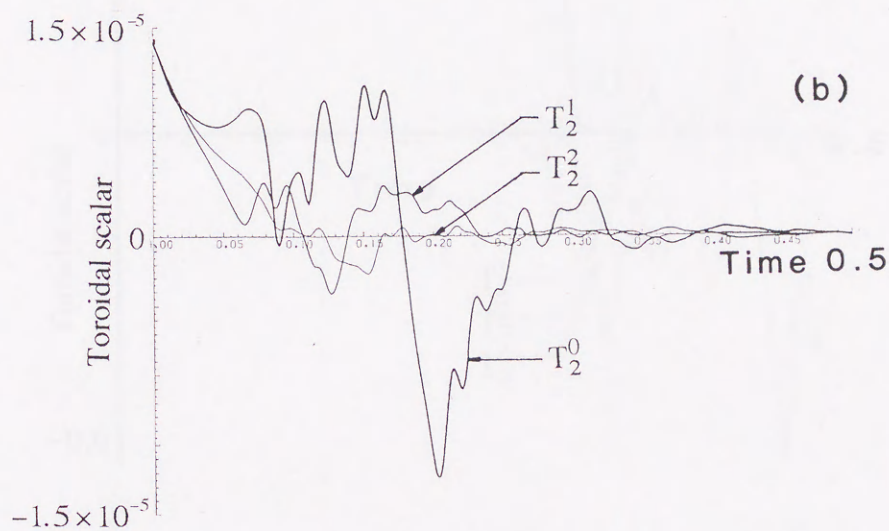
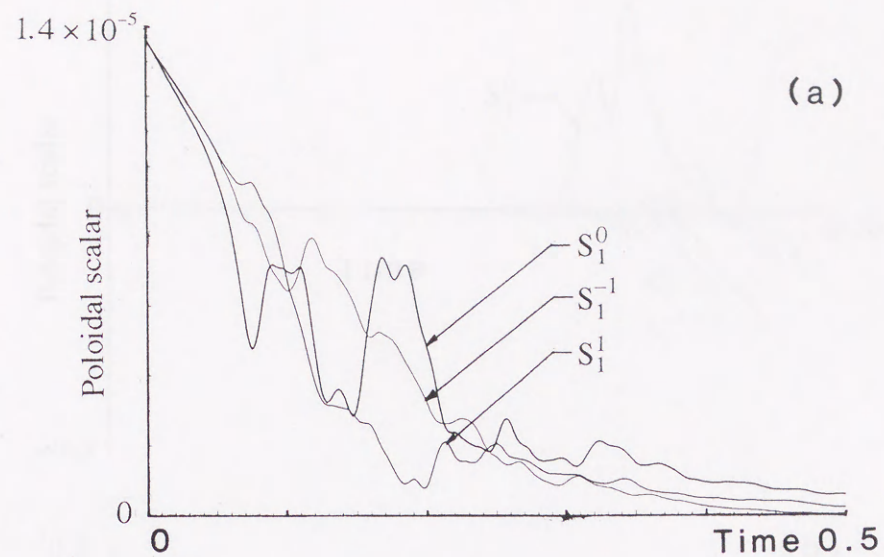


Figure 3.23 Time evolution of the poloidal (a) and toroidal (b),(c) scalar functions on the spherical surface $r = 0.7$ for Run 5.

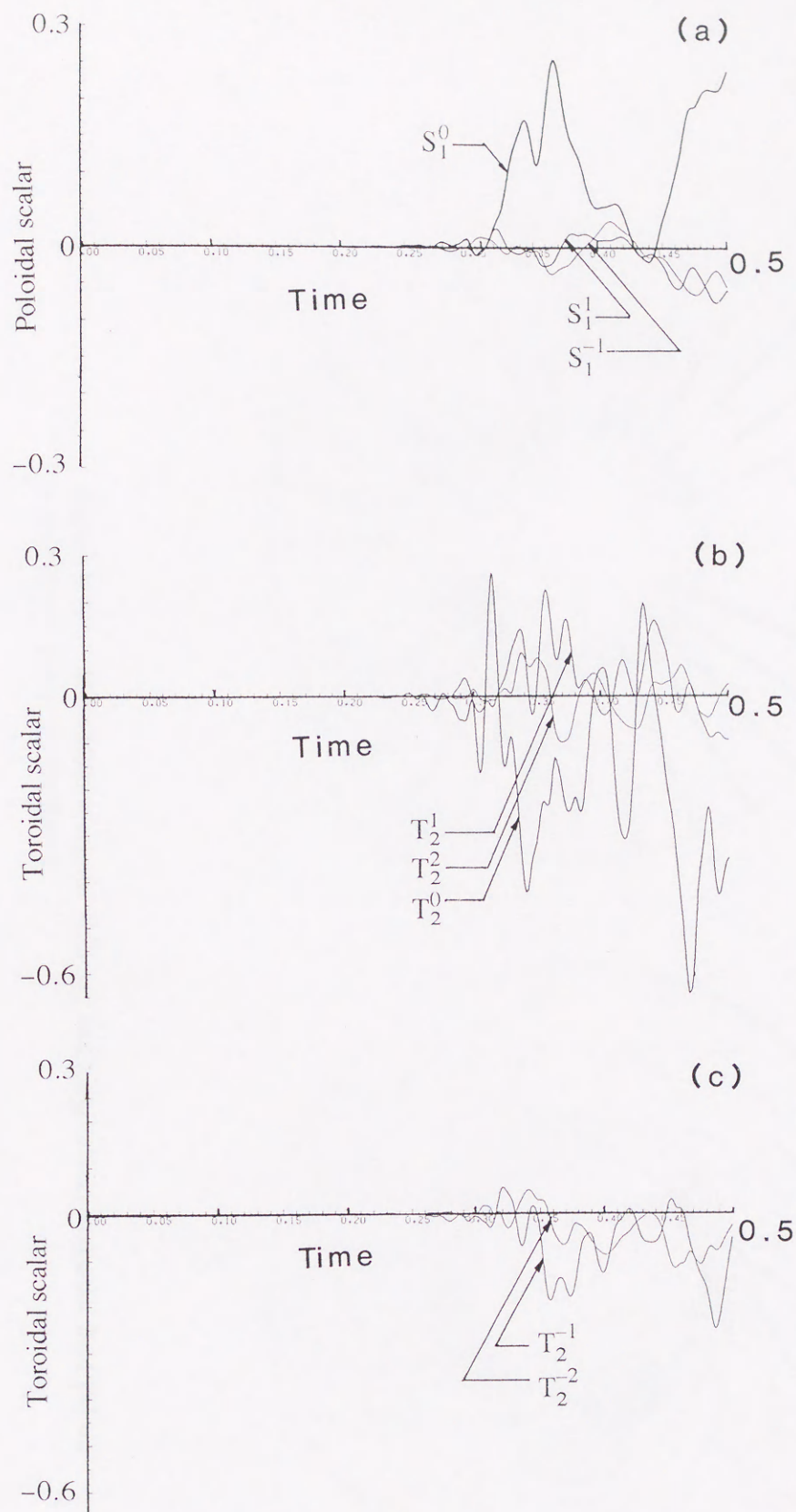
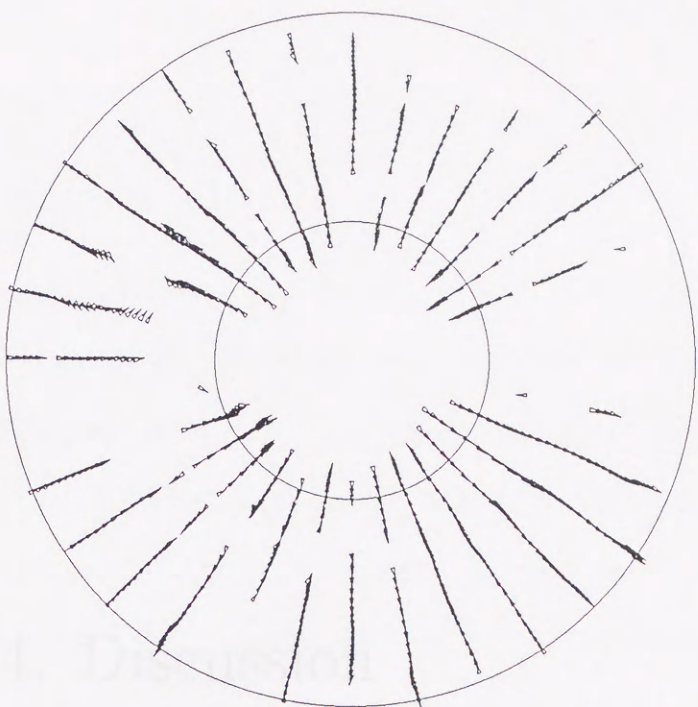


Figure 3.24 Time evolution of the poloidal (a) and toroidal (b),(c) scalar functions on the spherical surface $r = 0.7$ for Run 6.



(a)



(b)

Figure 3.25 Meridional magnetic field (a) and longitudinal magnetic field (b) on a meridional plane (a) for Run 6.

4 Discussion

4.1 Check for the boundary effects

The results of the present simulation have shown that the velocity field contains the helical motion as essential part; and the convective rolls whose axes are approximately parallel to the rotation axis of the system are raised. The longitudinal scale of the convective motion is small compared with that in the non-rotating case. When the effect of rotation is dominant, the fluid motion is almost symmetric with respect to the equatorial plane. The magnitude of the helicity density h is much larger than that in the non-rotating case. On the average, in the north hemisphere h is positive in the region out of the cylindrical surface which is adjoining the inner boundary and negative within the cylindrical surface. In addition, the convective pattern shows the westward drift.

The fluid motion which shows these features is supposed to be a candidate for the magnetic field generation. Though it is expected that the large-scale helical motion which has been obtained in the present model generates the magnetic field, the regeneration process of the magnetic field does not occur straightforward. Especially the magnetic field does not grow for the moderate value of the magnetic Prandtl number P_{rM} . Although the magnetic energy makes growth when P_{rM} is increased i.e. the magnetic diffusivity is decreased, the obtained magnetic field is rather spiky and intermittent including the relatively large amplitude in the spherical harmonics with high degree. This spatial property of the obtained magnetic field is not relevant to the geomagnetic field in which the dipole component is dominant. In addition, the magnetic diffusivity λ is supposed to be much

larger than the kinematic viscosity ν and the thermal diffusivity κ in the Earth's outer core (Gubbins and Roberts, 1987). Therefore, adopting the small value of λ compared to those of ν and κ is not appropriate to the geodynamo problem.

In the present model, a treatment for the magnetic field in the interior of the shell is provided; the magnetic field near the origin ($r = 0$) is decreased exponentially by multiplying \mathbf{B} by a function $G(r)$ given in Eq. (3.68). This treatment is introduced in order to avoid a numerical instability which occurs in the vicinity of the origin. Although we considered that this treatment possesses only minor effect on the magnetic field generation which takes place in the shell, the magnetic diffusion by this treatment might be rather large. To study the effect of this treatment on the magnetic field generation, we perform another computational run in which the interior of the shell is assumed to be a very high conducting material. We here describe the model in which the conducting fluid is adjoining a perfect conductor at the inner boundary. First, the boundary condition of \mathbf{B} at the inner boundary is presented.

On a spherical surface adjoining a perfect conductor,

$$B_r = 0, \quad (4.1)$$

$$E_\theta = E_\phi = 0. \quad (4.2)$$

From the Ohm's law ($\mathbf{J} = \sigma(\mathbf{E} + \mathbf{u} \times \mathbf{B})$) and the conditions (4.2) and ($\mathbf{u} = 0$ at the inner and outer boundaries), we have

$$J_\theta = J_\phi = 0, \quad (4.3)$$

Then, it follows from the equation of continuity for \mathbf{J}

$$\frac{\partial}{\partial r} (r^2 J_r) = 0. \quad (4.4)$$

These conditions for B_r and \mathbf{J} provide the condition for T_{Ml}^m and S_{Ml}^m on a spherical boundary adjoining a perfect conductor, that is,

$$\frac{\partial T_{Ml}^m}{\partial r} = 0, \quad S_{Ml}^m = 0, \quad \frac{\partial^2 S_{Ml}^m}{\partial r^2} = 0. \quad (4.5)$$

Thus, the boundary condition for T_{Ml}^m and S_{Ml}^m is obtained. In this model, it is not necessary to solve the equation of magnetic diffusion in the interior of the shell. The time variation of the toroidal and poloidal scalars referred in Section 3.4 is shown in Fig. 4.1. Time evolution of these scalars is similar to that of Run 3 in Section 3.4. The toroidal and poloidal scalars eventually vanish though the toroidal scalars exhibit complicated temporal behavior during the evolution process. Hence, lack of the regeneration process of the magnetic field in the present model is not attributed to the treatment for \mathbf{B} in the interior across the boundary.

4.2 Necessity of small-scale dynamo

The present model is a large-scale, laminar dynamo model where the interaction between the large-scale motion and large-scale magnetic field generates the large-scale magnetic field as in Bullard-Gellman (1954).

For the ineffective generation of the magnetic field in the large scale dynamo, we consider that the insufficiency of the α -effect results in ineffective generations of the magnetic field case for the moderate magnetic Prandtl number. As shown in Figs. 3.21 and 4.1, the temporal variation of the toroidal scalars are remarked and the amplitude of the toroidal scalars takes the rather large value compared with their initial value during the evolution process. On the other hand, the poloidal scalars decrease almost monotonically. These temporal behavior of the toroidal and poloidal scalars suggests that the generation

mechanism of the poloidal field is inadequate in the present model. It is needed to incorporate the effect of the small-scale motion with the present model.

4.3 Possible direction for future studies

As described in Section 1, there are other models which include the small-scale motion and magnetic field. For example, in the Parker's $\alpha\omega$ -dynamo (Parker, 1955), the toroidal magnetic field is generated from the poloidal field by the differential rotation which is a large-scale motion, while the poloidal magnetic field is created from the toroidal field by the ensemble of the small-scale motions called cyclones. Namely, the ω -effect is caused by the large-scale motion, while the α -effect is caused by the small-scale motion. In this context, the results of the present studies for the plane boundary show quite interesting suggestion. By existence of the helical motion of the fluid the sufficient growth of the magnetic field is taking place. The interesting point is that we can use the plane boundary model of the present studies given in Section 2 as local solution to understand the small unit of eddies, cells and rolls.

One way to include the effect of the small-scale phenomena in the numerical simulation is to solve the basic equation directly using a fine mesh with a large number of spatial grid points. Although this method is desirable because of its simplicity of the algorithm, the feasible problem is strongly restricted by the ability of the computer. In particular, in the celestial dynamo problem the non-dimensional parameter which characterize the fluid motion such as the Reynolds number and the Rayleigh number, often takes a quite large value due to the large scale of the celestial body. We should say, therefore, the direct simulation of the small-scale dynamo process is quite impossible.

Another way to incorporate the effect of the small-scale phenomena with the simulation

is turbulence modeling. Among the various methods using turbulence model, Large-Eddy-Simulation (LES) is one of the most powerful method to treat turbulence. In LES, only the subgrid-scale quantities is modeled and expressed by the grid-scale quantities. The basic equation for the grid-scale quantities are numerically solved. The LES has been extensively performed in the study of hydrodynamic (non-magnetic) turbulence (Deardorff, 1970 ; Moin and Kim, 1982). Recently, the LES of the reversed field pinches has been carried out by using a MHD turbulence model (Yoshizawa and Hamba, 1988a ; Hamba, 1989). Reversed field pinches is a method to confine plasma in the fusion reactor and possesses common physical nature with planetary dynamo (Yoshizawa, 1990). It has been shown that the turbulence model improves the profile of B_θ . In the planetary and stellar dynamo problem, Glatzmaier (1985a,b) has included the eddy diffusivity in his simulation using the Smagorinsky model though turbulence modeling of the α -effect has not been carried out.

Although it is not clear whether convection in the Earth's outer core is in turbulent state or not, it is reasonable to assume the existence of the small-scale motion, considering the large Reynolds number of the fluid motion. Therefore, the LES of the geodynamo process is required to treat the small-scale α -effect and the eddy diffusivity. We consider that the present studies for the local solution and the large scale dynamo have shown the necessity of the inclusion of the small scale processes together with large scale processes to have the real solution for the origin of the geodynamo. The detail studies in this direction are deferred for future studies.

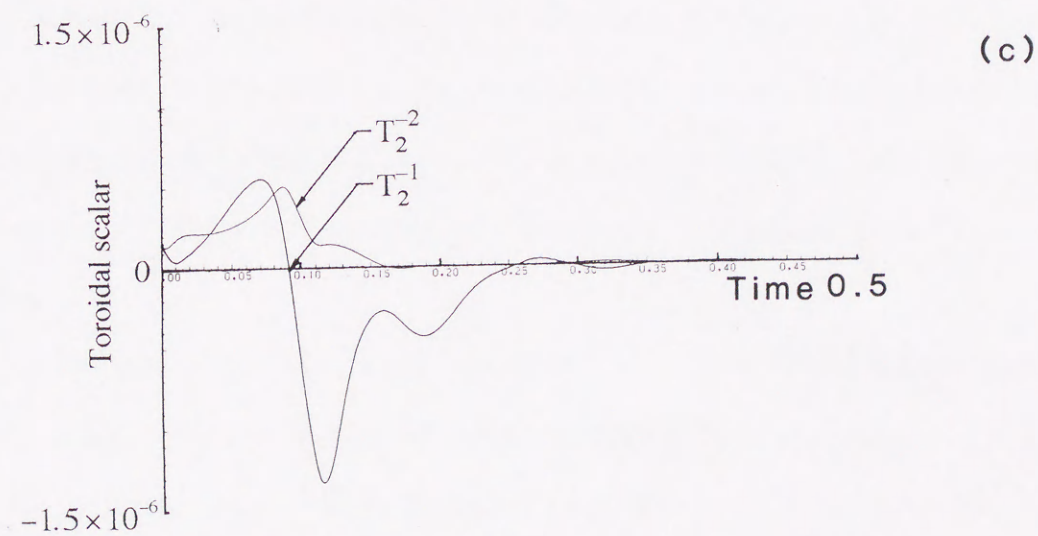
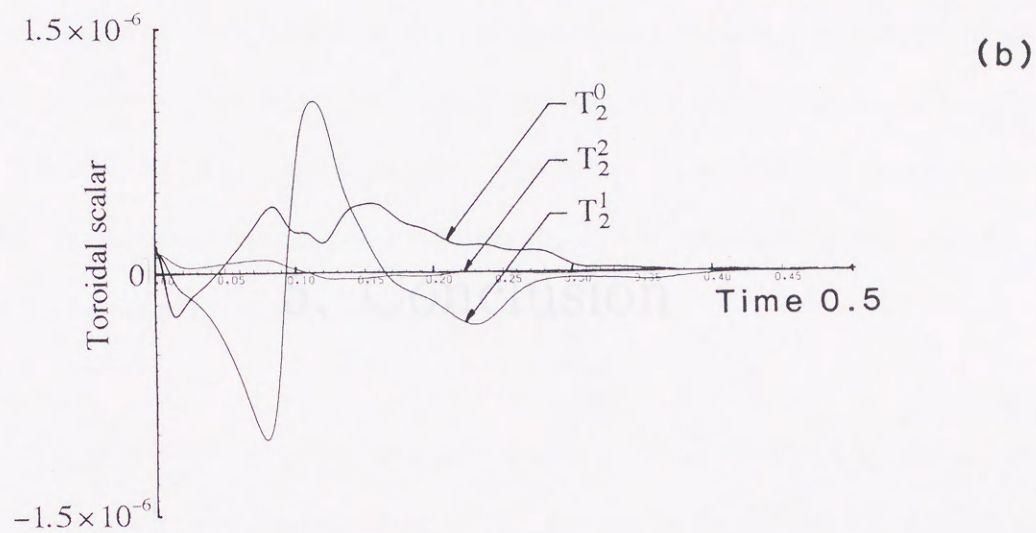
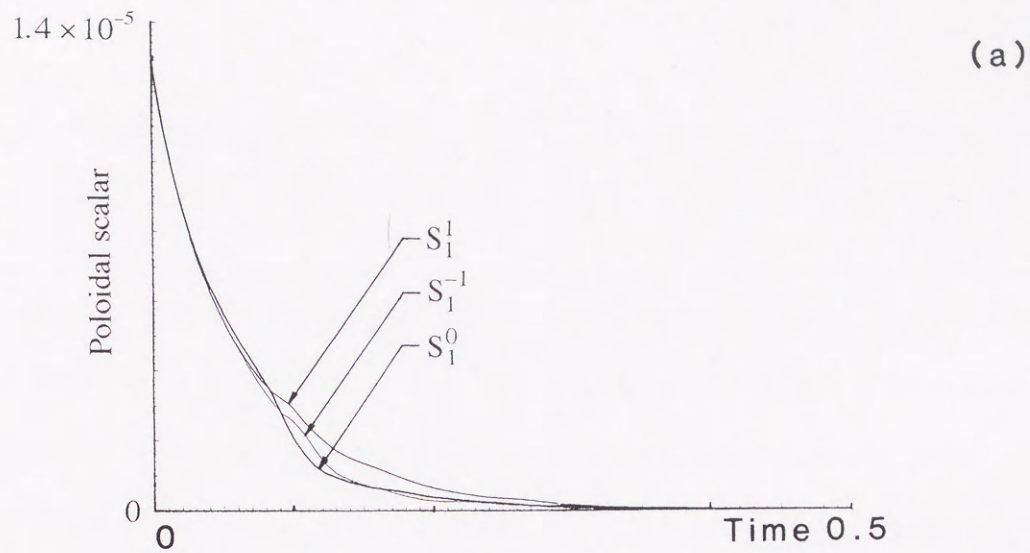


Figure 4.1 Time evolution of the poloidal (a) and toroidal (b),(c) scalar functions on the spherical surface $r = 0.7$.

5 Conclusion

Numerical simulations of magnetoconvection have been performed to study the effect of rotation of the system on convection and magnetic field generation. The equations of motion, electromagnetic induction and heat conduction are simultaneously solved within the Boussinesq approximation. We have considered two models, i.e. a plane boundary model and a spherical shell model. Both models are large-scale dynamo model in which the interaction between the large-scale motion and magnetic field generates the large-scale magnetic field. The plane boundary model is however understood also as local solution that reflects the elementary processes when we take the boundary as non-realistic one that is set up to make the system simple.

First, we have studied the plane boundary model to clarify the effect of rotation under simple condition. The Rayleigh numbers of the simulation are several times larger than the critical value. The spatial derivative in the horizontal direction is calculated by the pseudospectral method with Fourier series expansion. The spatial derivative in the vertical direction is obtained by the second-order finite difference method. Time integration is performed by the improved Euler method. The results of the plane boundary model are as follows.

i) When the convective velocity is small, the distribution of the kinetic helicity density $h = \mathbf{u} \cdot \nabla \times \mathbf{u}$ is anti-symmetric with respect to the central, horizontal plane at $z = 0$ as predicted by the linear theory. When the velocity becomes large, however, the distribution of h changes into the roughly symmetric one due to the advection effect of the fluid motion.

ii) The studies of this part are concentrated on a part of the kinetic helicity density, $h_z = (u_z \omega_z)$ which becomes a good indicator of the rotation effect. The temporal change of the distribution of h_z from anti-symmetric one with respect to the central plane $x = 0$ into the approximately symmetric one has been clearly shown as the result of the advection. To study the effect of the advection on the distribution of h quantitatively, the equation for ω_z is considered. It has been shown that the transporting term makes the distribution of h_z the approximately symmetric one when the convective velocity becomes large.

iii) The effect of rotation on the convective pattern has been presented by the several computational runs with various Taylor numbers. The helical flow due to the Coriolis force has been clearly shown. We have present values of quantity, $\int |h_z| dV / (u_{rms} \omega_{rms})$ which is a good index of the rotation effect.

iv) The effect of rotation on the magnetic field generation has been clarified by comparing the result for rotating case with that for non-rotating case, though the ratio of the magnetic energy increment to the initial value is only matter of factor.

v) The geometrical relation between \mathbf{u} and \mathbf{B} vectors has been investigated in terms of the distribution of $\cos \theta (= \mathbf{u} \cdot \mathbf{B} / (|\mathbf{u}| |\mathbf{B}|))$. The difference between the distribution of $\cos \theta$ for the rotating case and that for the non-rotating case is apparent. In the rotating case, the distribution of $\cos \theta$ is approximately uniform, leading to the magnetic field generation via the induction term $\nabla \times (\mathbf{u} \times \mathbf{B})$.

In the second part of this study, we have considered the case of a model planet. The dynamics of the conducting fluid in a rotating spherical shell in the interior of a model planet is investigated for the generation processes of the helical motion and magnetic field

relating to the understanding of the geodynamo process. The spatial derivative in the vertical (radial) direction is obtained by the second-order finite difference method. The spatial derivative in the horizontal direction is obtained by the pseudospectral method with spherical harmonic expansion. Time integration is performed by the improved Euler method.

The obtained velocity field for the rotating case shows the characteristic flows of convection in a rotating spherical shell, that is,

- i) The convective rolls whose axes are approximately parallel to the rotation axis of the shell are generated. The longitudinal scale of the rolls is small compared with that of the non-rotating case.
- ii) When the effect of rotation becomes dominant, the convective motion changed to symmetric one with respect to the equatorial plane. Therefore, the fluid motion which crosses the equatorial plane is very small.
- iii) The axisymmetric part of the longitudinal motion, i.e. differential rotation is strong and the axisymmetric part of the meridional motion, i.e. meridional circulation is weak compared with those of the non-rotating case.
- iv) The generated convective rolls drift westward.
- v) The magnitude of the kinetic helicity density is much larger than that of the non-rotating case.
- vi) On the average, in the northern hemisphere the kinetic helicity is negative out of the cylindrical surface adjoining the inner boundary and positive within the cylindrical surface. All the signs of the kinetic helicity are changed in southern hemisphere compared with those in the northern hemisphere.

The obtained velocity field with helical motion shows properties to be candidate for the origin of magnetic field when we infer from the elemental processes based on the plane boundary case. However, the regenerative process does not occur for the moderate value of the magnetic Prandtl number. We consider that the α -effect, which is essential to generate the poloidal magnetic field from the toroidal field, is insufficient in the present large-scale model. The detailed investigation of the present study suggests that the model which includes the effect of the small-scale phenomena is necessary to simulate more realistic geodynamo process. In particular, it becomes more apparent that the Large-Eddy-Simulation of the geodynamo is required. The study in this direction is deferred for future study.

References

1. Baker, G. E., A class of self-exciting dynamical systems, *SIAM J. Appl. Math.*, **23**, 437-457, 1963.
2. Buzant, E. C. and H. Ginzburg, Some problems of the self-excitation of vegetation, *Phil. Trans. R. Soc. Lond. A*, **271**, 217-236, 1974.
3. Braginsky, S. I., Self-excitation of hydromagnetic fields during the motion of a solid body, *Soviet Phys. Dokl.*, **27**, 126-128, 1974.
4. Braginsky, S. I., Nonlinear self-excitation of the hydromagnetic field, *Phys. Lett.*, **45**, 115-116, 1973.
5. Braginsky, S. I., Nonlinear self-excitation of the hydromagnetic field, *Phys. Lett.*, **45**, 115-116, 1973.
6. Buzant, E. C., Thermal self-excitation of the hydromagnetic field, *Phys. Lett.*, **45**, 115-116, 1973.
7. Buzant, E. C., Thermal self-excitation of the hydromagnetic field, *Phys. Lett.*, **45**, 115-116, 1973.
8. Buzant, E. C., Thermal self-excitation of the hydromagnetic field, *Phys. Lett.*, **45**, 115-116, 1973.
9. Buzant, E. C., Thermal self-excitation of the hydromagnetic field, *Phys. Lett.*, **45**, 115-116, 1973.
10. Buzant, E. C., Thermal self-excitation of the hydromagnetic field, *Phys. Lett.*, **45**, 115-116, 1973.
11. Buzant, E. C., Thermal self-excitation of the hydromagnetic field, *Phys. Lett.*, **45**, 115-116, 1973.
12. Buzant, E. C., Thermal self-excitation of the hydromagnetic field, *Phys. Lett.*, **45**, 115-116, 1973.
13. Buzant, E. C., Thermal self-excitation of the hydromagnetic field, *Phys. Lett.*, **45**, 115-116, 1973.
14. Buzant, E. C., Thermal self-excitation of the hydromagnetic field, *Phys. Lett.*, **45**, 115-116, 1973.
15. Buzant, E. C., Thermal self-excitation of the hydromagnetic field, *Phys. Lett.*, **45**, 115-116, 1973.
16. Buzant, E. C., Thermal self-excitation of the hydromagnetic field, *Phys. Lett.*, **45**, 115-116, 1973.
17. Buzant, E. C., Thermal self-excitation of the hydromagnetic field, *Phys. Lett.*, **45**, 115-116, 1973.
18. Buzant, E. C., Thermal self-excitation of the hydromagnetic field, *Phys. Lett.*, **45**, 115-116, 1973.
19. Buzant, E. C., Thermal self-excitation of the hydromagnetic field, *Phys. Lett.*, **45**, 115-116, 1973.
20. Buzant, E. C., Thermal self-excitation of the hydromagnetic field, *Phys. Lett.*, **45**, 115-116, 1973.

References

- Backus, G. E., A class of self-sustaining dissipative spherical dynamos, *Ann. Phys.*, **4**, 372-447, 1958.
- Bullard, E. C. and H. Gellman, Homogeneous dynamos and terrestrial magnetism, *Phil. Trans. R. Soc. Lond.*, **A247**, 213-278, 1954.
- Braginsky, S. I., Self excitation of magnetic field during the motion of a highly conducting fluid, *Sov. Phys. JETP*, **20**, 726-735, 1964.
- Braginsky, S. I., Nearly axially symmetric model of the hydromagnetic dynamo of the Earth, I., *Geomag. Aeron.*, **15**, 122-128, 1975.
- Braginsky, S. I., Nearly axially symmetric model of the hydromagnetic dynamo of the Earth, *Geomag. Aeron.*, **18**, 225-231, 1978.
- Busse, F. H., Thermal instabilities in rapidly rotating system, *J. Fluid Mech.*, **44**, 441-460, 1970.
- Busse, F. H., A model of the geodynamo, *Geophys. J. R. Astro. Soc.*, **42**, 437-459, 1975.
- Busse, F. H. and C. R. Carrigan, Laboratory simulation of thermal convection in rotating planets and stars, *Science*, **191**, 81-83, 1976.
- Busse, F. H., Magnetohydrodynamics of the Earth's dynamo, *Ann. Rev. Fluid Mech.*, **10**, 435-462, 1978.
- Busse, F. H., Recent developments in the dynamo theory of planetary magnetism, *Ann. Rev. Earth Planet. Sci.*, **11**, 241-268, 1983.
- Chandrasekhar, S., Hydrodynamic and Hydromagnetic Stability, Oxford University Press, 1961.
- Childress, S. and A. M. Soward, Convection-driven hydromagnetic dynamo, *Phys. Rev. Lett.*, **29**, 837-839, 1972.
- Cox, A., Geomagnetic reversals, *Science*, **163**, 237-245, 1969.
- Cowling, T. G., The magnetic field of sunspots, *Mon. Not. R. Astr. Soc.*, **94**, 39-48, 1934.

- Deardorff, J. W., A numerical study of three -dimensional turbulent channel flow at large Reynolds numbers, *J. Fluid Mech.*, **41** , 453-480. 1970.
- Galloway, D. J. and N. O. Weiss, Convection and magnetic fields in stars, *Astrophys. J.*, **243**, 945-953, 1981.
- Gilbert, A. D., Frisch U. and Pouquet A., Helicity is unnecessary for alpha effect dynamos, but it helps, *Geophys. Astrophys. Fluid Dynamics*, **42**, 151-161, 1988.
- Gilman, P. A. and Miller, J., Dynamically consistent nonlinear dynamos driven by convection in a rotating spherical shell, *Astrophys. J. Suppl.*, **46**, 211-238, 1981.
- Gilman, P. A., Dynamically consistent nonlinear dynamos driven by convection in a rotating spherical shell. II. Dynamos with cycles and strong feedbacks, *Astrophys. J. Suppl.*, **53**, 243-268, 1983.
- Glatzmaier, G. A., Numerical simulations of stellar convective dynamos. I. The model and method., *J. Comp. Phys.*, **55**, 461-484, 1984.
- Glatzmaier, G. A., Numerical simulations of stellar convective dynamos. II. Field propagation in the convection zone., *Astrophys. J. Suppl.*, **45**, 351-380, 1985.
- Glatzmaier, G. A., Numerical simulations of stellar convective dynamos. III. At the base of the convection zone., *Geophys. Astrophys. Fluid Dyn.*, **31**, 137-150, 1985.
- Gubbins, D., Theories of the geomagnetic and solar dynamos, *Reviews of Geophysics and Space Physics*, **12**, 137-154, 1974.
- Gubbins, D. and Roberts, P. H., Magnetohydrodynamics of the Earth's Core, in Geomagnetism vol. 2, pp. 1-183, Academic Press, 1987.
- Hamba, F., Numerical Simulation of Reversed Field Pinches Using a Turbulence Model, *J. Phys. Soc. Jpn.*, **58**, 2414-2422, 1989.
- Hasegawa, A., Self-organization processes in continuous media, *Advances in Physics*, **34**, 1-42, 1985.
- Inglis, D. R., Dynamo theory of the earth's varying magnetic field *Reviews of Modern Physics*, **53** (3), 481-496, 1981.
- Krause, F. and Rädler, K.-H., Mean Field Magnetohydrodynamics and Dynamo Theory, Pergamon Press, 1981.

- Lilley, F. E. M., On kinematic dynamos, *Proc. Roy. Soc. Lond. A*, **316**, 153-167, 1970.
- Moffatt, H. K., Magnetic field generation in electrically conducting fluids, Cambridge University Press, 1978.
- Moin, P., and J. Kim, Numerical investigation of turbulent channel flow, *J. Fluid Mech.*, **118**, 341-377, 1982.
- Parker, E. N., Hydromagnetic dynamo models, *Astrophys. J.*, **122**, 293-314, 1955.
- Pouquet, A. N., U. Frisch, and J. Leorat, Strong MHD helical turbulence and the nonlinear dynamo effect *J. Fluid Mech.*, **77**, 321-354, 1976.
- Orszag, S. A., Numerical simulation of incompressible flows within simple boundaries. 1. Galerkin (spectral) representations, *Stud. in Appl. Math.*, **50**, 293-327, 1971.
- Orszag, S. A., Comparison of pseudospectral and spectral approximation, *Stud. in Appl. Math.*, **51**, 253-259, 1972.
- Orszag, S. A., Spectral methods for problems in complex geometries, *J. Comp. Phys.*, **37**, 70-92, 1980.
- Roberts, P. H. and D. Gubbins, Origin of the Main Field: Kinematics in Geomagnetism vol. 2, pp. 185-249 Academic Press, 1987.
- Roberts, P. H., Origin of the Main Field: Dynamics in Geomagnetism vol. 2, pp. 251-306 Academic Press, 1987.
- Steenbeck, M., F. Krause, and K.-H. Rädler, Berechnung der mittleren Lorentz-Feldstärke $\mathbf{v} \times \mathbf{B}$ für ein elektrisch leitendes Medium in turbulenter, durch Coriolis-Kräfte beeinflusster Bewegung, *Zeitschrift für Naturforschung*, **21 a**, 369-376, 1966.
- Stevenson, D. J., Planetary magnetic fields, *Rep. Prog. Phys.*, **46**, 555-620, 1983.
- Taylor, J. B., Relaxation of toroidal plasma and generation of reverse magnetic fields, *Rhys. Rev. Lett.*, **33**, 1139-1141, 1974.
- Veronis, G., Cellular convection with finite amplitude in a rotating fluid, *J. Fluid Mech.*, **5**, 401-435, 1959.
- Walter, M. E., Induction Effects in Terrestrial Magnetism, *Phys. Rev.*, **69**, 106-116, 1946.

- Weiss, N. O., The expulsion of magnetic flux by eddies, *Proc. R. Soc. A*, **293**, 310-328,
- Yokoyama, Y., Study of geomagnetic 60 year variation, Ph. D. thesis, Univ. Tokyo, 1989.
- Yokoyama, Y., Sixty year variation in a time series of the geomagnetic Gauss coefficients between 1910 and 1983 *J. Geomag. Geoelectr.*, **43**, 563-584, 1991
- Yoshizawa, A., Self-consistent turbulent dynamo modeling of reversed field pinches and planetary magnetic fields, *Phys. Fluids B*, **2** (2), 1589-1600, 1990.
- Yoshizawa, A. and F. Hamba, A turbulent dynamo model for the reversed field pinches of plasma, *Phys. Fluids*, **31** (8), 2276-2284, 1988.
- Yukutake, T. and H. Tachinaka, The westward drift of the geomagnetic secular variation, *Bull. Earthq. Res. Inst., Univ. Tokyo*, **46**, 1075-1102, 1968.
- Yukutake, T. and H. Tachinaka, Separation of the earth's magnetic field into the drifting and the standing parts, *Bull. Earthq. Res. Inst., Univ. Tokyo*, **47**, 65-97, 1969.

